DISLOCATION MOBILITY AND PLASTIC DEFORMATION IN MOLYBDENUM SINGLE CRYSTALS

Thesis Submitted for the Degree of

Doctor of Philosophy

by

Gauri Charan Das

Department of Metallurgy,
Imperial College of Science
and Technology,
University of London.

August 1967.

ABSTRACT

Molybdenum single crystals, oriented near the centre of the unit stereographic triangle have been grown by electron beam floating zone-melting technique. A new etchant consisting of H_2SO_4, CH_3OH and $HClO_3$ has been developed to etch dislocations in molybdenum. It can etch planes within 35^o of {100} and is more reliable than the other available etchants.

Tensile and bending specimens have been machined by spark planing and annealed at 2200^oC to reduce the dislocation density from $5 \times 10^5/cm.^2$ to $4 \times 10^4/cm.^2$.

The proportional limit and flow stress are lower for crystals with a low dislocation density, which is attributed to a small long range internal stress. The strain rate and temperature sensitivities have been studied in the temperature range 77^oK to 433^oK and the results are explained in terms of the effect of temperature on the dislocation structure.

The alignment of etch pits in a specimen stressed just above its proportional limit indicates that the dislocations are moving on one {110} plane with a low resolved shear stress. However, at higher strains, the highly stressed $\{110\}\langle 1\bar{1}1\rangle$ type slip systems operate, as determined by slip line analysis.

Dislocation velocity has been determined over four orders of magnitude of velocity at 77^oK, 153^oK, 243^oK and 298^oK. The power dependence of dislocation velocity on stress, m, is 7.2 at 298^oK

and increases to 12.2 at 77°K. Values of m determined by strain rate change and relaxation experiments are much higher than those from the direct etch pit method.

The activation parameters for plastic deformation and dislocation motion have been determined. The results indicate that there may be more than one rate controlling mechanism.

CONTENTS

Page

CHAPTER 1. GENERAL INTRODUCTION AND REVIEW OF LITERATURE 8

1.1. Concept of Dislocations 8

1.2. The Direct Observation of Dislocations 9

1.3. Quantitative Measurement of Dislocation Mobility 9

1.3.1. Experimental Techniques 10

1.3.2. Various Results, Theories and Deductions 11

1.4. Indirect Methods for the Determination of Stress Dependence of Dislocation Velocity 14

1.4.1. Strain Rate Change Experiments 14

1.4.2. Stress Relaxation Method 16

1.5. Yielding and Flow of Body Centred Cubic Metals 17

1.6. Obstacles to Dislocation Motion in B.C.C. Metals 21

1.6.1. The Peierls-Nabarro Force 21

1.6.2. Intersection of Dislocations 22

1.6.3. Jogs in Dislocations 22

1.6.4. Dissociation of Dislocations 23

1.6.5. Impurities 24

1.7. Thermal Activation During Yielding and Flow .. 25

1.8. Calculation of Activation Parameters 27

1.9. Purpose of the Present Investigation 30

CHAPTER 2. THE GROWTH OF MOLYBDENUM SINGLE CRYSTALS .. 32

2.1. Introduction 32

2.2. Zone Refining and Purification 33

Page

2.3. Heating Methods and Electron Beam Floating Zone Melting 34

2.4. Description of the Apparatus 35

2.5. Starting Material 40

2.6. Growth of Single Crystals of Predetermined Orientations and Operating Conditions During Growth 40

2.7. Characteristics of the Single Crystals 45

CHAPTER 3. ETCH PITTING OF DISLOCATIONS IN MOLYBDENUM SINGLE CRYSTALS 46

3.1. Introduction 46

3.2. Reliability of the Etching Methods 48

3.3. Available Etchants for Molybdenum 51

3.4. Development of a New Etchant 55

3.5. Preparation of the Etchant and the Etching Process 57

3.6. The Characteristics of the Etchant 58

3.6.1. Reliability of the Etchant 63

3.7. Discussion 70

CHAPTER 4. PREPARATION AND ANNEALING OF SPECIMENS .. 73

4.1. Introduction 73

4.2. Machining of Specimens by Surface Grinding .. 74

4.3. Polishing of Specimens 75

Page

4.4. Preparation of Specimens by Spark Machining .. 77

4.4.1. Machining of Bending Specimens 79

4.4.2. Machining of Tensile Specimens 82

4.5. Annealing of Specimens 87

CHAPTER 5. YIELDING AND FLOW OF MOLYBDENUM SINGLE CRYSTALS 93

5.1. Introduction 93

5.2. Experimental Techniques 94

5.3. Orientation of Specimens 97

5.4. Deformation Behaviour of Specimens 97

5.5. Crystallography of Slip 104

5.6. Slip Line Observation 105

5.7. Variation of Dislocation Density with Stress and Strain 124

5.8. Strain Rate Sensitivity of Flow Stress 130

5.9. Temperature Sensitivity of Flow Stress 134

5.10. Stress Relaxation Experiments 137

5.11. Calculation of Activation Parameters 140

5.11.1. Activation Volume 141

5.11.2. Activation Energy 144

5.12. Discussion 149

5.12.1. Stress-Strain Curves 149

5.12.2. Crystallography of Slip and Active Slip Systems 154

Page

5.12.3. Deformation and Dislocation Density .. 156

5.12.4. Strain Rate and Temperature Sensitivities of Flow Stress 158

5.12.5. Activation Parameters 160

CHAPTER 6. MOBILITY OF DISLOCATION IN MOLYBDENUM SINGLE CRYSTALS 163

6.1. Introduction 163

6.2. Experimental Techniques 163

6.2.1. Ageing of Specimens 164

6.2.2. Introduction of Fresh Dislocations .. 164

6.2.3. Application of Load 166

6.2.4. Measurement of Dislocation Velocity and Stress Calculation 167

6.3. Results of Some Preliminary Experiments 172

6.4. Orientation and Geometry of the Specimens .. 174

6.5. Dislocation Motion at Various Stresses and Temperatures 174

6.6. Determination of the Slip System for Dislocation Motion by the Etch Pit Method 177

6.6.1. Stress Dependence of Dislocation Velocity 184

6.7. Determination of Activation Volume 189

6.8. Temperature Dependence of Dislocation Velocity 189

Page

6.8.1. Calculation of Activation Energy for Dislocation Motion 194

6.9. Calculation of the Stress Dependence of Dislocation Velocity by Indirect Methods 194

6.9.1. Strain Rate Change Experiments 195

6.9.2. Stress Relaxation Experiments 195

6.10. Discussion 198

6.10.1. Stress Dependence of Dislocation Velocity 198

6.10.2. Slip System for Dislocation Motion .. 201

6.10.3. Comparison of Proportional Limit Flow Stress and the Stress to Move Fresh Dislocations 202

6.10.4. Activation Parameters and Rate Controlling Mechanism for Dislocation Motion .. 202

6.10.5. Determination of m from Indirect Methods 203

CHAPTER 7. CONCLUSIONS AND SUGGESTIONS FOR FUTURE WORK 206

7.1. Conclusions 206

7.2. Suggestions for Future Work 209

REFERENCES 210

ACKNOWLEDGEMENTS 222

CHAPTER 1

GENERAL INTRODUCTION AND REVIEW OF LITERATURE

1.1. Concept of Dislocations

The theoretical shear strength of crystals calculated by Frenkel's model[1] is about 100-1000 times larger than the true yield strength found in practice. Becker's[2] idea of stress concentration due to thermal vibration in the lattice could hardly explain this difference in the order of magnitude. Finally Taylor[3], Polanyi[4] and Orowan[5] introduced the concept of slip dislocations in real crystals. According to them, atoms slip consecutively rather than simultaneously. Slip nucleates in one or few places in the slip plane and then spreads. The boundary between the slipped and the unslipped region is called the dislocation line and plastic deformation occurs by the movement of dislocations.

In an ideal crystal free from dislocations, the actual strength may approach the theoretical strength. Bragg and Lomer[6] have determined the shear strength of a two-dimensional crystal of bubbles to confirm this. It is also supported by the high strength of metal whiskers.

1.2. The Direct Observation of Dislocations

Although the dislocation theory of crystal plasticity was postulated in the mid-thirties, no experimental method for the direct observation of dislocations was available for a long time. Most of the properties of dislocations were determined theoretically or were inferred from the macroscopic mechanical properties of the bulk materials.

The need to verify these postulated and derived properties opened out a new field of experimental research, i.e. the direct observation of dislocations and the study of their individual properties. The different techniques employed for this purpose can be grouped into five main categories, namely surface topology[7-11], etch-pitting[12-24] and decoration[25, 26], X-ray diffraction[27-32], transmission electron microscopy[33-44] and finally, field emission and field-ion microscopy[45-48]. An excellent review of all these methods has been written by Amelinckx[44].

1.3. Quantitative Measurement of Dislocation Mobility

The first quantitative measurement of the mobility of individual dislocations was made by Johnston and Gilman[49] in lithium fluoride single crystals by etch pit method. This was followed

by similar measurements in iron-3% silicon single crystals by Stein and Low[50] and Erickson[51], in germanium, silicon, InSb and GaSb crystals by Patel, Chaudhury and Rubin[52], in germanium single crystals by Dew Hughes[53] and Kabler[54], in NaCl and other alkali halide crystals by Gutmanas, Nadgorni and Stepanov[55, 56], in tungsten single crystals by Schadler[57] and in niobium single crystals by Guberman[58]. Besides, electron microscopy has also been used for dislocation velocity measurements in magnesium[59] and the X-ray Lang method in silicon single crystals[60].

1.3.1. Experimental Techniques

The experimental technique essentially consists of:

a. Preparation of a specimen of proper orientation and geometry.

b. Immobilisation of the grown-in dislocations.

c. Introduction of fresh dislocations into the chemically or electrolytically polished and etched surface.

d. Application of the stress pulse for a predetermined length of time.

e. Measurement of the distance moved by the fresh dislocations after a second etch.

In alkali halides and semiconductors with a low dislocation density the motion of a single dislocation loop is studied

whereas in metals the distance moved by the dislocations from a scratch is measured.

1.3.2. Various Results, Theories and Deductions

The velocity, v, of dislocations is found to be a very sensitive function of stress except in semiconductors. The empirical relation

$$v = \left(\frac{\tau}{\tau_o}\right)^m \qquad (1.1.)$$

where τ is the applied shear stress and τ_o the shear stress for unit dislocation velocity, is obeyed in all cases. It may be mentioned here that a more correct method is to take effective shear stress τ^* ($=\tau-\tau_r$ where τ_r is the long range internal stress) rather than applied shear stress. At very high stresses, investigated only in alkali halides[49, 55], the velocity approaches a limit close to the transverse sound wave velocity in the material. The exponent m for silicon-iron and tungsten decreases with increasing temperature[50, 57].

Gilman[61] has proposed the functional relationship

$$v = v_o \exp(-D/\tau) \qquad (1.2.)$$

where v_o is a limiting velocity close to the elastic shear wave

velocity in the material and D is a characteristic drag stress. Though log v varies linearly with $\frac{1}{\tau}$ in most materials, only in LiF and NaCl do the curves $(v - \frac{1}{\tau})$ extrapolate to the elastic shear wave velocity at infinite stress $(\frac{1}{\tau} \simeq 0)$. However, Gilman[62] has shown that in silicon-iron, when a correction is applied for internal stress fluctuations, the curves do extrapolate to the shear wave velocity.

Equation 1.1. does not seem to have any physical basis and the dislocation velocity does not have any upper limit. On the other hand, Gilman[62] has interpreted equation 1.2. in terms of a two dimensional nucleation theory which successfully accounts for the temperature and stress dependence of dislocation velocity. He has considered both the point-defect-limited mobility controlling the high stress sensitive case and crystal-matrix-limited mobility for the low stress sensitive case. Celli et al.[63] have presented a model of kink nucleation with dragging points on the dislocation and predicted a similar stress dependence of dislocation velocity as equation 1.2. for semiconductors. Kabler's data[54] on dislocation velocity in germanium have been analysed in the light of this model.

In LiF[49] and NaCl[55] the edge dislocation has a higher velocity than the screw. The large difference in the length of edge and screw components in the electron micrographs

of deformed molybdenum[64] and silicon iron[65] also provides evidence for the higher mobility of the edge component. This may be due either to the high jog density or to the dissociation of the screw dislocations.

It has been found from the dislocation velocity measurement in LiF[49] that there is a minimum stress to move dislocations. The movement takes place in jerks, the acceleration distance is very small and the dislocation velocity is dependent on the hardness and strength of crystals. Both radiation damage and impurities have two effects on the dislocation motion, namely static pinning of glide dislocations and dynamic resistance to the motion of fresh dislocations.

In silicon-iron single crystals the mobility of edge dislocations has been measured both on {110} and {112} planes and it is found that in certain favourably oriented crystals {112}$\langle 11\bar{1} \rangle$ slip system is operative above 184°C and {110}$\langle 1\bar{1}1 \rangle$ slip is favourable below this temperature. Dislocation motion on {112} planes needs a somewhat higher stress.

During plastic deformation the formation and growth of glide bands takes place by dislocation multiplication[49, 65, 66] and it is suggested that multiplication occurs by the double cross slip mechanism proposed by Koehler[67] and Orowan[68]. The dislocation density ρ as a function of strain ε is given by the equation[69]:

$$\rho = \rho_o + A\varepsilon^a \qquad (1.3.)$$

where ρ_o is the initial dislocation density and A and a are parameters characteristic of the material.

1.4. Indirect Methods for the Determination of Stress-Dependence of Dislocation Velocity

1.4.1. Strain Rate Change Experiments

Dislocation velocity measurement by the etch-pit method is rather tedious and it is difficult to find a suitable etchant for every material. So Guard[70] suggested that it may be possible to get the power dependence of dislocation velocity on stress from strain rate change experiments.

The plastic strain rate, $\dot{\varepsilon}$, is given by[71]:

$$\dot{\varepsilon} = \phi b \rho \bar{v} \qquad (1.4.)$$

where ρ is the density of mobile dislocations, $\bar{v}$ their average velocity, b is the Burgers vector and ϕ is an orientation factor of mean value ≈0.5 for tensile strain.

On taking the logarithms of both sides of equation 1.4. and differentiating with respect to the logarithm of resolved shear stress τ

$$m' = \frac{d\ln\dot{\epsilon}}{d\ln\tau} = \frac{d\ln\rho}{d\ln\tau} + \frac{d\ln\bar{v}}{d\ln\tau} = \frac{d\ln\rho}{d\ln\tau} + m \qquad (1.5.)$$

If $\frac{d\ln\rho}{d\ln\tau}$ is negligible, i.e. an increase in stress does not increase the number of mobile dislocations appreciably, then

$$m = m' = \frac{d\ln\dot{\epsilon}}{d\ln\tau} \qquad (1.6.)$$

But Guard[70] found that for silicon-iron m' is twice as much as m determined by the etch pit method and he concluded that any rate change is accompanied by an increase in the number of mobile dislocations. Johnston and Stein[72] have suggested that m' increases with strain ϵ and approaches m at $\epsilon = 0$. They have verified this for silicon-iron and lithium fluoride. Later this method has been used by Michalak[73] for high purity iron.

Christian[74] has analysed the strain rate sensitivity method for the determination of m. The same temperature dependence of yield stress, flow stress and stress for constant dislocation velocity implies that change in ρ is negligible during a temperature or strain rate change. He pointed out that in b.c.c. metals the change in tensile stress $\Delta\sigma$ for a given change in strain rate is approximately independent of the stress at which the change is made. This results in a linear increase in m' with the total stress τ. On the other hand for f.c.c. metals which obey Cottrell-Stokes law

($\Delta\sigma/\sigma$ = const.) m' would be constant. The variation of m' with strain may probably reflect a corresponding variation of m with strain. Floreen and Scott[75] determined $d\ln\rho/d\ln\sigma$ for silicon-iron from the experimental data on the variation of cell size as a function of strain and the strain hardening coefficient and found an actual increase in m with strain. However, Li and Michalak[76] have serious doubts as to the validity of this method, and they attribute the difference between m and m' to internal stress.

1.4.2. Stress Relaxation Method

Hull and Noble[77, 78] have tried to derive m from stress relaxation as well as strain rate change experiments. In the former method any transient effects from the machine are eliminated and the slope of the plot log stress against log time gives 1/1-m'. For silicon-iron comparable values of m' are obtained by both the methods. m' remains almost constant at ≈55 during Lüder's band propagation and then sharply increases to 76 at the onset of work hardening followed by a gradual increase with increasing strain. Noble and Hull attribute the larger values of m from indirect methods to the fact that in these experiments there is a large contribution to the strain rate by dislocation movement and deformation in the

existing slip lines and a smaller contribution from dislocations at the tips of slip lines moving into the undeformed region. In the work hardening region the latter contribution vanishes resulting in a sudden increase in m'. Due to this discontinuity in the value of m', they doubt the validity of Johnston and Stein's method of determining m by extrapolation of m' from the work hardening region to zero strain.

Guiu and Pratt[79] have analysed in detail the stress relaxation phenomenon and derived expressions for strain rate sensitivity which have been extensively used during the present investigation. Recently Li[80] has reviewed the indirect methods for determining the stress dependence of dislocation velocity.

1.5. Yielding and Flow of Body Centred Cubic Metals

Body centred cubic transition metals show a strong temperature and strain rate dependence of yield stress at low temperatures and in all these metals except tantalum, there is a ductile to brittle transition associated with the rapid rise in yield stress as the temperature is lowered. They also exhibit discontinuous yielding in both polycrystalline and single crystal forms. Cottrell and Bilby[81, 82] have postulated the theory of dislocation locking to explain the

yield drop phenomenon. Impurity atoms especially interstitials migrate to the dislocation line and form an atmosphere around it. Thus dislocations are effectively locked and during mechanical testing the stress should increase to a sufficiently high value for unlocking or tearing away of the dislocations from the impurity atmosphere to occur. Once dislocations are free they can move at a lower stress. This gives rise to the sudden decrease in stress at the upper yield point.

The dependence of discontinuous yielding on the presence of interstitial impurities[83] and the kinetics of strain ageing[82] lend support to this concept. It can explain the temperature dependence of yield stress because unlocking would be difficult at lower temperatures. However, it fails to explain the same temperature and strain rate dependence[84-86] of upper and lower yield stress, flow stress, delay time during transient creep and Lüder's band velocity during non-uniform yielding.

Gilman and Johnston[87] observed a prominant yield drop in LiF crystals without any evidence of unlocking of grown in dislocations. On the other hand, fresh dislocations were nucleated heterogeneously and subsequently multiplied. They concluded that yielding is determined by the mobility and multiplication of dislocations. The higher yield and flow

stress at low temperatures arises primarily from an increase in the resistance to dislocation motion with decreasing temperature. This was later supported by Stein and Low[50] who found the same temperature dependence of yield stress and the stress to more fresh dislocations at a constant velocity.

Johnston and Gilman[49] and later Johnston[88] have considered the case of a specimen deformed in a hard tensile machine at a constant cross head speed. The stress-strain curves and transient creep curves, derived theoretically using equations 1.1. and 1.4. were in good agreement with the experimental curves for LiF. Johnston[88] also found that low values of the initial density of mobile dislocations (ρ_o) and the power dependence of dislocation velocity on stress (m) produce a significant yield drop and large delay times.

Hahn[69] has applied Johnston's concept of yielding and creep to iron and other b.c.c. transition metals and derived the classical equation of state for yielding and flow

$$\sigma = q\varepsilon p + 2\tau_o \left(\frac{\dot{\varepsilon}}{0.5bf\ (\rho_o + C\dot{\varepsilon p}^a)} \right)^{1/m} \qquad (1.7.)$$

where σ is the flow stress, q is the strain hardening coefficient, εp is the plastic strain and c, a, f, τ_o are constants for the material. The yield drop depends on ρ_o and m in the same manner as in LiF. Both uniform and non-uniform yielding have been explained by Hahn in the light of

this concept.

According to the dynamic theory of discontinuous yielding there are a few mobile dislocations initially present and to keep up the imposed strain rate these dislocations have to move faster (equation 1.4.), so the stress increases rapidly. At the upper yield point there is an increase in the number of mobile dislocations due to multiplication and the imposed strain rate can be maintained with a lower dislocation velocity at a lower stress. This accounts for the load drop from the upper to the lower yield point.

Later Cottrell[89] has brought both these theories together. He suggests that discontinuous yielding is possible only when there are few mobile dislocations initially present and yield drop occurs by a sudden increase in the number of mobile dislocations either by unpinning when the dislocations are weakly locked, or by the creation and multiplication of mobile dislocations at points of stress concentration when the crystal is nearly perfect or the grown-in dislocations are strongly locked. The friction stress is mostly responsible for the temperature dependence of yield stress, though under certain circumstances it may come from the unpinning stress.

1.6. Obstacles to Dislocation Motion in B.C.C. Metals

Plastic deformation occurs by the movement of dislocations and any obstacles to this movement may have some influence on the yielding and flow behaviour of b.c.c. metals. These obstacles may have a short range stress field, e.g. Peierls-Nabarro force, intersection of dislocations, cross slip, dissociation of dislocations into partials and impurities in the materials or they may have a long range stress field, e.g. dislocations on parallel slip planes and large precipitates.

Thermal fluctuation can assist in overcoming the short range or thermal obstacles, but long range athermal obstacles are impervious to thermal fluctuation.

1.6.1. The Peierls-Nabarro Force

The Peierls-Nabarro force (henceforth designated as P.N.F.) represents the inherent resistance of the crystal lattice to the motion of a dislocation when it moves from one potential valley to the next[90, 91]. A dislocation may overcome the P.N. energy barrier by a thermally activated mechanism involving the formation of a pair of kinks under the action of thermal fluctuation and applied stress. This model was originally proposed by Seeger[92] to explain the internal

friction peaks in f.c.c. metals and has since then been studied in detail by Seeger et al.[93], Lothe and Hirth[94] and Dorn and Rajnak[95]. Expressions for the kink energy, activation energy for kink nucleation and the kinetics of dislocation motion have been derived for this model.

1.6.2. Intersection of Dislocations

A dislocation while moving on its glide plane, intersects forest dislocations which cross this glide plane. This may result either in the formation of a jog[71] or in a junction reaction[96-98]. In the latter case the reaction

$$\frac{a}{2}[111] + \frac{a}{2}[1\bar{1}\bar{1}] \rightarrow a[100]$$

leads to an attractive junction and corresponds to a gain in energy in the configuration. This reaction is supposed to be responsible for the hexagonal network observed in several b.c.c. metals[99-101]. The forest dislocations may also exert long range elastic repelling stresses on the moving dislocations.

1.6.3. Jogs in Dislocations

The low mobility of the screw dislocation compared to

that of the edge[49, 55, 64, 65] has been attributed to the presence of jogs. They may be either thermal jogs retained during cooling from a high temperature or intrinsic jogs existing in the dislocation network for geometrical reasons[102]. They may also be produced by dislocation intersection and cross slip during plastic deformation[71].

A jog in a screw dislocation can move either conservatively along the dislocation line[103] or non-conservatively producing trails of edge dislocations or point defects[104]. In the latter case additional energy is necessary for the production of lattice defects and so jogs exert a dragging force on the dislocations.

1.6.4. Dissociation of Dislocations

The low mobility of the screw dislocation may also be due to its dissociation which has been investigated in some detail by Hirsch and co-workers[105-107]. The usual dissociation of $\frac{a}{2}$ <111> screw dislocation in the b.c.c. lattice is along the three symmetrical {110} or {112} planes or on composite planes, as

$$\frac{a}{2}\langle 111\rangle \rightarrow \frac{a}{6}\langle 111\rangle + \frac{a}{6}\langle 111\rangle + \frac{a}{6}\langle 111\rangle$$

Sleeswyk[108] has shown that the lowest energy configuration corresponds to asymmetric dissociation on {112} planes. The

dissociated dislocation can move by forming a constriction in the fault which contributes to the friction stress. The long slip distances for edge dislocations compared to the screws[109] and the preferential alignment of screw dislocations along <111> directions at low temperatures[106] can be explained by this mechanism.

1.6.5. Impurities

Impurities can exist either in solid solution or as precipitates. The short range dislocation impurity atom interaction due to volume changes in the lattice induced by the impurities produces a viscous drag which can be overcome by thermal fluctuations. Those interstitials which introduce a tetragonal distortion in the lattice cause rapid hardening[110] and probably affect the mobility of both edge and screw dislocations.

At higher temperatures stress-induced local ordering of interstitial impurity atoms about a dislocation has been proposed by Schoeck[111] to explain the well known Snoek peak in internal friction. Schoeck and Seeger[112] have analysed the dragging force arising from this effect and their analysis has been verified by Arsenault[113]. Interstitial impurities can also migrate to dislocations and the elastic interaction between the two results in the well known Cottrell locking[81].

Precipitates can give rise to a temperature dependent friction stress only if they are small in size and distributed uniformly[114]. Large precipitates possess a long range stress field which cannot be overcome by thermal activation.

1.7. Thermal Activation During Yielding and Flow

The strong temperature and strain rate dependence of the yield and flow stress of b.c.c. metals has been attributed to a number of different thermally activated mechanisms.

Unlocking of dislocations from the interstitial atmosphere, suggested by Cottrell and Bilby[81, 82] has been supported by Fisher[115]. Heslop and Petch[116] attributed the impurity insensitivity of the temperature dependent portion of the friction stress to the presence of a strong P.N.F. in α-iron. Conrad and co-workers[117-119] have found that in b.c.c. metals activation energy and activation volume as a function of stress are independent of the structure and impurity content, a fact which supports the overcoming of the P.N. barrier as the rate controlling mechanism. Conrad's experimental data[119] is also in good agreement with Seeger's model for the thermally activated nucleation of kinks. Experimental results of Basinski and Christian[120] with α-iron

and Christian and Masters[121] with transition b.c.c. metals also favour the same mechanism.

In molybdenum[122], tungsten[123] and iron[124] single crystals the temperature dependence of the yield stress decreases with increasing purity which has prompted Stein[125] to suggest that dislocation impurity interaction may be the rate controlling mechanism. However, contrary to this the yield stress is found to be independent of impurity content at very low temperatures[122].

Schoeck[102] has suggested the non-conservative motion of jogs in screw dislocations as a possible rate controlling mechanism in b.c.c. metals. This has received support from the results of Mordike[126] in tantalum, Rose, Ferris and Wulff[127] in tungsten and Gregory[128] and Gregory et al.[129] in niobium.

Mordike and Haasen[114] have found that in iron single crystals the temperature and strain rate sensitivities of flow stress are structure sensitive and vary with heat treatment. The activation parameters are in close agreement with a rate controlling mechanism involving the overcoming of small precipitates of carbides and nitrides.

Brown and Ekvall[130] found that for very pure iron the microscopic yield stress σ_A has a much lower temperature dependence than the macroscopic flow stress σ_f. They

suggest that this may be due to an increased rate of work hardening in the microstrain region as the temperature is decreased and so the rate controlling mechanism may be the cross slip of screw dislocations. According to Kussowsky and Brown[131], two different P.N.F. mechanisms may be rate controlling in micro and macro yielding and possibly σ_f is controlled by the P.N.F. for cross slip.

Conrad[132] has studied the activation parameters for yielding and flow in different metals and predicted the probable dislocation mechanisms operating in different temperature ranges in b.c.c., f.c.c. and h.c.p. metals and alloys. However, it is impossible to confirm that a particular rate controlling mechanism is operating. Some experimental results for b.c.c. metals can only be explained by assuming two instead of one rate controlling mechanisms are operating at the same time[133].

1.8. Calculation of Activation Parameters

If dislocation motion is controlled by a single thermally activated process one can write:

$$v = \alpha \nu_o \exp\left(\frac{-G}{KT}\right)$$

$$= \alpha \nu_o \exp\left(\frac{s}{k}\right) \exp \frac{-H(T,\tau^*)}{KT}$$

$$= \alpha\nu^* \exp \frac{-H(T,\tau^*)}{KT} \qquad (1.8.)$$

where v is the dislocation velocity, α is the product of the number of places where thermal activation can occur per unit length of dislocation line and the area swept out during a successful thermal fluctuation, ν_o is the frequency of vibration of the dislocation segment, $G = H(T,\tau^*) - TS$ is the free energy of activation, $H(\tau^*, T)$ is the enthalpy of activation usually called the activation energy and is a function of the effective stress τ^* and absolute temperature T, s is the entropy of activation and $\nu^* = \nu_o \exp \frac{s}{k}$, k being Boltzmann's constant.

The effective shear stress τ^* is given by

$$\tau^* = \tau - \tau_\mu \qquad (1.9.)$$

where τ is the applied shear stress and τ_μ, the long range internal stress is proportional to the shear modulus μ and depends on temperature only through the variation of μ with temperature.

The shear strain rate $\dot{\gamma}$ at which the specimen deforms is given by (equation 1.4.)

$$\dot{\gamma} = \rho bv = \rho ba\nu^* \exp \frac{-H(T\tau^*)}{KT}$$

$$= \nu \exp \frac{-H(T\tau^*)}{KT} \qquad (1.10.)$$

where $\nu = \rho b \alpha \nu^*$.

Activation energy $H(T,\tau^*)$ and activation volume v^* can be determined from the relations[134, 117].

$$H(T,\tau^*) = -K \left(\frac{\delta \ln \dot{\gamma}/\nu}{\delta \frac{1}{T}} \right)_{\tau^*}$$

$$= -KT^2 \frac{(\delta\tau/\delta T)_{\dot{\gamma}}}{(\delta\tau/\delta \ln \dot{\gamma}/\nu)_T} \qquad (1.11.)$$

and $$v^* = -\frac{dH}{d\tau^*} = KT \left(\frac{\delta \ln \dot{\gamma}/\nu}{\delta \tau} \right)_T \qquad (1.12.)$$

It has been assumed here that the variation of τ_μ with a change in temperature or strain rate is negligible compared to the variation of τ^*. Assuming ν = const. one can determine $\left(\frac{\delta \ln \dot{\gamma}/\nu}{\delta\, 1/T} \right)_{\tau^*}$ by changing the temperature during a creep test, $\left(\frac{\delta\tau}{\delta T} \right)_{\dot{\gamma}}$ by changing the temperature during a conventional tensile or compression test and $\left(\frac{\delta\tau}{\delta \ln \dot{\gamma}/\nu} \right)_T$ from a stress change during creep test or strain rate change during a tensile or compression test.

ν can be obtained from the slope of the plot H vs. T using the relationship

$$H = KT \ln (\nu/\dot{\gamma}) \qquad (1.13.)$$

1.9. Purpose of the Present Investigation

It has been established beyond doubt that the motion and multiplication of dislocations play a very important role in the plastic deformation of materials. However, unfortunately very little work has been done on the quantitative measurement of dislocation velocity in different materials and such work has so far been limited to single crystals of alkali halides, silicon-iron, semiconductors, tungsten and niobium, due to the inherent difficulty in obtaining specimens of low dislocation density especially in metals and developing a reliable etchant to etch dislocations on the proper crystallographic surface. The results from the indirect methods based on too many doubtful assumptions are often unreliable.

It was, therefore, decided to make direct quantitative measurement of dislocation velocity in molybdenum. The present investigation can be divided into the following parts.

1. Growth of molybdenum single crystals and preparation of specimens with a low dislocation density.
2. Development of a reliable etchant to etch dislocations in molybdenum.
3. Measurement of dislocation velocity by etch pit method at different stresses and temperatures.
4. Determination of the stress dependence of dislocation velocity by indirect methods and to compare it with that

from the direct method.

5. Studying the effect of a very low dislocation density (produced by annealing specimens at a temperature close to the melting point) on the deformation behaviour of molybdenum single crystals and the determination of the slip systems by etch pit method.

6. Calculation of activation parameters for plastic deformation to determine the probable rate controlling dislocation mechanism for yielding and flow in these crystals.

CHAPTER 2

THE GROWTH OF MOLYBDENUM SINGLE CRYSTALS

2.1. Introduction

The limitations of shape, size and purity in refractory metal single crystals grown by conventional strain anneal[134] and high temperature gradient methods have been finally overcome with the development of floating zone melting technique. In this method, a molten zone is established between two vertically held cylindrical rods and moved from one end to the other. A steep temperature gradient and slow rate of zone travel prevents the formation of any extraneous nuclei and the molten metal solidifies in the form of a single crystal. This method, initially applied by Keek and Golay[135] to grow single crystals of silicon, has since been used widely to grow single crystals of refractory metals like molybdenum[136-138], tungsten[136, 138-140], tantalum and niobium[136, 141]. The mechanical stability of the molten zone is a function of the radius of the rod, the surface tension and density of the liquid and the shape of the solid-liquid interface[142-144].

2.2. Zone Refining and Purification

Crystals with a high purity can be grown by floating-zone-melting technique because growth takes place in clean conditions out of contact with a crucible and is accompanied by zone refining. The principles of zone refining have been reviewed by Pfann and others[145-147]. Soluble impurities which lower the melting point of the solvent accumulate in the molten zone and concentrate at the finishing end, whereas those raising the melting point concentrate at the starting end.

The extent of zone refining in crystals grown by floating zone melting has been studied using low temperature resistivity measurements. In low melting point metals there is a distinct preferential distribution of impurities[148], but in refractory metals this effect is negligible[149] and confined only to a small region near the starting end[138].

Most of the purification during the growth of refractory metal single crystals occurs by preferential volatilization and vacuum distillation of impurities[135, 138, 139, 148]. The degree of purification attained is dependent on the extent to which the products of volatilization and distillation can be removed by the vacuum system without the introduction of new contaminants into the furnace chamber. Carbon is mainly removed as CO after combining with oxygen in the metal[150, 151] and its removal is enhanced when the oxygen content of the

metal is high[151]. The refractory metals give up oxygen as a metal suboxide and many metallic and gaseous impurities get preferentially volatilized [150, 152].

2.3. Heating Methods and Electron Beam Floating Zone Melting

A floating zone can be produced by radiation[153], induction heating[136] or by an electron bombardment technique developed by Davis, Calverley and Lever[140]. However, electron beam floating-zone-melting, with its greater versatility and advantages, has now virtually supplanted the other methods for the growth of refractory metal single crystals. In this method, electrons thermionically emitted from the hot filament of a cathode assembly are accelerated by a d.c. potential of a few kilovolts towards the polycrystalline rod (anode) where they give up their excess kinetic energy as heat. The electrons are focussed over a narrow zone and the heat produced is sufficient to melt the material. Easy construction of the apparatus, better control of melting, low power requirements and applicability to small diameter specimens are some of the advantages of electron beam floating-zone-melting. The only severe limitation is the vapour pressure of the metal at its melting point. Considerable details about the principles of the electron bombardment floating-zone-melting and the construction

of the apparatus have been given by Calverly, Davis and Lever[154], Birbeck and Calverly[155], Drangel and Murray[138] and Schadler[144].

2.4. Description of the Apparatus

A general view of the electron beam zone-melting apparatus used for growing single crystals during the present investigation is shown in Figure 2.1. Essentially it consists of a water cooled, nickel plated, mild steel furnace chamber evacuated from below by an oil diffusion pump with a capacity of 300 litres/sec. A liquid nitrogen trap between the furnace chamber and the diffusion pump prevents any back streaming of diffusion pump oil vapour into the furnace chamber.

All the internal parts (Figure 2.2.) are connected to the lid and can be lifted out of the furnace chamber. A liquid nitrogen trap is provided at the top to improve the ultimate vacuum. Power leads are introduced into the furnace through glass vacuum seals. The cathode assembly is mounted on a water cooled lead screw and is insulated by two blocks of pyrophilite. The lead screw enters the furnace through Wilson seals and is driven by a variable speed motor with a reduction gear giving speeds from 0 to 30 cm./minute. During crystal growth the molten zone is observed through a quartz

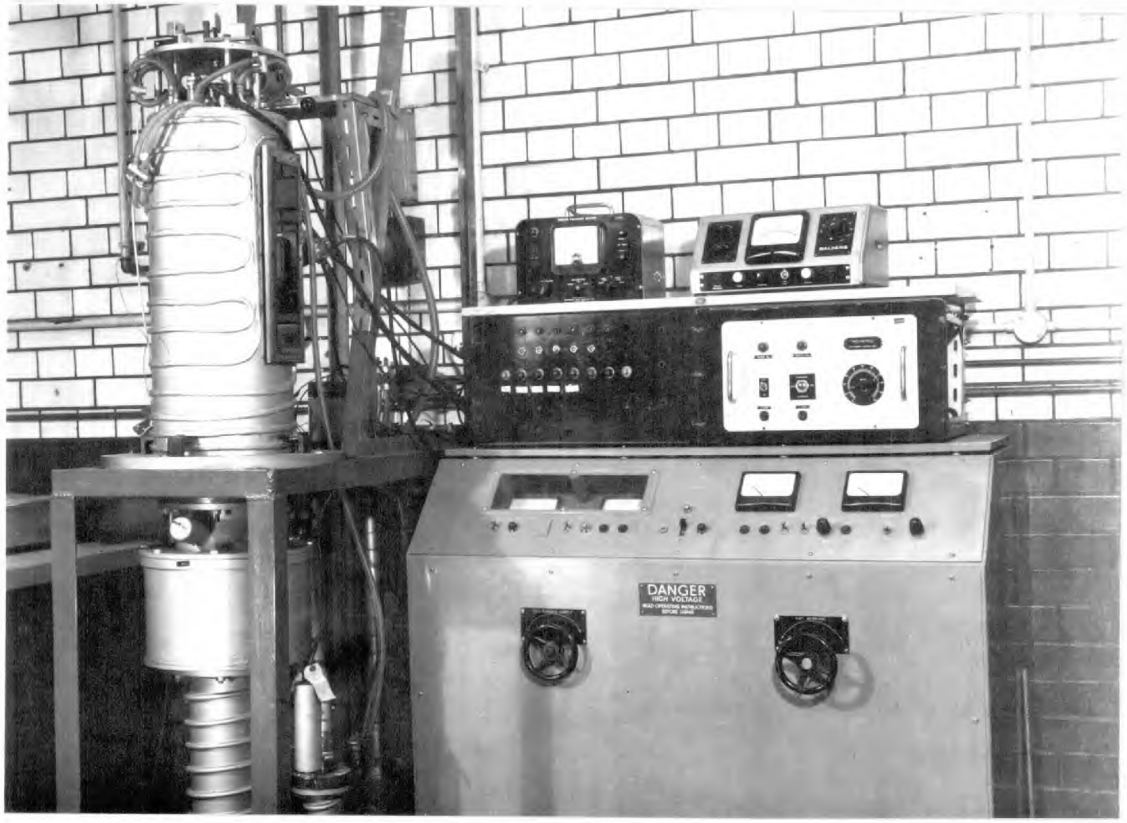


Figure 2.1. General view of the electron beam zone melting equipment.

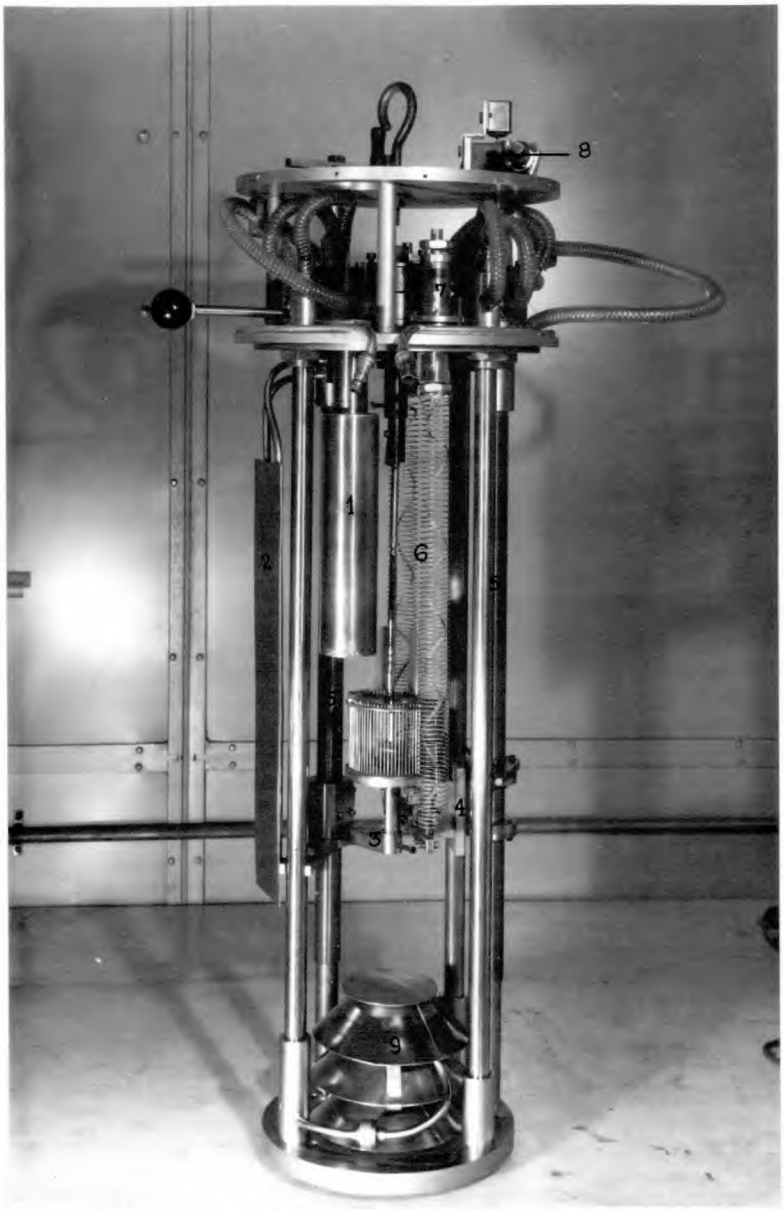


Figure 2.2. Internal parts of the electron beam zone melting furnace.

1. Liquid nitrogen trap 2. Movable window shield.
3. Lower rod clamp, adjustable in height.
4. Insulating 'pyrophilite' blocks. 5. Water cooled lead screws. 6. Extendible current leads.
7. Vacuum sealed terminals. 8. Reduction gear.
9. Water cooled baffle.

window on the furnace wall. It is protected from the metal vapour deposit by a silica glass plate and a movable water cooled radiation shield. Pressure is measured by a Balzers ionization guage with its head connected to the side of the furnace.

The cathode (Figure 2.3.) is squirrel cage-type, similar to one used by Cole et al.[156] and its components are made of molybdenum. The filament is a 0.5 mm. diameter tungsten wire loop heated by a 50 Kv 20 amp transformer. The cage, maintained at the same negative potential as the cathode focusses the electron beam about 2.5 cm. above the filament level. This prevents the contamination of the molten zone with metallic vapours from the filament and the coating of the filament by the evaporation and sputtering of metal from the molten zone.

The power unit for the high voltage d.c. supply consists of a one amp full wave rectifier with a trip circuit to prevent over-loading. The emitter is operated in the emission limited range rather than the space charge limited range. Power control unit operated by thyratrons regulates the temperature of the filament and thus the emission current.

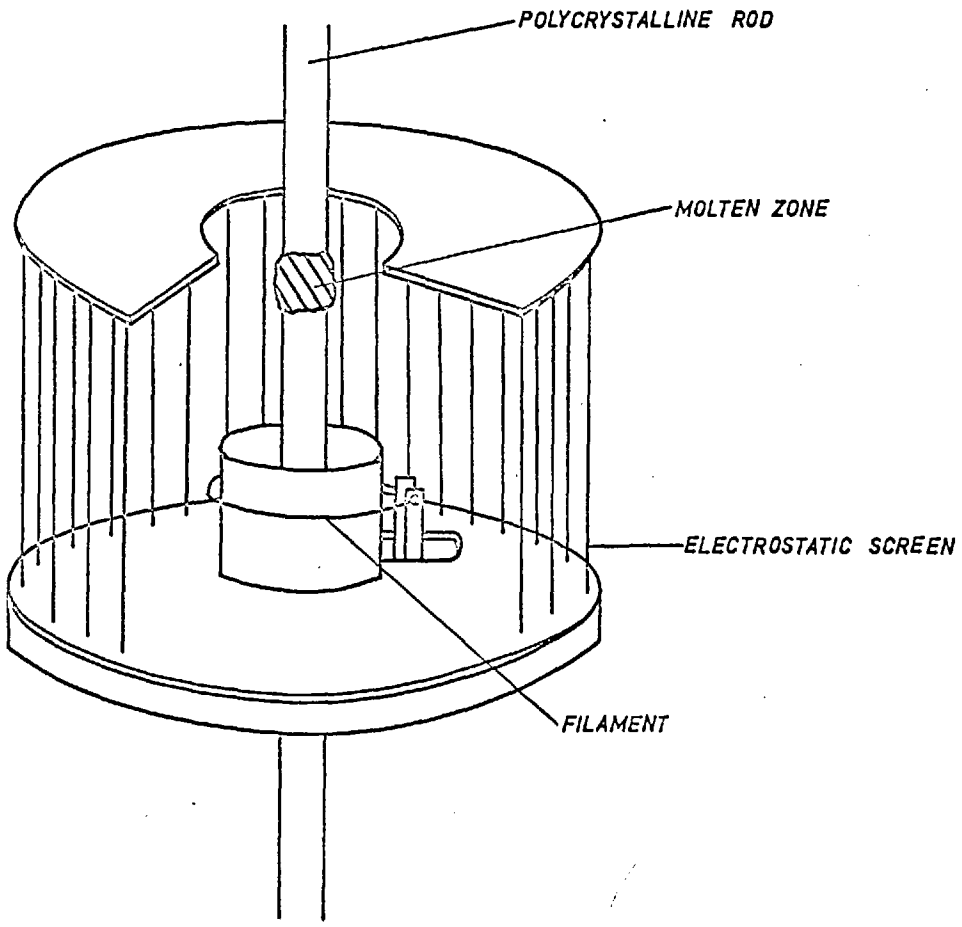


Figure 2.3. Schematic diagram of the cathode.

2.5. Starting Material

The starting material was a polycrystalline, sintered and ground molybdenum rod of 6.35 mm. diameter, supplied by Murex Ltd., Rainham. With the first batch of material there was excessive sputtering and a loss of about 20% of the material during the first pass. The melting conditions were most unstable and the resulting single crystal had a very irregular shape due to the frequent switching off of the power supply during melting. This material was rejected and samples from different batches of sintered molybdenum were tried before selecting a new batch of rods for growing the single crystals. Also a few crystals were grown from the arc cast and hot swaged molybdenum rods, supplied by The Armament Research and Development Establishment, Woolwich, to find out any possible difference in the dislocation structure in the crystals grown from two different materials. The chemical analyses of the two types of molybdenum rods as supplied by the manufacturers are given in Table 2.1.

2.6. Growth of Single Crystals of Predetermined Orientations and Operating Conditions During Growth

Single crystals grown from polycrystalline rods had a random orientation. However, due to the preferred <110>

Table 2.1.

Analyses of polycrystalline molybdenum, molybdenum single crystals and annealed specimens.

Material	Content in p.p.m. in weight					
	H	N	O	C	Fe	Si
Arc cast molybdenum. Analysis supplied by A.R.D.E. Woolwich	4	12	6	80	100	20
Sintered molybdenum. Analysis supplied by Murex Limited	5	50	50	50	20	15
Two pass single crystals grown from sintered molybdenum. Analysis supplied by B.N.F.M.R.A.		<10	8			
Annealed single crystal specimens. Analysis supplied by B.N.F.M.R.A.		<10	7			

texture in these rods the orientation of some of the crystals was close to <110>. The desired orientation was obtained by using a proper seed crystal. The seed was prepared by holding a randomly oriented single crystal in a two circle goniometer (Figure 2.4.), taking a Laue photograph, giving the crystal the necessary rotations and then cutting it with a carborundum slitting wheel through a plane normal to the desired orientation. The cut face was held by a screw flat against the horizontal strip of the seed holder. The polycrystalline rod and the seed were aligned properly and welded. Melting was started in the seed and the molten zone was allowed to travel from the seed crystal on to the polycrystalline rod at a speed of 2.5 mm. per minute. The second pass was started in the opposite direction from within the single crystal part at the other end. As purification occurs mostly by vacuum distillation and evaporation of impurities, zone-refining was not used and two passes in the opposite directions produced a single crystal of reasonable purity and uniform composition. Once a crystal of the desired orientation had been grown it was used as a vertical seed to grow more crystals of the same orientation.

The pressure in the furnace chamber with the water cooling on was about 5×10^{-6} torr and decreased to $\approx 1.5 \times 10^{-6}$ torr when the trap at the top of the chamber was filled with

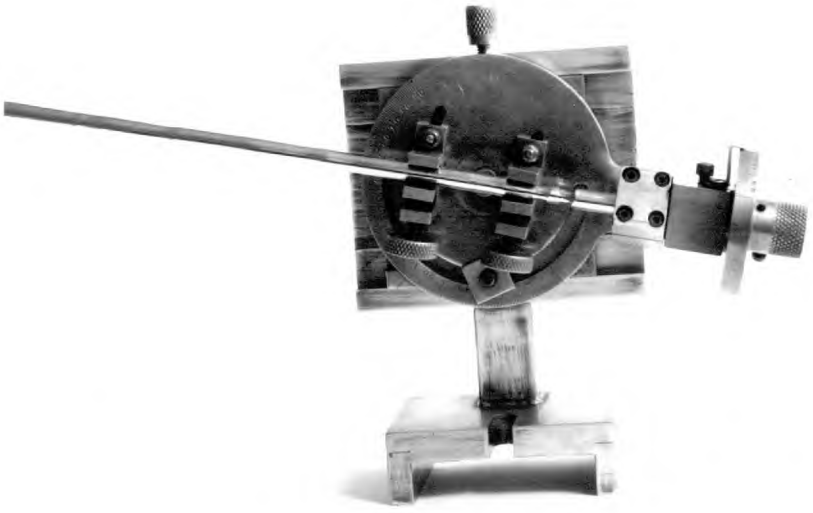


Figure 2.4. Two stage goniometer.



Figure 2.5. Two pass molybdenum single crystal with a centimeter scale.

liquid nitrogen. The pressure increased with the heating and was about 6×10^{-6} torr immediately before melting. However, it improved continuously with melting because molybdenum vapour gets deposited on the liquid nitrogen cold finger and other cold parts of the furnace and acts as a getter of gases, especially hydrogen. At the end of the first pass the pressure was $\simeq 5 \times 10^{-7}$ torr and during the second pass it decreased to an ultimate value of $\simeq 2 \times 10^{-7}$ torr.

The polycrystalline rod was initially given a degassing pass at a temperature close to the melting point using a power output of about 550 watts. This reduced the sputtering during subsequent melting to a great extent. A voltage of $\simeq$ 6.5 Kv and emission current of $\simeq$ 110 amps were used during melting. The power was maintained at $\simeq$715 watts during the first pass and reduced to $\simeq$700 watts for the second pass so that the conditions in the molten zone were optimum. Loss of material due to evaporation and sputtering was $\simeq$10% for the first pass and $\simeq$7% for the second pass. When arc cast molybdenum rods were used for growing single crystals, sputtering was completely absent and the degassing pass was unnecessary.

2.7. Characteristics of the Single Crystals

A two pass single crystal grown by this method is shown in Figure 2.5. The orientations of most crystals were within $\pm$ 3° of the seed crystal. The Laue photographs show sharp and clear spots which indicates that misorientation between subgrains is less than 0.5°. Guiu[157] has studied the impurity content and its distribution in molybdenum single crystals grown in the same apparatus under very similar experimental conditions by measuring the microhardness and proportional limit along the length of the crystals. His results indicate that the distribution of impurities is fairly uniform.

The as grown single crystals have been analysed by B.N.F.M.R.A. and the results are listed in Table 2.1.

CHAPTER 3

ETCH PITTING OF DISLOCATIONS IN MOLYBDENUM SINGLE CRYSTALS

3.1. Introduction

A method involving the preferential dissolution of material at the emergence of dislocations was developed independently by Gevers et al.[12] and Horn[13] for silicon carbide so as to reveal both the screw and edge dislocations. Since then several methods of etching, namely thermal etching[14], chemical etching[15], solution etching[16], preferential oxidation[17], electrolytic etching[18] and cathodic sputtering[19] have been successfully applied in different materials to develop dislocation etch pits. Preferential dissolution of material may be due to the strain energy around a dislocation. This is most probable in cases where the etchants etch only fresh dislocations. On the other hand, prior ageing treatment necessary to reveal dislocations in certain metals and alloys like tantalum[20], niobium[21] and silicon iron[18] suggests that an impurity atmosphere around the dislocations is essential for etching, thus relieving the strain near the dislocation, but increasing the solubility locally.

Etching is very sensitive to the crystallographic orientation of the surface. In silicon-iron all crystallographic

planes can be etched; in copper one can etch within 3^{o} of {111} whereas in tungsten planes within 38^{o} of {100}are etchable[23]. A systematic study of the orientation effect for different etchants has been made by Holmes[24]. The shape of the etch pits also depends on the etching plane. Usually preferential dissolution takes place along {110} and {100} planes and they form the faces of the etch pit. So pits have a square pyramidal shape on {100} planes and get elongated away from {100}. On {111} planes pits are triangular in shape. Impurities in the etchant can often change the ratio of the lateral dissolution rate to the normal dissolution rate which results in a change in the shape and size of the pits.

Of all the methods available for the direct observation of dislocations the etch pit technique is probably the simplest since it involves polishing the surface of the specimen, and then immersing it in the proper etchant. Sometimes electrolytic etching is necessary as in case of silicon-iron and niobium. One limitation of the etch pit method is that it reveals only the points of emergence of dislocations, but it is possible to study a number of phenomena by this method, namely: polygonisation during the annealing of bent single crystals; climb; deformation patterns such as the distribution of dislocations in slip and glide bands; pile ups against grain boundaries; and growth of glide bands by dislocation multiplication.

In the case of copper, Livingstone[158] has observed dark and light pits on {111} planes moving in opposite directions under an applied stress. He attributes this difference in the pit characteristic to positive and negative dislocations. However, no such observation has so far been made in other materials.

3.2. Reliability of the Etching Methods

Before using the etch pit method for any quantitative studies of dislocations, it is necessary to establish the reliability of the etchant since pits can form at fission tracks[159], impurity precipitates or inclusions[160, 161], linear defects other than dislocations[162] and even at surface steps. The correspondence between etch pits and dislocations has been reviewed by Johnston[163], Amelinckx[44] and several other authors. In general it is necessary to find out whether (a) there is some correlation between etch pits and dislocations (b) all dislocations form etch pits and (c) all etch pits correspond to dislocations. Of these the third one is the most difficult to confirm.

Whether etch pits correspond to continuous line defects can be verified by repeated polishing and etching when the identity of the pit distribution will be maintained. Only when

a new dislocation loop is encountered or an old loop polished away pits will appear or disappear in pairs[87, 164]. Continued etching should result only in an increase in the pit size without any change in the pit density. However, a more convincing method is to compare etch pits on two matching surfaces of a cleaved crystal when the etch pit patterns should be mirror images of each other. This has been verified in single crystals of lithium fluoride[87] and tungsten[165].

Dash[166] has decorated and etched silicon single crystals and observed correspondence between dislocation lines and etch pits. Similar correspondence has been observed in electron micrographs of etched thin foil specimens of silicon-iron[167]. Etching should reveal the substructure in an as grown crystal and the etch pit density should increase with applied stress as a result of dislocation multiplication.

One to one correspondence between the dislocations and etch pits can be checked by introducing a predetermined number of dislocations into a single crystal specimen. The equilibrium density 'N' of the excess dislocations of a given sign introduced by uniform plane bending has been calculated by Nye[168] and is given by

$$N = \frac{1}{Rb \cos \phi} \qquad (3.1.)$$

where R is the radius of curvature, b the Burgers vector and ϕ the angle between b and the neutral plane. This formula has been experimentally verified in single crystals of germanium[169], copper[22], silicon-iron[18] and tungsten[165].

Vogel et al.[170] have measured the misorientation θ across a tilt subboundary and showed that the spacing D of etch pits along the subboundary obeys the relation Db/θ. The measurement of a small angle θ is rather difficult and using the Read and Shoekley[171] formula, Amelinckx[172] has established a relation:

$$\Sigma \rho_i / (\cos \phi_i + \sin \phi_i) = 0$$

where ρ_i is the dislocation density along the i-th of the three tilt boundaries, and ϕ_i the angle between the i-th boundary and a symmetrical tilt boundary. This relationship is found to be satisfied in sodium chloride[172], germanium[173] and silicon-iron[174]. Schadler[165] has measured the difference in step height between two slip lines in tungsten and found reasonable agreement between the calculated number of dislocations to form the slip step and the number of etch pits between the slip lines.

3.3. Available Etchants for Molybdenum

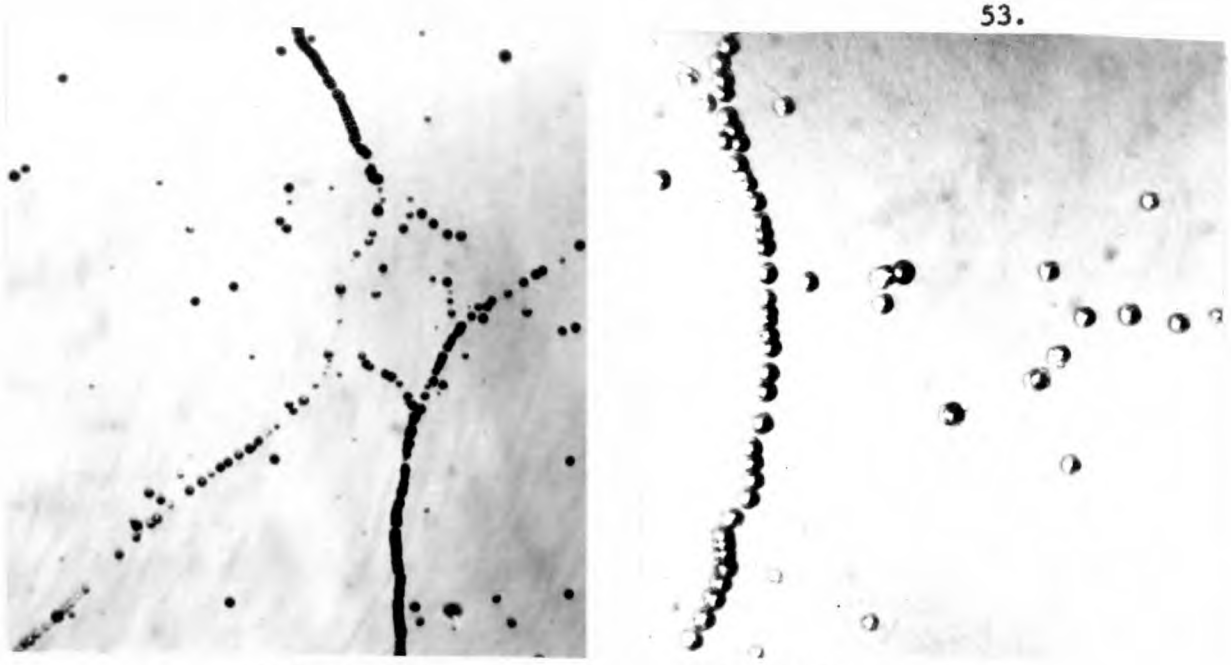
Several etchants have been used to develop etch pits at the sites of dislocations in molybdenum. Due to the similar chemical properties of tungsten and molybdenum, many etchants which etch tungsten can also etch molybdenum. The following etchants for molybdenum have been used.

1. Chemical etching in:
   a. Murakami's solution, which contains $K_3Fe(CN)_6$ and NaOH in water[175, 176, 157].
   b. The Millner and Sass Reagent (a solution composed of 2 parts by volume of a 25 wt.% solution of $CuSO_4$ and 1 part by volume of reagent grade NH_4OH at 45°C).
   c. 50% HNO_3 in water.
2. Electrolytic etching in:
   a. A dilute solution of oxalic acid[177, 178].
   b. A 2.5 wt.% solution of NaOH at 2 volts and 0.05 amp/cm.^{2} current density.

For the etchants mentioned above the composition and the etching conditions are not very critical. All of them have very similar etching characteristics and they reveal both grown in and fresh dislocations without any prior decoration. They can etch {100} planes and any other plane that makes an angle of not more than 30° with the {100} planes. The shape of the pits depends on the etching plane. On {100} planes the

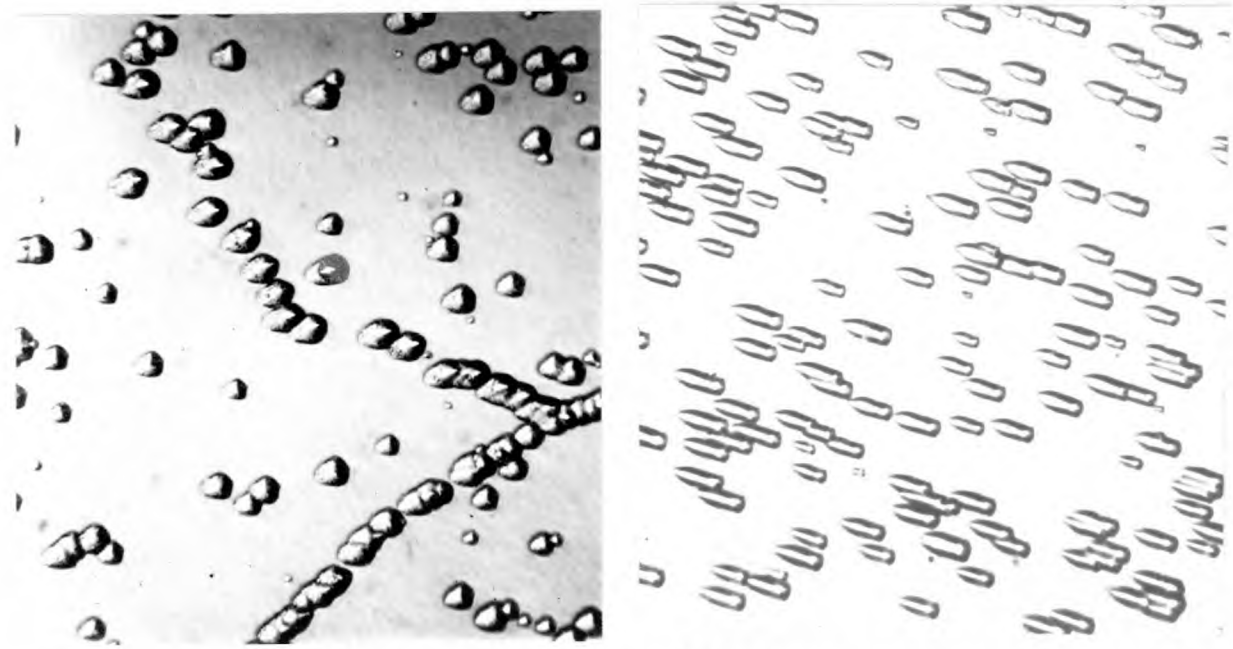
shape is conical, but at higher magnification it appears as a truncated pyramidal pit (Figure 3.1.). On planes at increasing angle from {100} the etch pits become more and more elongated and inclined to the surface (Figure 3.2.). It appears that the faces of the pits correspond to {110} planes. This is very similar to the pit characteristics observed by Berlec and Schadler in tungsten single crystals.

All these etchants show a peculiar behaviour. The density of the etch pits is a minimum on {100} planes and increases with increasing angle from {100}. At about 30^{o} from {100} the pit density is very high and beyond that the planes get oxidised rather than etched (Figure 3.3.). This can hardly be explained in terms of a preferential distribution of dislocations as the same behaviour is observed on all {100} planes and the planes around it. It is possible that on {100} all dislocations are not etched whereas away from {100} some other defects such as surface steps may be getting etched in addition to the dislocations. So the establishment of one to one correspondence between etch pits and dislocations for these etchants is not possible. However, it is evident that these etchants do produce etch pits at dislocations because the density of etch pits increases with plastic deformation, etch pits form near microindentations (Figure 3.4.) and scratch (Figure 3.5.) and can be moved under an applied stress.



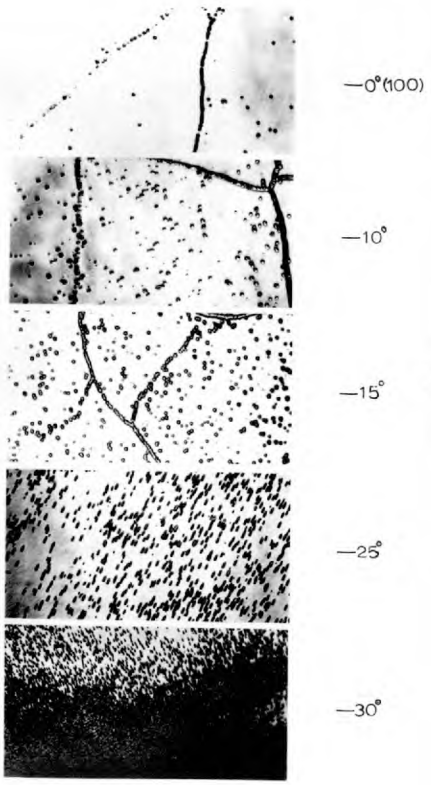
(a) x 200 (b) x 500

Figure 3.1. Etch pits on {100} etched with a solution of 10 wt.% $K_3Fe(CN)_6$ + 10 wt.% NaOH in water. Etchant A.



(a) x 500 (b) x 500

Figure 3.2. Etch pits on planes (a) at 15° from {100}towards {111}, (b) {113}. Etchant A.



ETCH PIT DENSITY ON PLANES AT INCREASING ANGLES FROM (100) X 200

Figure 3.3. Etched with Etchant A. x 75.

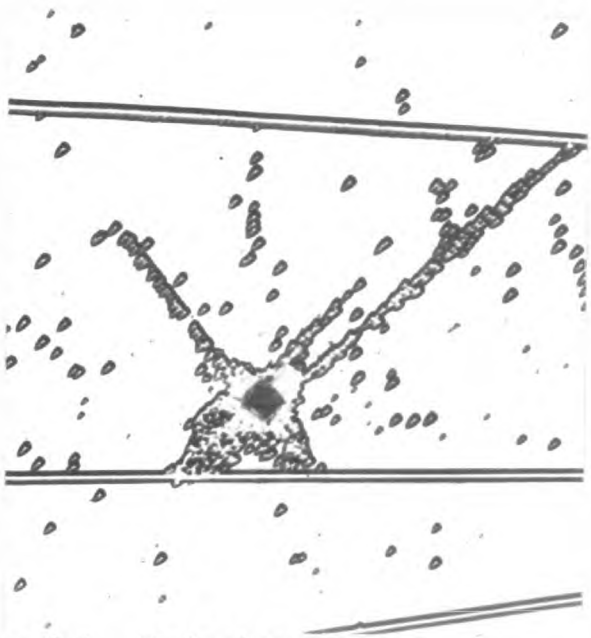


Figure 3.4. Etch pits near a microindentation on {113}. Etchant A. x 200.

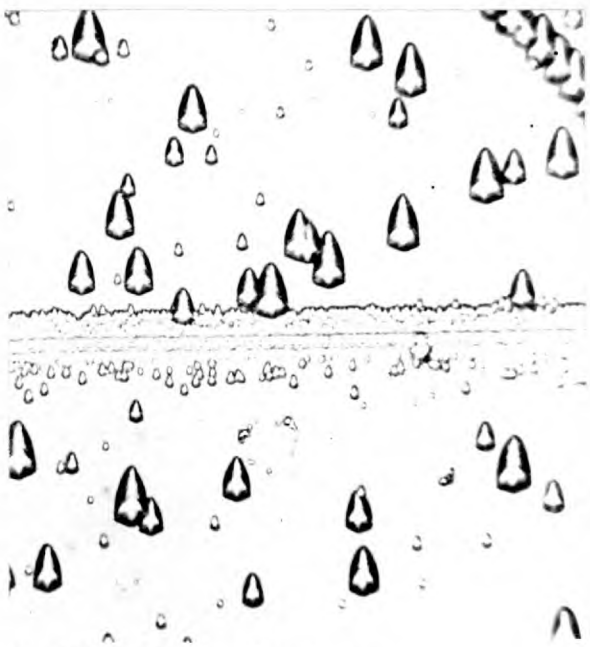


Figure 3.5. Etch pits near a scratch, oxalic acid electrolytic etch. x 200.

Another limitation of these etchants is that they cannot etch {112} planes (35^{o} from {100}) which is essential for the measurement of the velocity of pure edge dislocations on {110} planes. As the measurement of dislocation velocities was the main object of the present investigation there was the need to develop an etchant with better etching characteristics.

3.4. Development of a New Etchant

Many reagents used for electrolytic polishing can also be used for electrolytic etching at a reduced voltage and reduced current density. In the present investigation, the concentrated H_2SO_4 used for electrolytic polishing was unsuitable for electrolytic etching, but a solution of H_2SO_4 and CH_3OH which has also been used for electrolytic polishing was found to develop etch pits in molybdenum.

With an electrolyte containing 2 parts of H_2SO_4 and 1 part of CH_3OH, planes up to 32^{o} from {100} could be etched in the temperature range 70^{o} to $85^{o}C$ at 1.6 volts and 0.05 amp/cm.^{2} current density. The dislocations in the subgrain interior etched very poorly in comparison to those at the subgrain boundaries, but there was no rapid increase of etch pit density with increasing angle from {100}. Reducing the voltage below 1.6 volts did not produce any noticeable change in etching,

but when it was increased above 2.2 volts only subgrain boundaries got etched and at still higher voltages there was no etching at all.

With an electrolyte containing 1 part of H_2SO_4 and 1 part of CH_3OH the etching effects were very similar. At temperatures below 45°C there was no etching; between 45° and 60°C etching occurred only at subgrain boundaries at very low voltage and current density (≈0.01 amp/cm.^{2}). Satisfactory etching was possible at temperatures above 70°C and with increasing temperature higher voltage and higher current density were necessary for optimum etching effects. At 70°C, 1.6 volts and 0.06 amp/cm.^{2} current density produced the best etching effects whereas at 80°C the corresponding values were 2 volts and 0.1 amp/cm.^{2}. Increasing the voltage and current density above the optimum range resulted in the formation of small superficial pits in the background. Above 90°C only subgrain boundaries etched faintly.

Etching was improved considerably by the addition of chloric acid ($HClO_3$). Duan et al.[179] have used a solution of methanol, sulphuric acid and chloric acid (30:6:13 by volume) to develop etch pits on {111} planes in molybdenum.

With a solution containing 2 parts of $HClO_3$, 25 parts of H_2SO_4 and 25 parts of CH_3OH in the temperature range 65°-70°C planes up to 33° from {100} could be etched at ≈1.6 volts and

0.06 amp/cm.^{2} current density and the pits were quite well developed. However, the etching behaviour was further improved by increasing the proportion of $HClO_3$ in the etchant which was accompanied by a decrease in the optimum temperature range for etching.

When a solution containing 2 parts of H_2SO_4, 2 parts of CH_3OH and 1 part of $HClO_3$ was used, the etching was excellent at 48°-50°C, 2 volts and 0.12 amp/cm.^{2} current density and planes up to ≈35° from {100} could be etched. At lower temperatures etching was possible only at a lower voltage and current density and the range of etchable planes decreased. Etching was worse at higher temperatures.

Increasing the concentration of $HClO_3$ above 20% did not produce any more improvement in the etching characteristics except the lowering of the optimum temperature for etching. With equal parts of H_2SO_4, CH_3OH and $HClO_3$ the etching temperature was reduced to 22°-26°C at 2 volts and 0.3 amp/cm.^{2} current density. Etching was faster with etchants having a higher concentration of $HClO_3$.

3.5. Preparation of the Etchant and the Etching Process

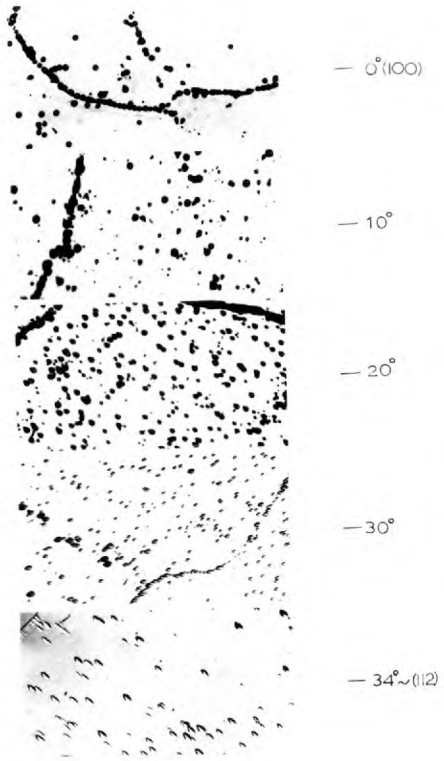
The heat of solution of H_2SO_4, CH_3OH and $HClO_3$ is very large and an explosion may occur unless sufficient precautions

are taken during the preparation of the etchant. First H_2SO_4 was added slowly to CH_3OH in a flask kept immersed inside ice, the solution being constantly stirred with a magnetic stirrer. Then the required amount of $HClO_3$ was taken in a dropping funnel and added drop by drop to the solution of H_2SO_4 and $HClO_3$ allowing sufficient time between successive additions so as to dissipate the heat produced during the process.

For etching, the specimen was electropolished, washed in methyl alcohol, dried and immersed for about 5 seconds in the etchant using a platinum cathode. Then it was rinsed in flowing distilled water, washed in alcohol and dried with a blower.

3.6. The Characteristics of the Etchant

The etching of the planes at increasing angles from {100} is shown in Figure 3.6. This etchant does not show the peculiar behaviour common to the other etchants. The etch pit density does increase slightly on planes away from {100}, but then it remains almost constant and shows a small decrease after 30° from {100}. Beyond {112} the pits become too shallow and faint to be observed under an optical microscope. Figure 3.7. shows the variation of etch pit density on planes with



ETCH PIT DENSITY ON PLANES AT INCREASING ANGLES FROM (100) X 200

Figure 3.6. Etched electrolytically in a solution of H_2SO_4, CH_3OH and $HClO_3$ (Etchant B). x 75.

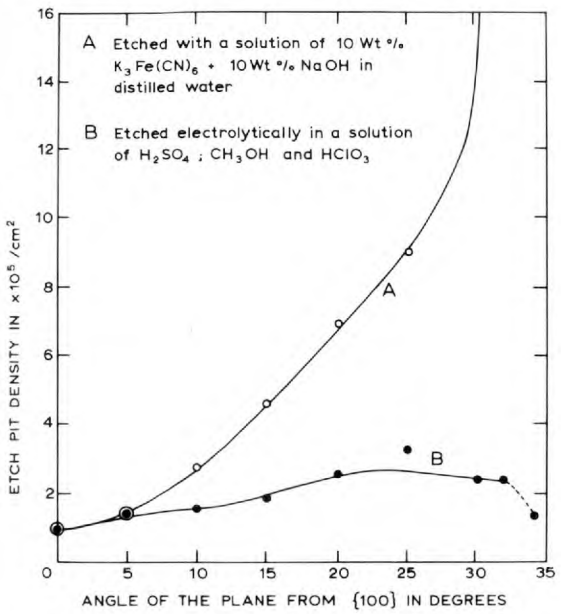


Figure 3.7. Variation of the etch pit density on planes with increasing angle from {100} towards {111} for the old and new etchants.

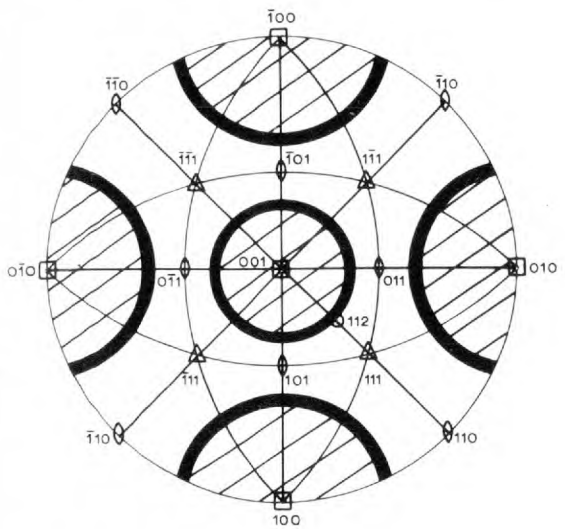
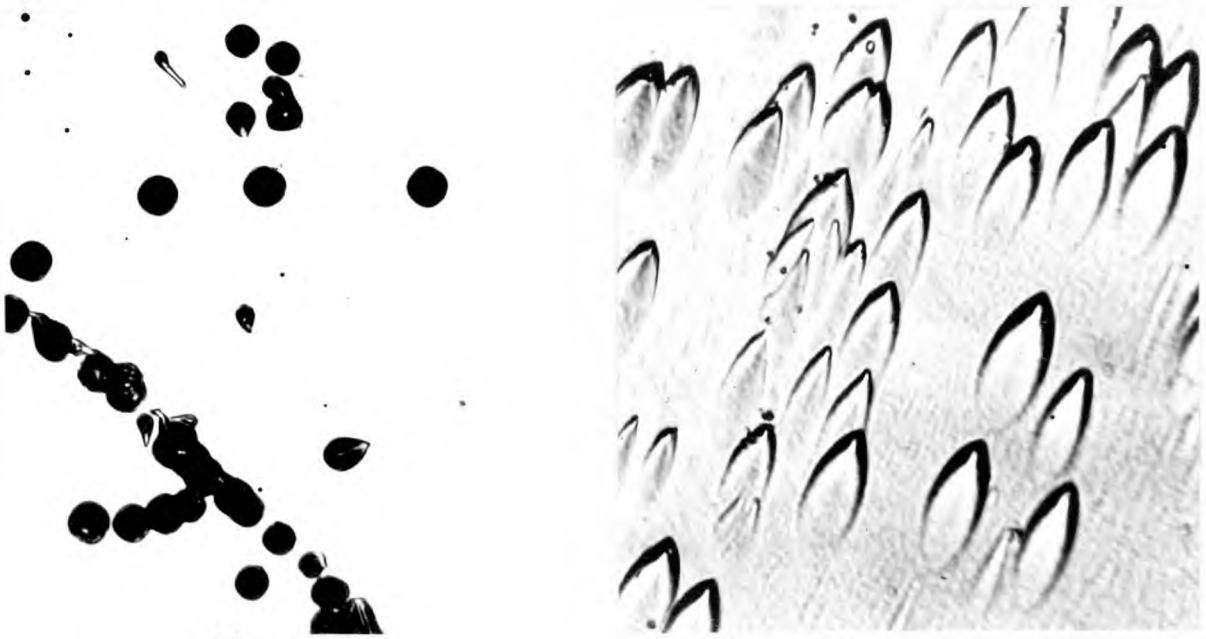


Figure 3.8. Standard (001) projection showing planes etchable by $K_3Fe(CN)_6$ + NaOH + H_2O (Chemical etch A) and H_2SO_4 + CH_3OH + $HClO_3$ (Electrolytic etch B). Cross hatched area = etchant A. Cross hatched + dark area = etchant B.

increasing angle from {100} for the old and new etchants. Figure 3.8. shows the range of planes in a standard (001) stereographic projection etchable by both types of etchants. This newly developed etchant does not need any decoration and can etch both grown in and fresh dislocations. The shape of the pits on {100} and a plane at 32^{o} from {100} towards {111} are shown in Figure 3.9.

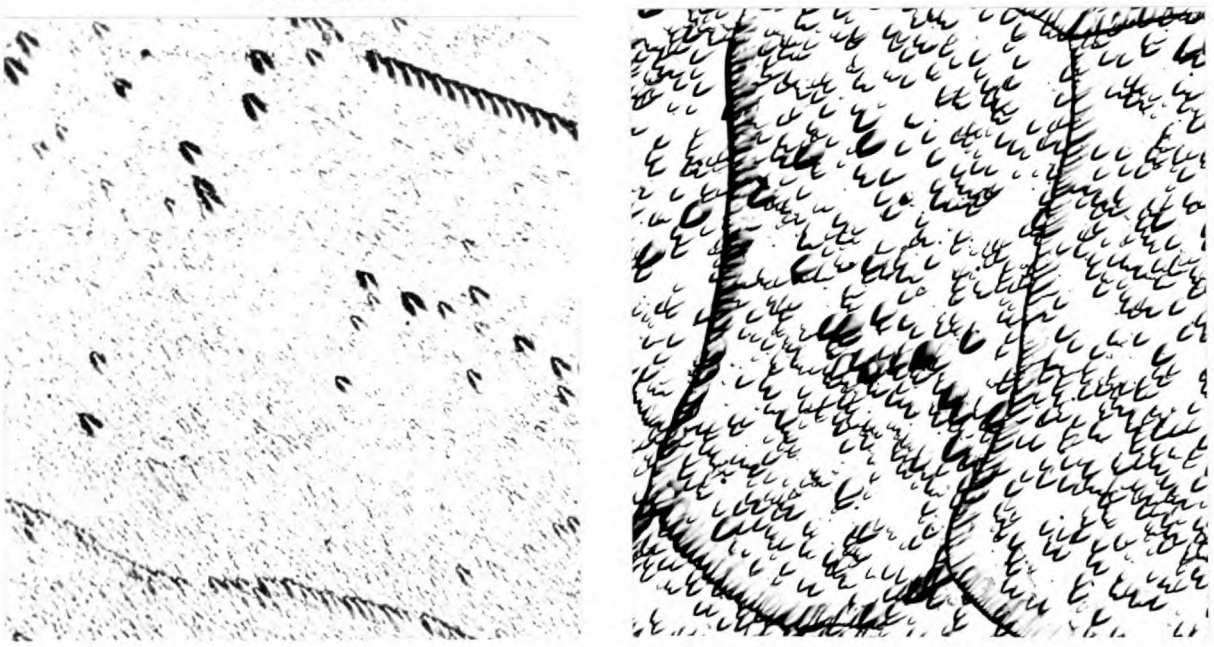
This etchant has certain other interesting characteristics. In a specimen with the surface considerably deformed by mechanical grinding or spark planing the grown in dislocations produce larger and more distinct pits than the fresh dislocations and this is observed even after a considerable amount of material has been removed from the surface by electropolishing (Figure 3.10). It is also noticed that dislocations at the subgrain boundaries etch better than those in the interior of the subgrains.

On etching a crystal grown from an arc cast, molybdenum rod some superficial small pits were formed in the background along with well developed pits (Figure 3.11.). These superficial pits are probably not due to dislocations, but result from the higher impurity content of these crystals.



(a) x 500 (b) x 500

Figure 3.9. (a) Etch pits on {100} plane, (b) on a plane at 32^{o} from {100} towards {111}, etched with etchant B.



(a) x 200 (b) x 200

Figure 3.10. a. Mechanically ground specimen etched after removing 0.035 mm. from the surface by electropolishing.
b. Spark machined specimen etched after removing 0.05 mm. from the surface by electropolishing.

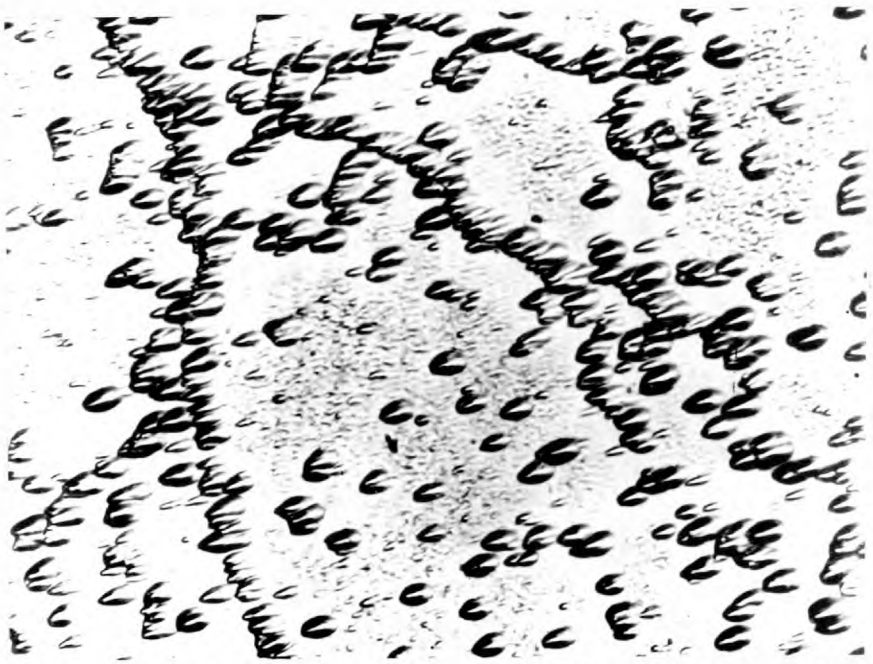
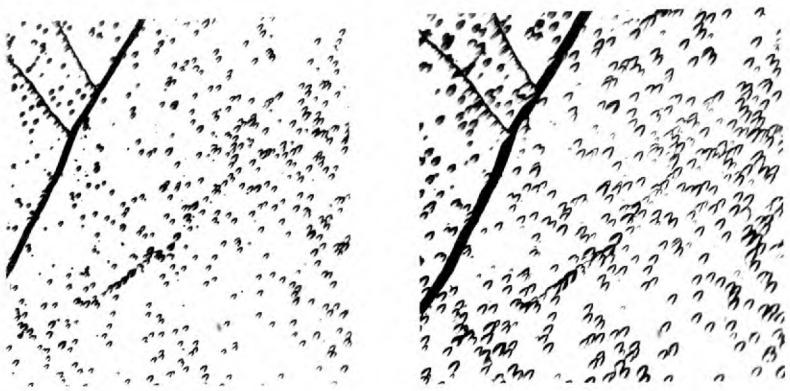


Figure 3.11. Etch pits on a plane at 30° from {100} towards {111} in a crystal grown from arc cast molybdenum.



(a) 200 X (b) 200 X

EFFECT OF ETCHING TIME ON THE ETCH PIT DENSITY ON A PLANE VERY CLOSE TO {112}

(a) ETCHED FOR 5 SECONDS

(b) ETCHED FOR 10 SECONDS

Figure 3.12. x 113.

3.6.1. Reliability of the Etchant

The reliability of this etchant has been investigated. Increasing the etching time resulted in larger pits with practically no increase in the density of pits (Figure 3.12.). When a micro-indentation was made on the surface of an annealed specimen, arrays of etch pits formed on etching, radiating from the indentation mark (Figure 3.13.). These pits represent dislocations which have been generated at the micro-indentation and subsequently moved and multiplied. The traces of these arrays were analysed by taking a Laue X-ray photograph of the specimen. The plane of observation was close to (112). The longer array was probably the trace of $(\bar{1}10)$ plane and the shorter ones along the traces of $(12\bar{1})$ and $(\bar{2}\bar{1}1)$ respectively as indicated in Figure 3.12. When a specimen was slightly deformed the density of etch pits increased and they were aligned along the trace of the slip plane (Figure 3.14.). The specimen was etched both before and after the application of load and the grown in dislocations show much larger pits because they have been etched for a longer time.

During spark machining, cleavage occurred in two single crystals. It is rather unusual that cleavage should occur in molybdenum single crystals at room temperature. However, one may expect that a dislocation threading through a cleavage plane

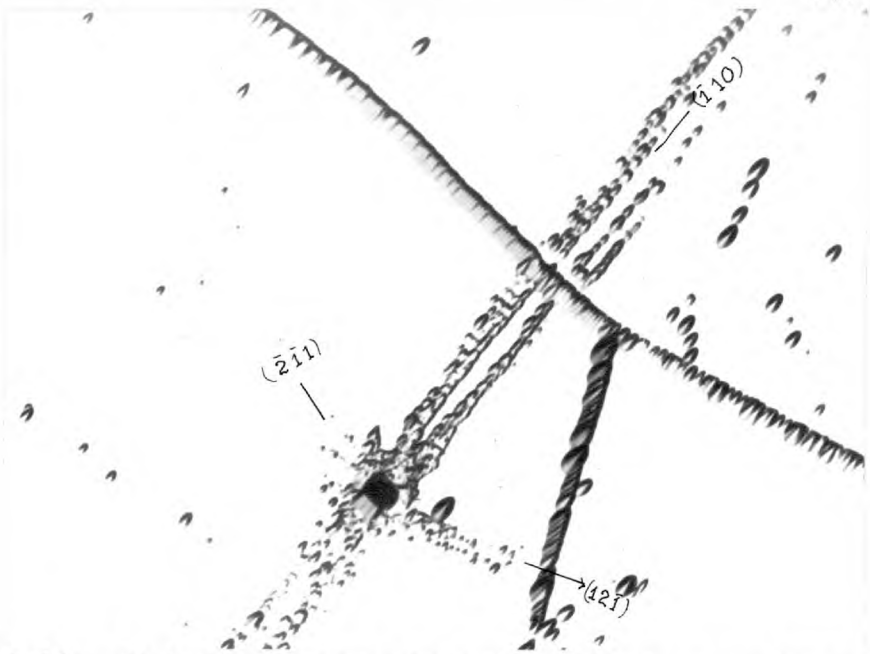


Figure 3.13. Etch pits near a micro-indentation on a plane close to (112) (etched with etchant B). x 200.



Figure 3.14. Alignment of the etch pits along the trace of slip planes in a slightly deformed specimen. x 200.

would produce etch pits on both the cleaved surfaces, when etched, and the etch pit distribution on one face should be the mirror image of the other. This is shown in the photographs of the matching halves of the cleaved crystal (Figure 3.15.). The cleavage surface is {100} and one to one correspondence between etch pits seems reasonable. There are no dark areas of high pit density as observed in tungsten single crystals by Schadler[165]. Probably the cleavage crack has travelled faster than the critical velocity, thus avoiding appreciable plastic deformation at the surface.

Nye's relation (equation 3.1.) discussed in section 3.2. has been verified for the present etchant. Two specimens having the orientation and geometry shown in Figure 3.16. were bent about an axis close to $[112]$ to radii of 13 ± 1 cm. and 18 ± 1 cm. respectively. The shear stress was maximum on $(1\bar{1}0)$ $[\bar{1}\bar{1}1]$ slip system and the dislocations emerging on the side face close to (112) were almost pure edge in character. The initial dislocation density was $\simeq 6 \times 10^4$ cm.^{2} in both specimens. After the bending the increase in pit density at the neutral axis on (112) plane was negligible, but the mean dislocation densities were $\simeq 1.037 \times 10^7$ per cm^2 in specimen A, bent to 13 ± 1 cm. radius and 9.024×10^6 per cm.^{2} in specimen B, bent to 18 ± 1 cm. radius. Figure 3.17. shows the region near the neutral axis in specimen B and a region of average

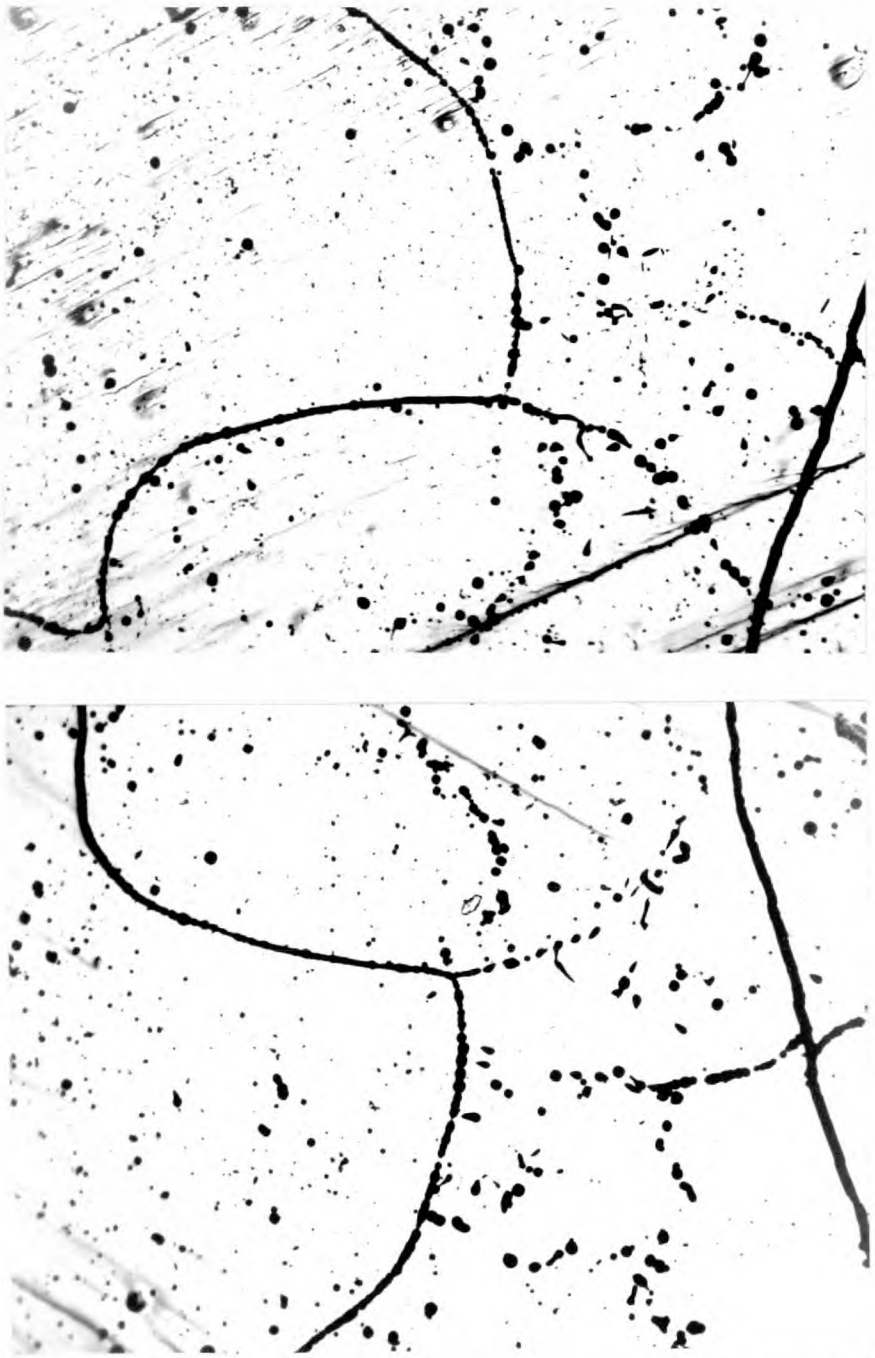


Figure 3.15. Cleavage surface of a molybdenum single crystal showing two matched faces etched by etchant B. x 200.

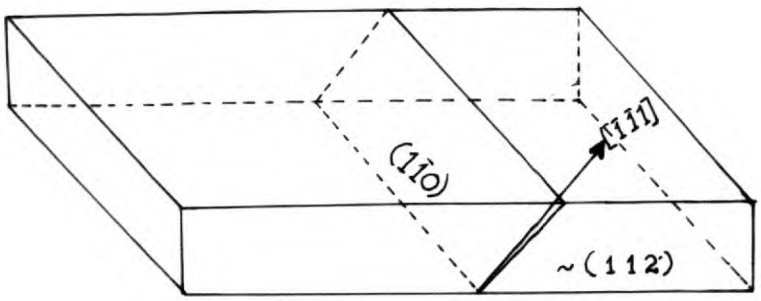


Figure 3.16. Schematic representation of the specimen geometry used for verification of Nye's relation in bent crystals.

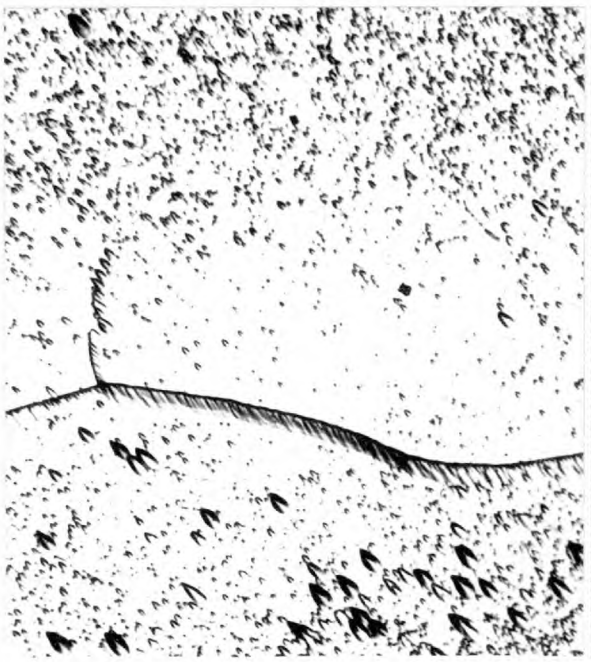


Figure 3.17. (a) Etch pits near the neutral axis on the ≃(112) surface of specimen B, bent about ≃[112] axis to a radius of 18 ± 1 cm. x 200

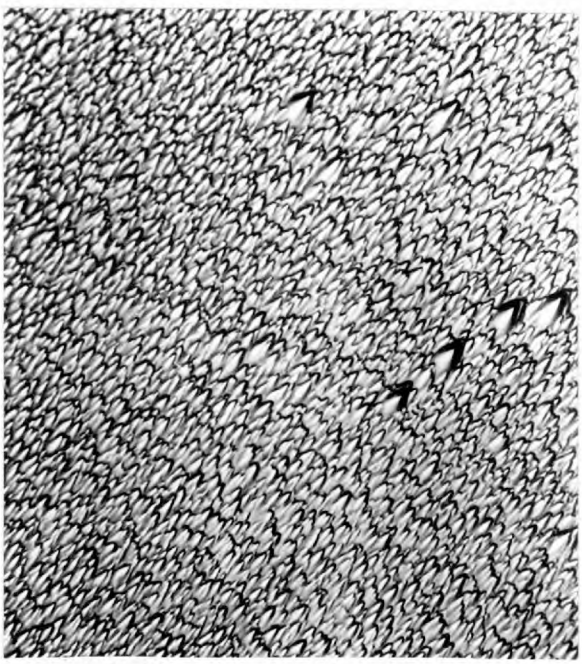


Figure 3.17. (b) Etch pits near a region of average strain on the ≃(112) surface of specimen A bent about ≃[112] axis to a radius of 13 ± 1 cm. x 200.

dislocation density in specimen A. This mean density after bending was higher than that predicted by Nye's formula. However, after annealing these bent specimens at 1500°C in vacuum for 6 hours, the dislocation density was much reduced (Figure 3.18) and there was no further significant reduction in the dislocation density when the specimens were re-annealed at 2000°C for 10 hours (Figure 3.19.). The values of etch pit density in bent and annealed specimens along with the dislocation density predicted by equation 3.1. are given in Table 3.1. The agreement between the experimental results and the predicted values is satisfactory confirming the correspondence between dislocations and etch pits.

Table 3.1.

Specimen	A	B
Etch pit density after bending	$1.037 \times 10^7/cm.^2$	$9.024 \times 10^6/cm.^2$
Etch pit density after annealing at 1500°C for 6 hours	$3.045 \times 10^6/cm.^2$	$2.368 \times 10^6/cm.^2$
Etch pit density after annealing at 2000°C for 10 hours	$2.24 \times 10^6/cm.^2$	$1.36 \times 10^6/cm.^2$
Theoretical dislocation density	$3.99 \times 10^6/cm.^2$	$2.88 \times 10^6/cm.^2$



Figure 3.18. Etch pits on ≈(112) surface of specimen A after annealing at 1500°C for 6 hours. x 500.

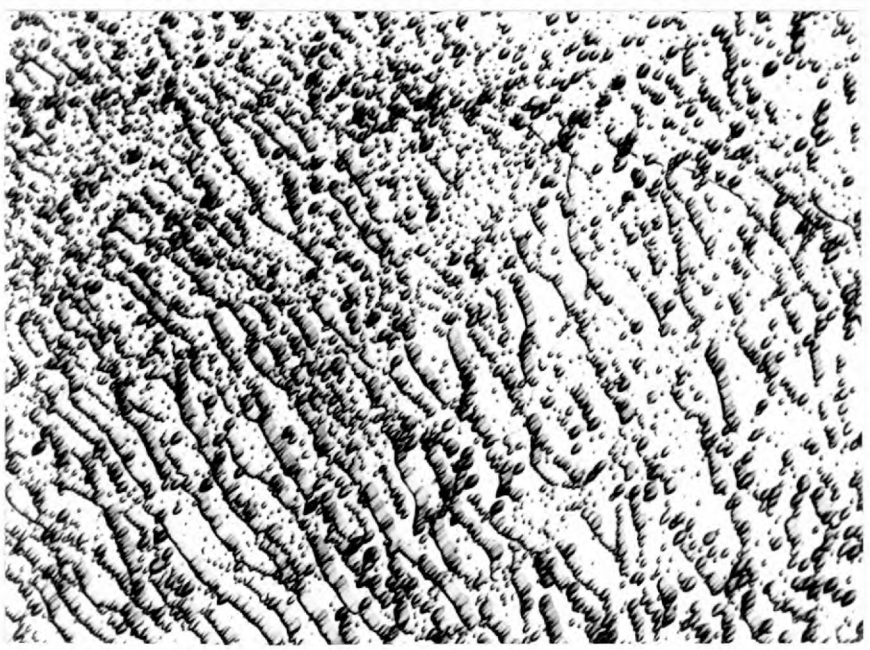


Figure 3.19. Etch pits on ≈(112) surface of specimen A after annealing at 2000°C for 10 hours. x 200.

3.7. Discussion

This etchant can etch both grown in and fresh dislocations on planes within 35^{o} of {100} without any prior decoration. However, the larger pits produced at the sites of grown in and aged dislocations suggest that decoration by interstitial impurities may be playing some additional role in the etching of dislocations in molybdenum single crystals, by this etchant. This etchant seems to have better etching characteristics than any other for molybdenum because of the large range of planes which are etchable and the consistency of the dislocation density on these planes. For a specimen having the geometry shown in Figure 3.15., Burgers vector $[\bar{1}\bar{1}1]$ is almost perpendicular to the top face and parallel to the side face, so dislocations with $[\bar{1}\bar{1}1]$ Burgers vector moving on $(1\bar{1}0)$ plane and emerging on the top face should be pure screw and those on the side face pure edge. As this etchant can etch both the faces it seems that both the screw and edge components are etchable by this etchant.

Glide polygonisation observed by Livingstone[22] in copper and by Schadler[165] in tungsten also occurs in molybdenum single crystals. In Figure 3.20. of the bent single crystal near neutral axis there is an alignment of pits perpendicular to the glide plane 'S'. There is a strong tendency for polygonisation during annealing of deformed crystals as is evident from

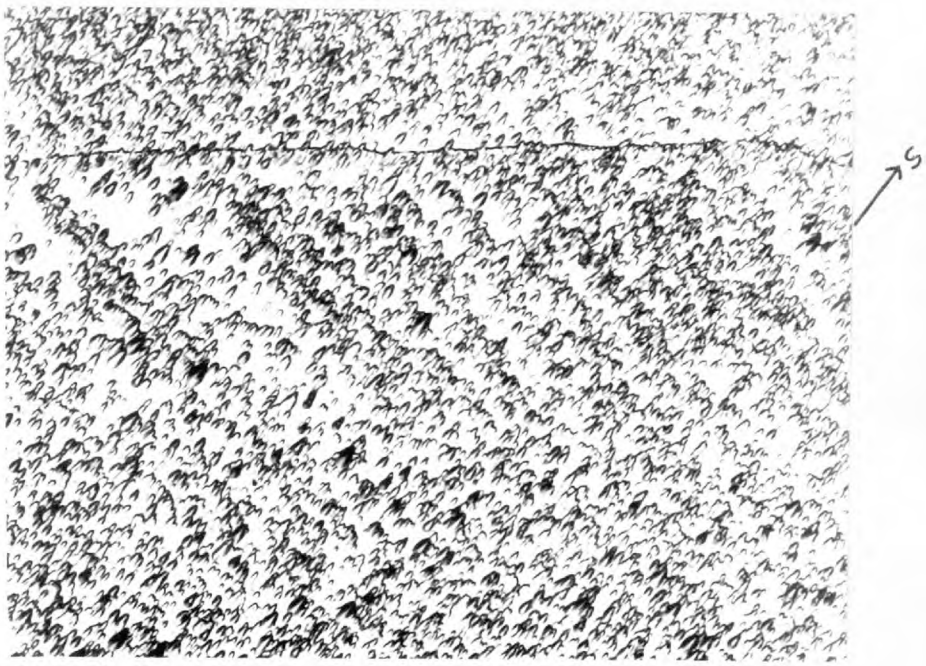


Figure 3.20. Etched surface close to (112) in the bent specimen A showing glide polygonisation. S = slip direction. x 200.

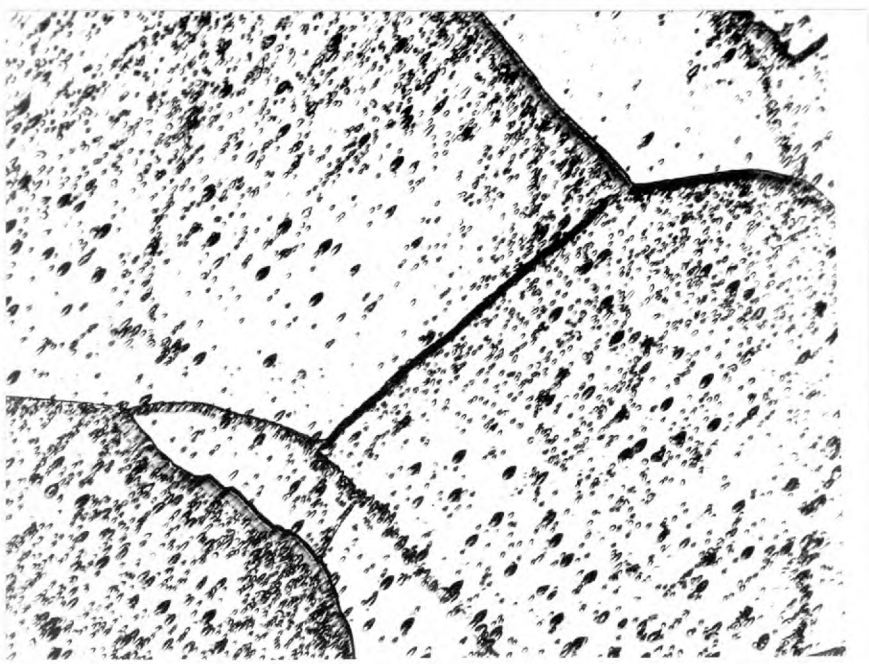


Figure 3.21. Pile up of dislocations at subgrain boundaries in a specimen deformed at 77°K. x 100.

Figure 3.18.

It is possible to study a number of interesting aspects of dislocation arrangement and plastic deformation in molybdenum single crystals with this etchant. They include pile up of dislocations at subgrain boundaries (Figure 3.21.), determination of slip systems operating at different temperatures from the alignment of etch pits on two perpendicular surfaces of a slightly deformed specimen and the measurement of dislocation mobility at different stresses and temperatures.

CHAPTER 4

PREPARATION AND ANNEALING OF SPECIMENS

4.1. Introduction

Dislocation mobility and plastic deformation studies in single crystals necessitates the preparation of specimens without introducing any appreciable amount of fresh dislocations. Most ionic crystals can be easily cleaved along certain crystallographic planes and thus specimens with very little plastic deformation can be obtained. Also the grown-in dislocation density in these crystals is rather low in comparison to metallic single crystals. Preparation of metal single crystal specimens especially for dislocation velocity measurement needs the utmost care and precaution and up to date three methods are available for this purpose:

1. Slow mechanical grinding[180, 181].
2. Spark machining[182, 106].
3. Chemical and electromachining[183, 184, 139].

Of these, the first two introduce a thin deformed layer at the surface, the depth of which depends on the rate of grinding or spark machining along with the surface condition of the tool. The coldworked layer is later removed by chemical or electropolishing. The third method does not introduce any plastic deformation, but it takes rather a long time when single crystals

of large diameters are to be machined. Besides it is not always possible to obtain single crystals of uniform cross section, which is a desirable condition for efficient chemical or electropolishing. Finding a suitable electrolyte or chemical reagent is another problem. Specimens for dislocation velocity measurement should have a rectangular cross section with flat faces. It is very difficult and often impossible to machine such specimens by electrolytic or chemical means.

Spark machining takes much longer time than mechanical grinding. The surface of the spark planing tool gets eroded rapidly during machining and has to be frequently ground flat so as to produce a flat and smooth specimen surface. These drawbacks of spark machining initially prompted the use of surface grinding for specimen preparation.

4.2. Machining of Specimens by Surface Grinding

For machining bending specimens, the single crystal was set in a two circle goniometer (Figure 2.4.) and an X-ray Laue photograph was taken. After indexing the Laue photograph the crystal was rotated through the necessary angle about the east-west axis so as to bring the plane of observation for dislocation velocity measurement, parallel to the base plate of the goniometer. Then the single crystal was set in a mild steel tray encased in

Wood's alloy (Figure 4.1.) and ground flat by a self cleaning alumina wheel to a depth of about 1.6 mm. The rate of grinding was 0.0012 mm. per each cut, but while removing the last 0.125 mm. the wheel had four passes per each cut.

The single crystal rod with one face ground was cut with a carborundum slitting wheel to lengths of about 25 mm. These pieces were set in Wood's alloy with their machined face down in a mild steel tray and the opposite face was ground in a similar way. Finally the side faces were ground by holding them in a jig. The finished specimens had a rectangular cross section of 2.6 mm. x 4.2 mm. and a length of 25 mm. Few tensile specimens were also machined by a mechanical grinding method described by Guiu[157].

4.3. Polishing of Specimens

The deformed surface layer produced by grinding was removed by electrolytic polishing in concentrated sulphuric acid at 12 volts and a current density of ≈0.75 amps/cm.^{2}. The cathode consisted of two sheets of platinum held parallel at a distance of 2 cm. by platinum wires. The temperature of the electrolyte was maintained below 40^{o}C and the specimen was constantly stirred. This helped in stabilising the current and produced a smooth surface free from waviness and pits. The



Figure 4.1. Setting the single crystal in Wood's alloy after giving it the necessary rotation with the goniometer.

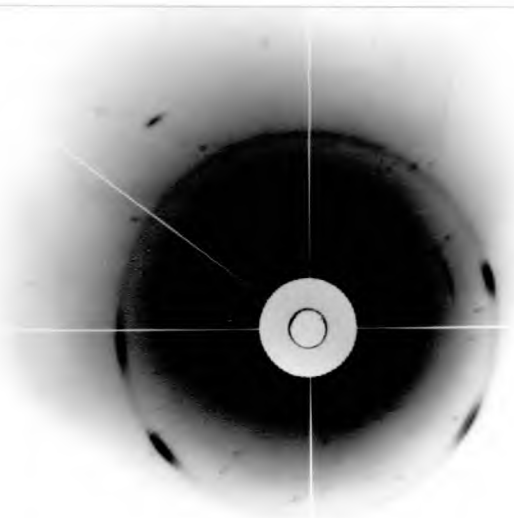


Figure 4.2. Back reflection Laue photograph of a specimen (prepared by mechanical grinding) in the as machined condition.

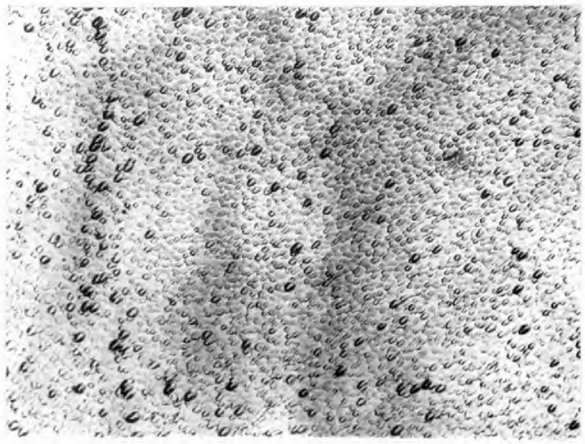
back reflection Laue photograph of the as machined sample showed well defined continuous Debye rings and some amount of asterism (Figure 4.2.), but after removing 0.025 mm. from the surface by electropolishing the rings and asterism disappeared. However, a more accurate and sensitive method for determining the thickness of the deformed layer introduced during machining is by dislocation etch pitting. The specimen was etched after removing different depths of material from the machined surface. It is found in Figure 4.3. that the etch pit density decreases with increasing depth below the machined surface and remains constant after about 0.18 mm. has been removed from the surface. However, it is difficult to confirm whether this density is the same as the grown in dislocation density in the crystal.

4.4. Preparation of Specimens by Spark Machining

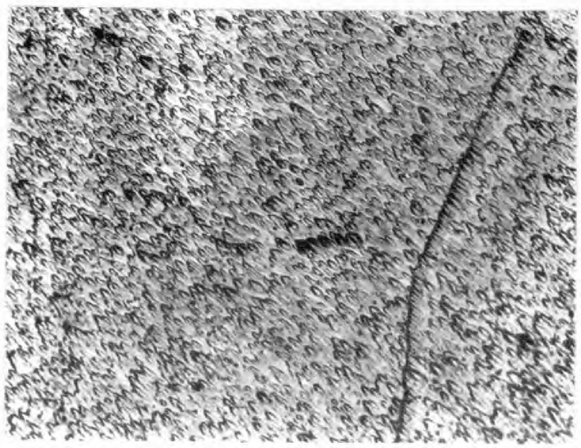
Some preliminary experiments to measure the mobility of dislocations were performed with specimens machined by surface grinding, but high dislocation density was always a problem even after long annealing at very high temperatures. This may have been due to the high plastic deformation introduced during mechanical grinding. It was, therefore, dedided to find out whether this difficulty could be overcome with spark machining.



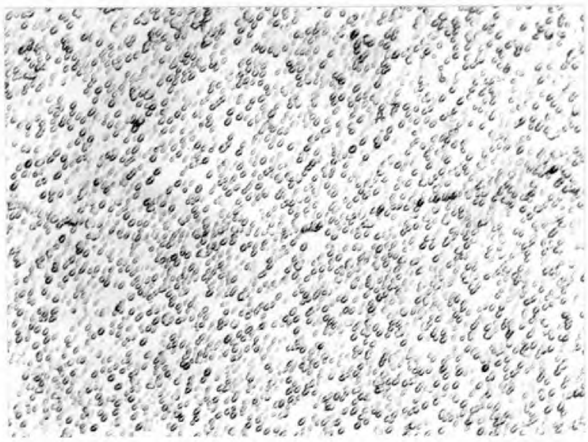
(a) x 200



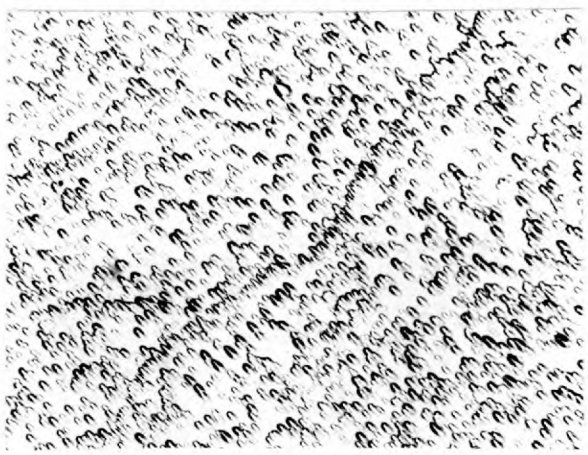
(b) x 200



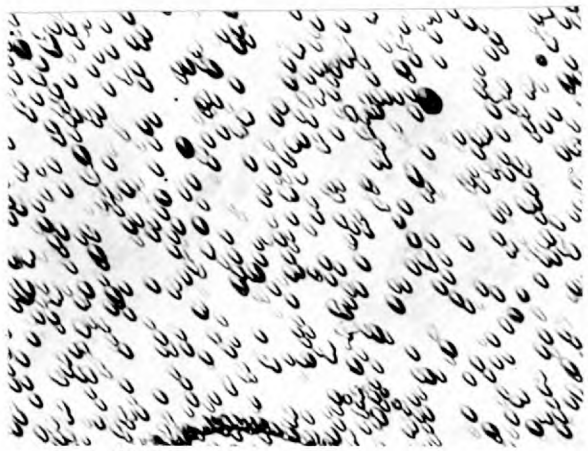
(c) x 200



(d) x 200



(e) x 200



(f) x 200

Figure 4.3. Dislocation etch pits at different depths below the machined surface of a mechanically ground specimen. Depths: (a) 0.035 mm. (b) 0.065 mm. (c) 0.085 mm. (d) 0.115 mm. (e) 0.150 mm. (f) 0.180 mm.

4.4.1. Machining of Bending Specimens

The single crystal was set in Wood's alloy after rotating it through the necessary angle with the goniometer as described in section 4.2. and it was spark planed in a Servomet sparking machine manufactured by Metals Research Limited, Cambridge. A brass disc of 6" diameter was used as a tool. The initial planing was done at a coarse setting of '4', but the finishing stages were carried out with a refaced tool for about one hour at each of the ranges 5, 6 and 7 respectively.

Then the crystal was cut into lengths of about 25 mm. with a carborundum slitting wheel and the cut pieces were set radially with their flat face down in another tray encased in Wood's alloy (Figure 4.4.). This arrangement facilitated the uniform machining of specimens. After machining the opposite face the specimens were held in a special jig (Figure 4.5.) and the side faces were machined by spark planing as before. The specimens have the average dimension of 2.8 mm. x 4.1 mm. x 25 mm.

The Laue X-ray photograph of the spark machined specimen (Figure 4.6.) shows traces of very faint Debye rings which disappear when 0.005 mm. is removed from the surface by electropolishing. This indicates the superiority of this method over mechanical grinding. The extent of surface damage was also determined by repeated electropolishing and etching.



Figure 4.4. A batch of specimens with one face spark planed is set in Wood's alloy for machining the opposite faces.

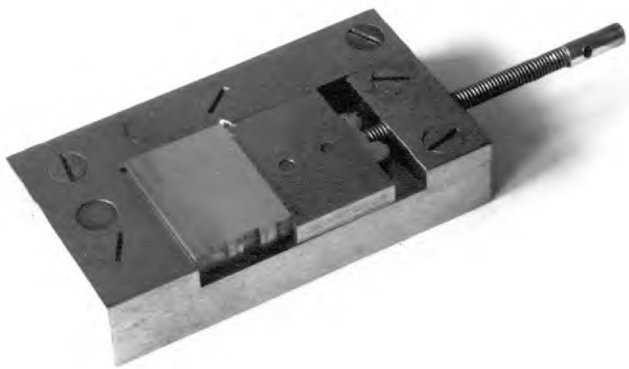


Figure 4.5. Special jig to hold bending specimens during the machining of the side faces.

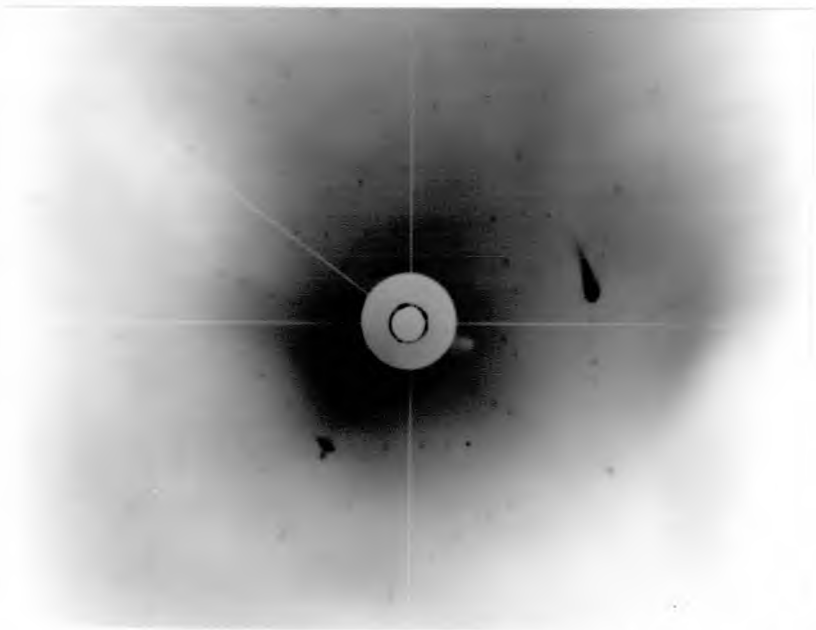
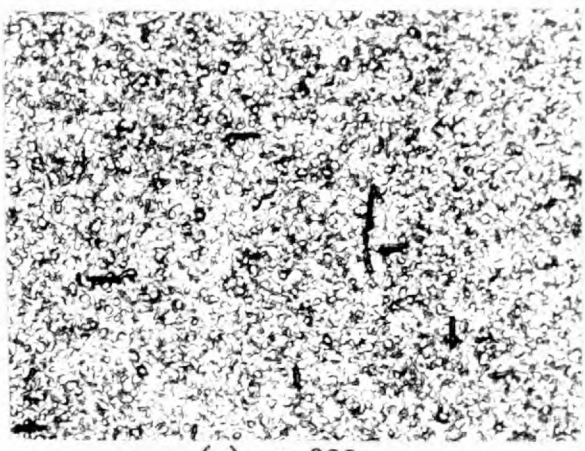


Figure 4.6. Back reflection Laue photograph of a specimen (prepared by spark planing) in the as machined condition.

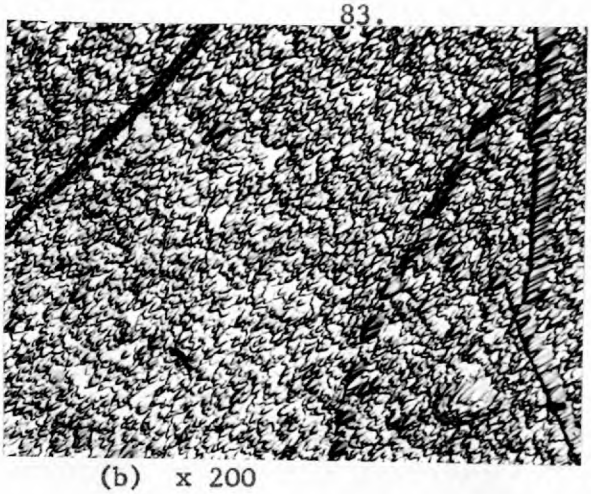
Figure 4.7. shows the distribution of dislocation etch pits after different depths of material have been removed from the spark machined surface. The dislocation density has been plotted against depth for both kinds of machining (Figure 4.8.). It is found that the thickness of the deformed layer is much less in the spark machined specimen than in the mechanically ground specimen.

4.4.2. Machining of Tensile Specimens

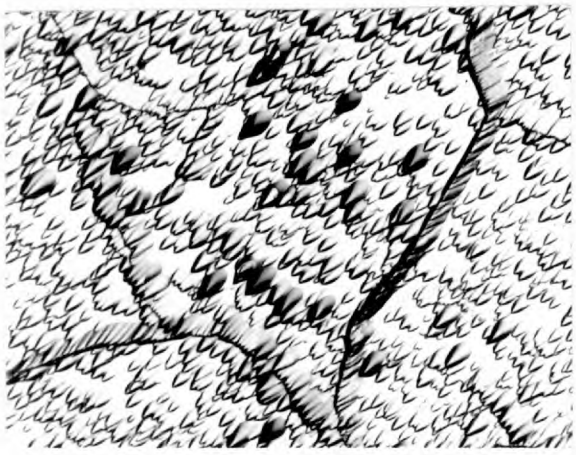
Tensile specimens of rectangular cross section are preferable for the study of the slip systems and dislocation structure during plastic deformation. However, the preparation of such specimens with a uniform cross section by spark machining was a difficult problem and a special tool holder was constructed for this purpose. The tool was a ½" x ½" x 4" elkonite 20-W-3 rod which could slide in the tool holder and be held by screws. Elkonite is a very hard material and lasts seven times as long as brass during spark machining. The single crystal was initially machined on four sides as described in section 4.4.1. The slabs thus produced were clamped in a special device shown in Figure 4.9. in batches of six and machining was continued across the length of the slabs. The set-up for machining tensile specimens is shown in Figure 4.10.



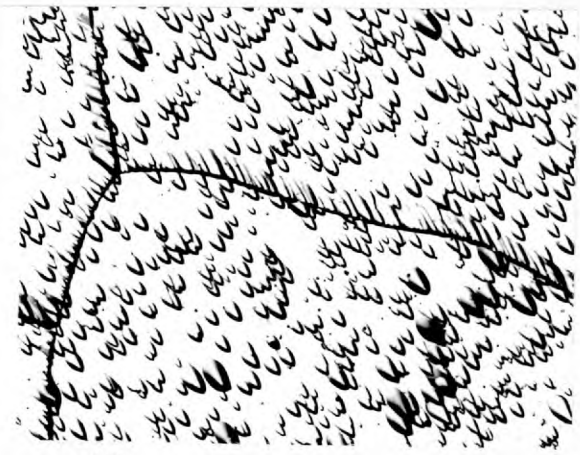
(a) x 200



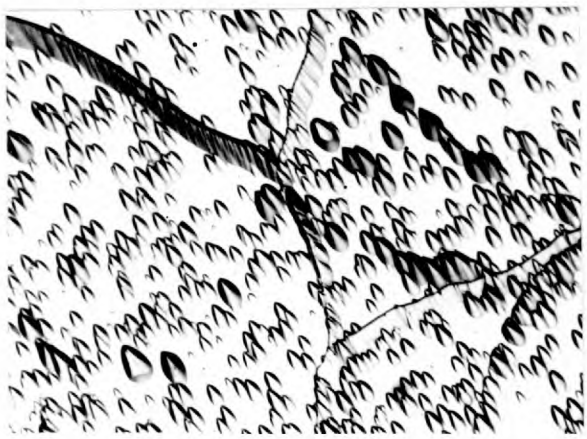
(b) x 200



(c) x 200



(d) x 200



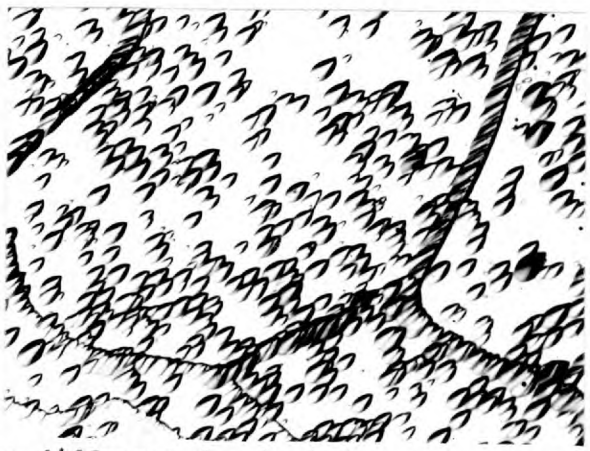


Figure 4.7. Dislocation etch pits at different depths below the machined surface of a spark planed specimen. Depths: (a) 0.001 mm. (b) 0.025 mm. (c) 0.050 mm. (d) 0.075 mm. (e) 0.100 mm. (f) 0.150.

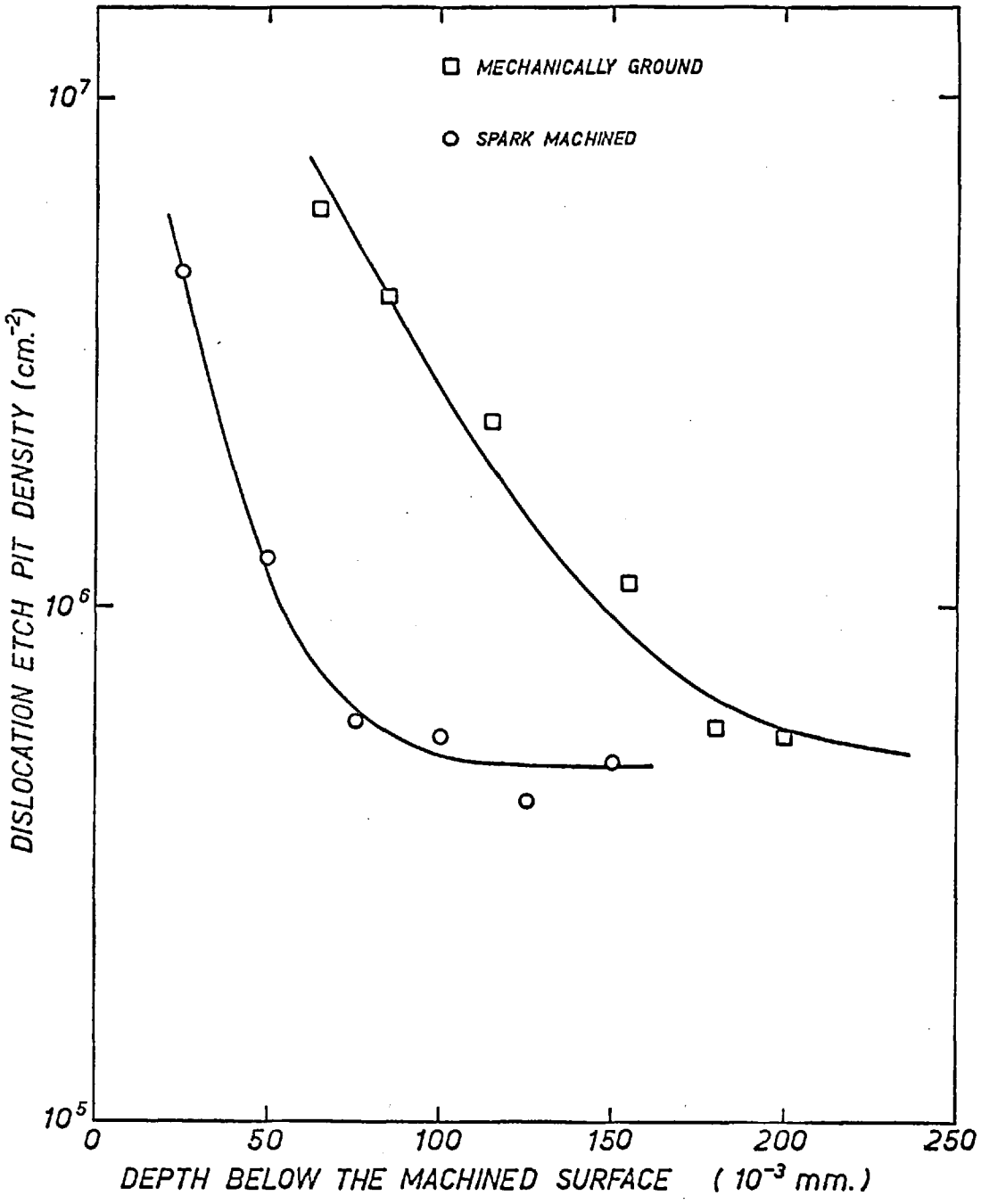


Figure 4.8. Etch pit density at various depths below the machined surface.



Figure 4.9. Special jig to hold tensile specimens during spark machining.

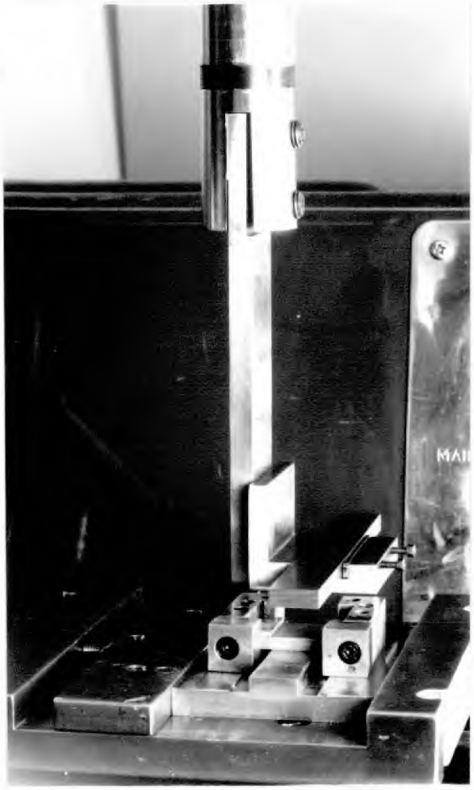


Figure 4.10. Set-up for machining tensile specimens in the Servomet sparking machine.



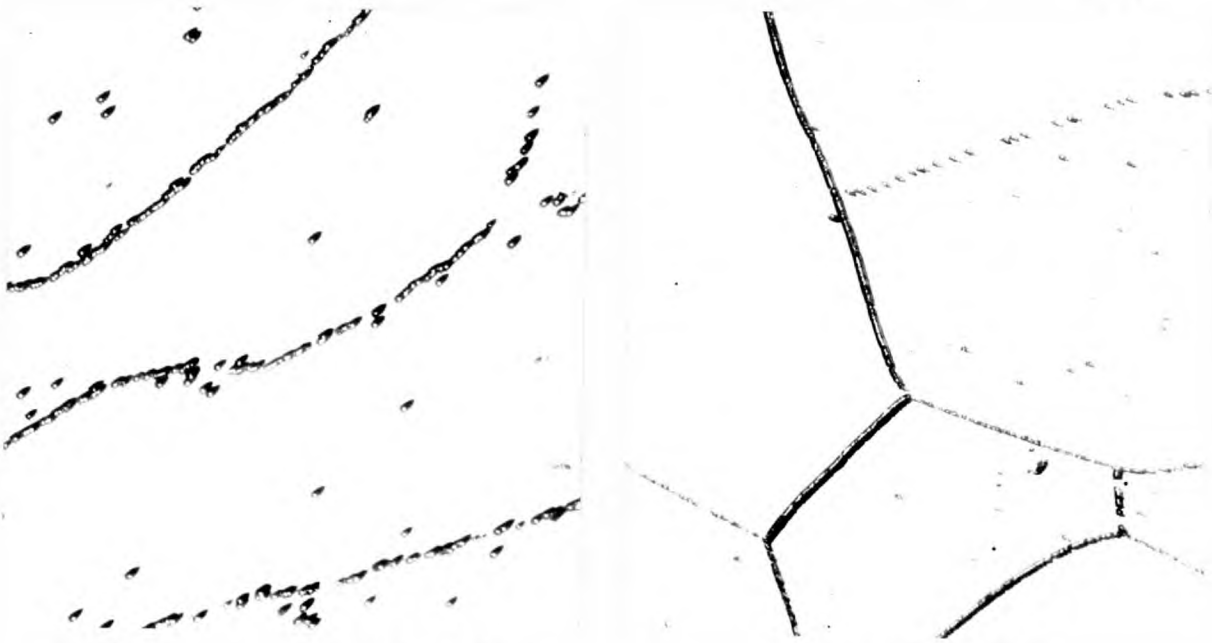
Figure 4.11. Two electropolished single crystal specimens for bending and tensile tests.

The specimens thus obtained have an overall length of 23 mm. with a guage length of 12.6 mm. and a rectangular cross section of ≈2.8 x 2.2 mm. About 0.125 mm. was removed from the surface by electropolishing. A bending specimen and a tensile specimen after electropolishing are shown in Figure 4.11.

4.5. Annealing of Specimens

It was necessary to reduce the grown in dislocation density in the molybdenum single crystal specimens by annealing before any dislocation velocity measurement could be made. So after the removal of the cold worked surface layer by electropolishing the specimens were given different annealing treatments before selecting one which would produce the optimum results.

Annealing at 1500°C and at a pressure of ≈1 x 10^{-5} torr in a vacuum furnace did not produce any appreciable change in the dislocation density. Then a specimen was annealed in the leectron beam floating zone melting furnace at a temperature close to the melting point for two hours. This resulted in a remarkable decrease in the dislocation density (Figure 4.12.), but the specimen used to bend at the high temperature, there were too many subgrains, and the annealing process itself was



(a) x 200 (b) x 200

Figure 4.12. Dislocation etch pits in specimens annealed close to the melting point in the electron beam zone-melting furnace for two hours.



Figure 4.13. Dislocation etch pit bands indicating plastic deformation in specimens wrapped in tantalum foil during annealing in Balzers furnace. x 100.

not convenient.

Finally specimens were annealed in a Balzers high vacuum furnace with a tantalum foil heating element. When the specimens were left uncovered they were coated with a black deposit. It was extremely difficult to remove this deposit by electropolishing. Excessive evaporation of material from the specimen surface was another problem. These difficulties were overcome by wrapping the specimens in thin tantalum foils and holding them in a tantalum crucible, but sometimes the specimens were deformed during annealing at high temperatures (Figure 4.13.). Also a considerable pick-up of tantalum from the wrapping was very probable. So it was decided to hold the specimens free in compartments in a molybdenum crucible which was itself placed inside a larger tantalum crucible. The outer crucible was suspended from the centre of the top radiation shield by a tantalum wire.

The effect of temperature and annealing time on the etch pit density is shown in Figure 4.14. Figure 4.15. shows the dislocation structure in a specimen annealed for different lengths of time at 2200°C. It is found that most of the decrease in dislocation density occurs during the first few hours of annealing. All the specimens used for the present investigation were annealed at 2200°C for 25 hours at a pressure of $\approx 3 \times 10^{-6}$ torr. Polygonisation of dislocations occurred during the annealing of deformed specimens (Figure 4.16.).

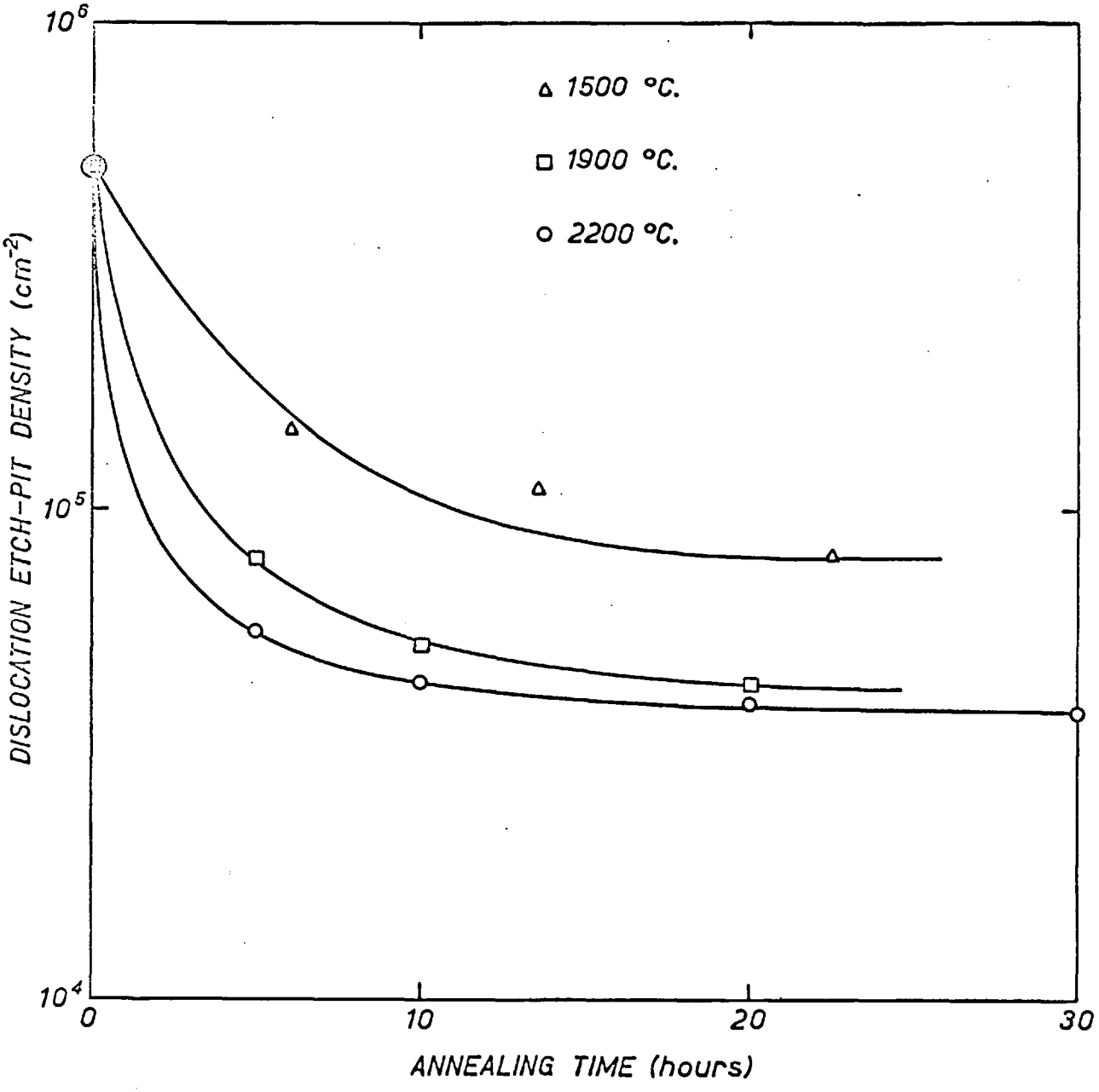


Figure 4.14. Effect of annealing time and temperature on the dislocation density.



(a) x 200



(b) x 200



(c) x 200

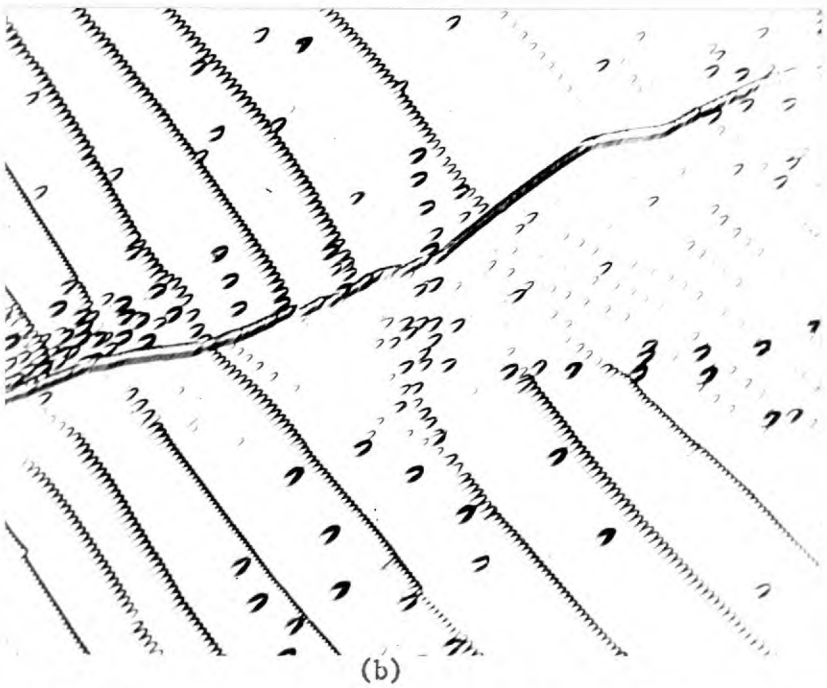


(d) x 200

Figure 4.15. Dislocation etch pits on a specimen annealed at 2200°C for (a) 5 hours; (b) 10 hours; (c) 20 hours; (d) 30 hours.



(a)



(b)

Figure 4.16. Polygonisation of dislocations in deformed crystals during annealing at 2000°C.

a. Specimen bent to 13 ± 1 cm. radius. Strain on the observation plane ≃10%.

b. Specimen stressed slightly above yielding.

CHAPTER 5

YIELDING AND FLOW OF MOLYBDENUM SINGLE CRYSTALS

5.1. Introduction

In recent years considerable work has been done on the temperature strain rate and orientation dependence of yielding and flow in b.c.c. metal single crystals. The main problem has been the determination of the operating dislocation mechanism and the crystallography of slip[106, 121, 127, 133, 180, 181]. The effect of impurities has also been extensively studied[114, 123-125, 185]. A fair amount of information on the plastic deformation behaviour of molybdenum single crystals has been obtained by Lawley and co-workers[64. 122], Guiu and Pratt[186] and Stein[185]. It is well known that dislocation mobility and multiplication play a very important role in the plastic deformation of the b.c.c. metals. Also the initial dislocation density (both grown-in and mobile) and structure may have a significant effect on the yielding and flow of these metals. Most of the work on molybdenum single crystals has been done with specimens having a dislocation density of $\simeq 10^6/cm.^2$ and very little data is available in the literature on the plastic deformation behaviour of metal single crystals of low dislocation density. So it was decided to investigate the effects of a very low initial dislocation density

on the yielding and flow of molybdenum single crystals.

Guiu[157] has studied the deformation behaviour of molybdenum single crystals grown under identical conditions, but his specimens were machined by mechanical grinding and had a dislocation density approximately 30 times higher than that of the annealed specimens used for the present investigation. This would provide a very good comparison of results so as to determine the effect of initial dislocation density on the deformation characteristics of molybdenum single crystals.

5.2. Experimental Techniques

The growth of molybdenum single crystals and the machining of specimens has been described in Chapters 2 and 4. The annealed specimens were electropolished to remove any oxide layer on the surface, formed during the long annealing at the high temperature. The tensile specimens had the following dimensions before testing: cross sectional area of ≈2.5 mm. x ≈2.1 mm. and a guage length of ≈12.7 mm. A floor model T.T-CM Instron machine with 500 kg. and 5000 kg. load cells was used for the tensile tests. The cross head speed in this machine could be varied between 0.005 cm./min. and 50 cm./min.

A frame made of nickel plated mild steel was mounted below the mobile cross head for tests at temperatures other than the

room temperature. Figure 5.1. shows this frame along with a tensile specimen held in special grips. This permitted the complete immersion of the specimen and the grip assembly in the constant temperature bath contained in a large Dewar flask. The temperature baths used are listed in Table 5.1.

Table 5.1.

Temperature ^{o}K	Bath Used
77	Liquid nitrogen
153	Isceon-12 (CCl_2F_2) cooled with liquid nitrogen
193	Isceon-12 cooled with liquid nitrogen
243	Boiling Isceon-12
273	Water and ice
373)	Silicon oil bath heated with an electric
)	
433)	resistance heater

The temperature was maintained within $\pm$ 1^{o}C at all temperatures. A pentane thermometer was used to measure temperatures below 273^{o}K and a mercury thermometer for temperatures above 273^{o}K. The thermometer bulb was placed very close to the specimen for accurate measurements. Before starting a test the specimen was left in the bath for at least 15 minutes so as to reach equilibrium.

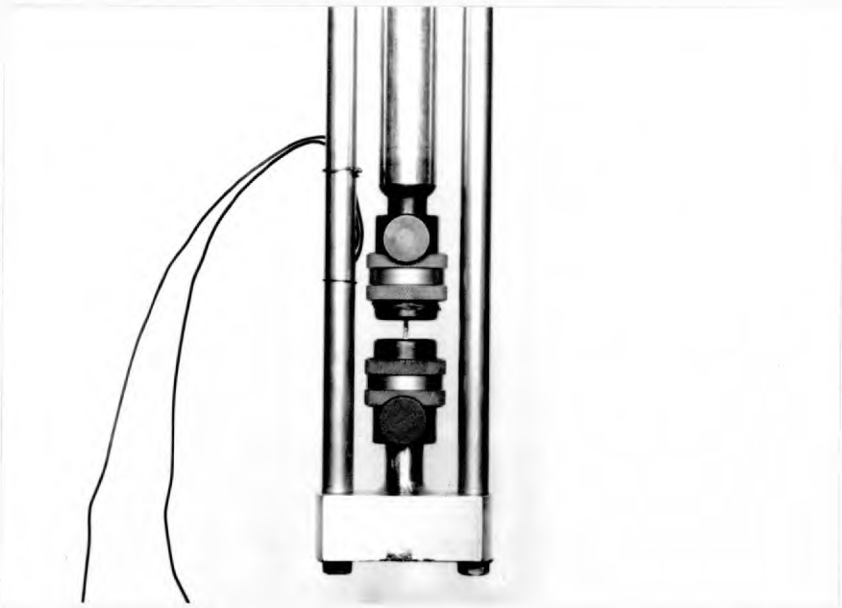


Figure 5.1. Frame for tests in constant temperature bath with the specimen held in special grips.

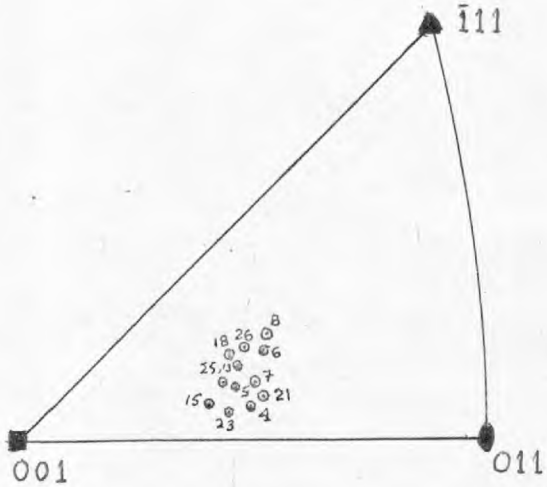


Figure 5.2. Unit stereographic triangle showing the orientation of molybdenum single crystals used for tensile tests.

5.3. Orientation of Specimens

The orientation of the tensile axes of the specimens was near the centre of the unit stereographic triangle. The orientations of the crystals used during the present investigation are shown in Figure 5.2.

5.4. Deformation Behaviour of Specimens

The shear stress versus tensile strain curves of the molybdenum single crystal specimens with the tensile axes near the centre of the stereographic triangle, tested at various temperatures and cross head speeds are plotted in Figures 5.3., 5.4. and 5.5. At 77°K the curves are plotted till fracture, but at other temperatures they are plotted till necking. These curves were obtained from the automatic recording chart in which the load and the elongation were recorded continuously. However, a correction has been applied for the extension of the machine by replacing the specimen with a thick block of steel and doing a test under identical conditions.

The shear stress, τ, was calculated using the following formulae of Schmid and Bois[187]. When the tensile axis does not rotate during the deformation

$$\tau = \frac{P(1 + \varepsilon)}{\alpha_o} \text{ Cos } \phi_o \text{ Cos } \lambda_o \qquad (5.1.)$$

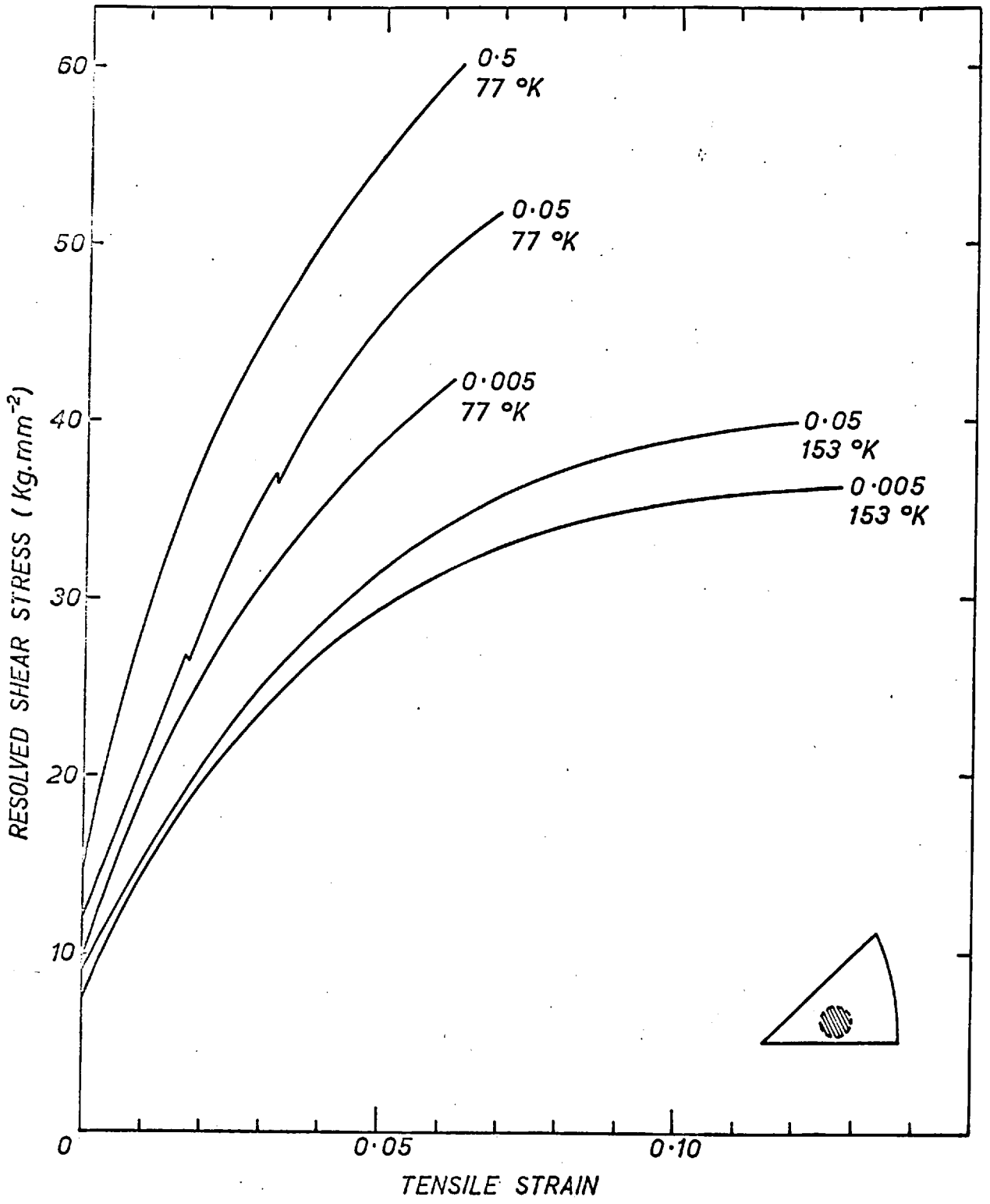


Figure 5.3. Stress-strain curves of crystals with tensile axis in a direction as shown in the stereographic triangle. The numbers 0.5, 0.05 and 0.005 refer to cross head speeds in cm./min.

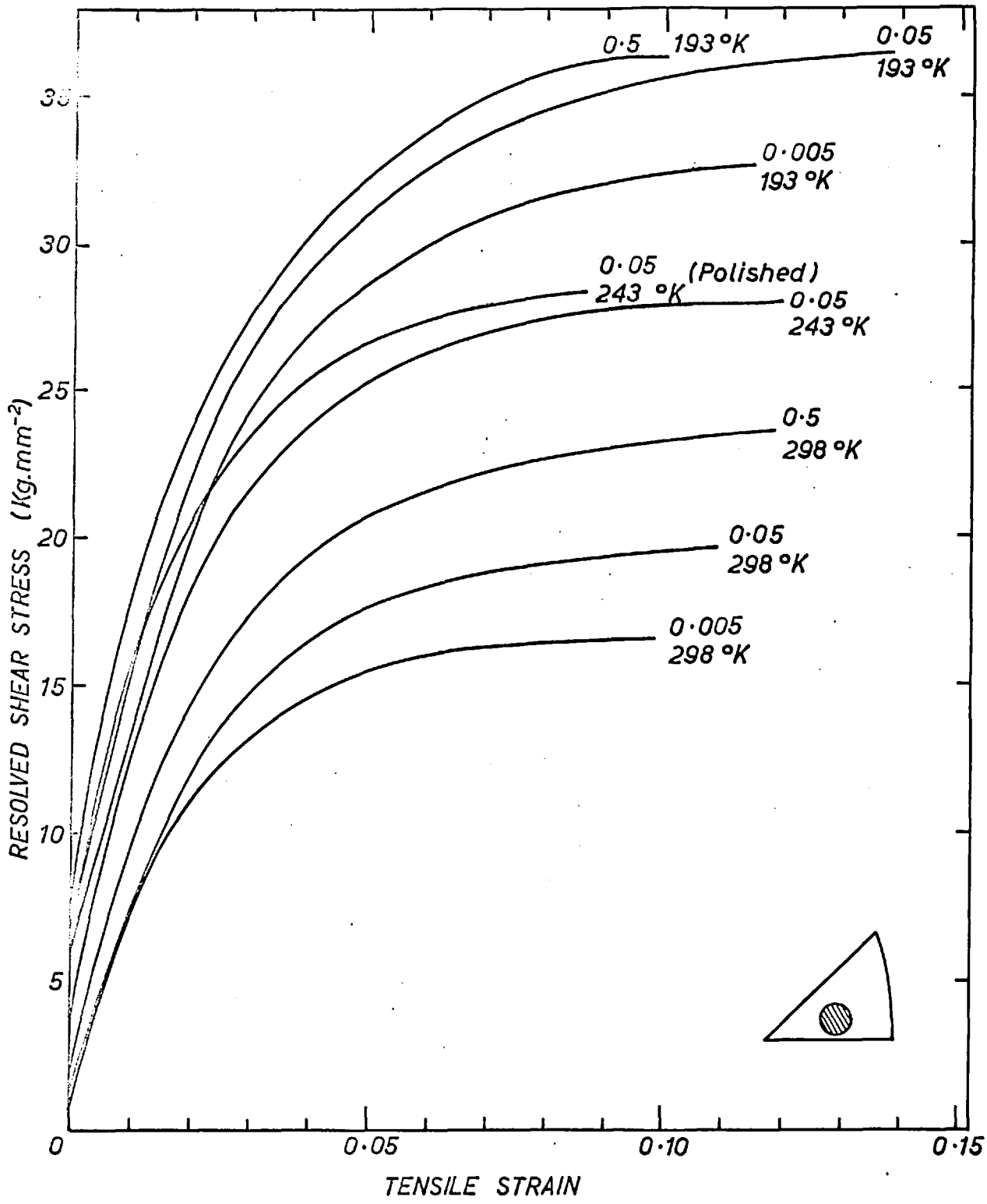


Figure 5.4. Stress-strain curves of crystals with tensile axis in a direction as shown in the stereographic triangle. The numbers 0.5, 0.05 and 0.005 refer to cross head speeds in cm./min.

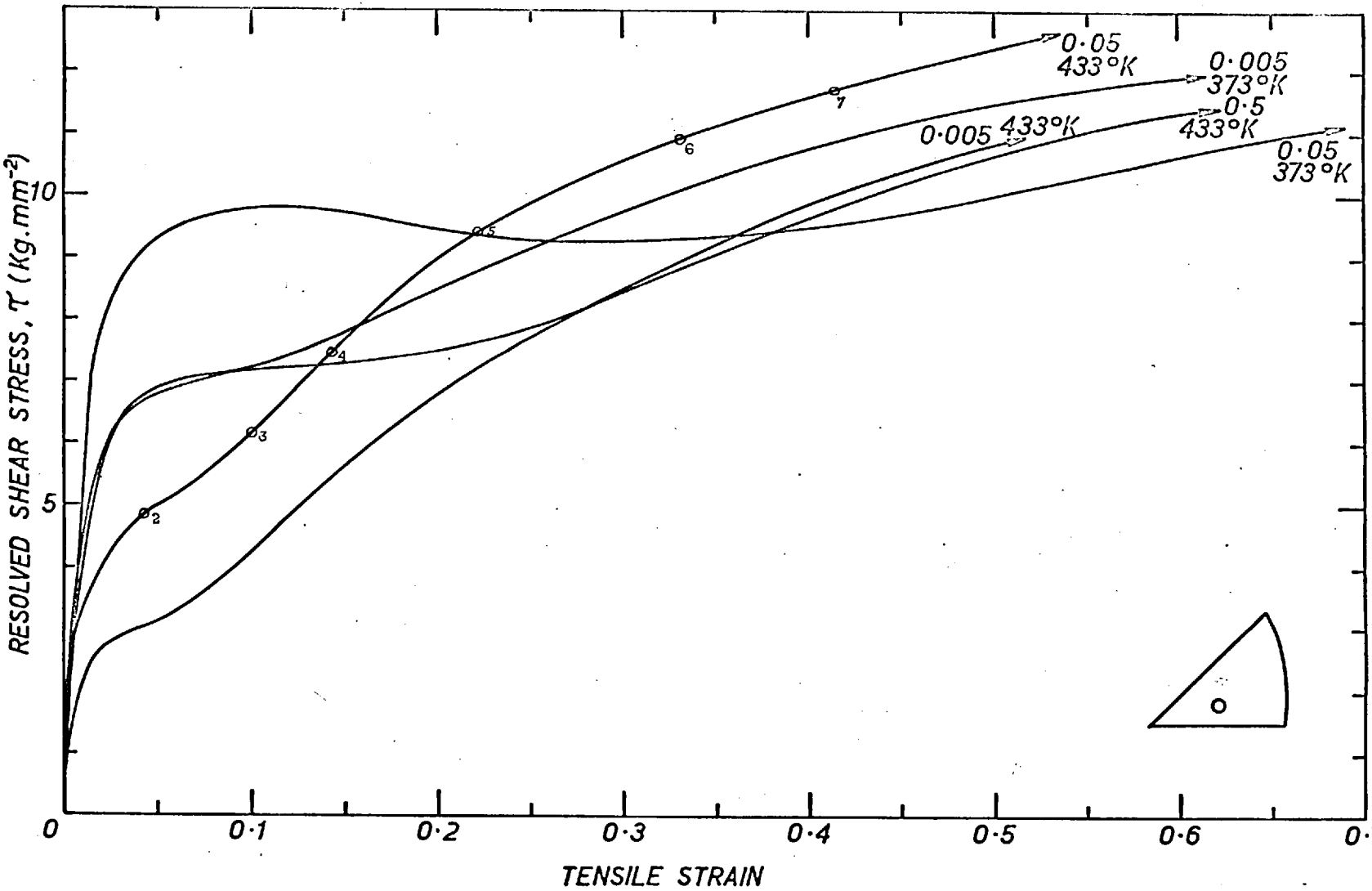


Figure 5.5. Stress-strain curves of crystals with tensile axis in a direction as shown in the stereographic triangle. The numbers 0.5, 0.05 and 0.005 refer to cross head speeds in cm./min.

where P is the load, ε the tensile strain, α_o initial cross sectional area, ϕ_o the angle between the tensile axis and the normal to the slip plane and λ_o the angle between the tensile axis and the slip direction for the undeformed crystal. When the deformation is accompanied by a rotation in the tensile axis,

$$\tau = \frac{P \cos \phi_o}{\alpha_o} \sqrt{1 - \frac{\sin^2 \lambda_o}{(1 + \varepsilon)^2}} \qquad (5.2.)$$

The Schmid factor $\cos \phi_o \cos \lambda_o$ for various possible slip systems with {110} and {112} type slip planes, when the tensile axis is oriented near the centre of the unit triangle are given in Table 5.2.

The proportional limit was taken as the point where the first departure from linearity in the load-elongation curve was observed. The proportional limits of specimens deformed at various temperatures and cross head speeds are listed in Table 5.3. All the stress strain curves have been plotted from the proportional limit.

Considering the nature of the stress strain curves, it is found that the proportional limit and work hardening rate increase with a decrease in temperature and increasing strain rate. There is no yield drop and the initial work hardening rate is much higher than that during the later stages of deformation. There were few load drops due to mechanical

Table 5.2.

Schmid factors for different slip systems with tensile axis oriented near the centre of the unit stereographic triangle.

Slip Direction	Slip Plane	Schmid Factor
111	$(\bar{1}01)$	0.500
	$(0\bar{1}1)$	0.206
	$(\bar{2}11)$	0.455
	$(\bar{1}\bar{1}2)$	0.455
$\bar{1}11$	(101)	0.472
	$(0\bar{1}1)$	0.296
	(211)	0.366
	$(1\bar{1}2)$	0.433
$\bar{1}\bar{1}1$	(011)	0.321
	(101)	0.186
	(112)	0.290
	$(\bar{1}21)$	0.258

Table 5.3.

Proportional limit of single crystals with the tensile axis near the centre of the unit stereographic triangle.

Temperature ^{o}K	Cross Head Speed cm./min	Proportional Limit $Kg./mm.^2$
77	0.005	9.7
	0.05	11.9
	0.5	15.2
153	0.005	7.5
	0.05	9.2
193	0.005	6.17
	0.05	7.14
	0.5	8.41
243	0.005	2.96
	0.05	4.08 (annealed)
	0.05	6.06 (polished)
298	0.005	1.06
	0.05	1.51
	0.5	2.35
373	0.005	1.05
	0.05	1.33
433	0.005	0.76
	0.05	1.0
	0.5	1.23

twinning in specimens deformed at 77°K and at high cross head speeds. In Figure 5.4. the stress-strain curve of a spark machined and electropolished specimen at 243°K has been included. Compared to the stress-strain curve of an annealed specimen deformed at the same temperature and the same cross head speed the unannealed specimen has a higher proportional limit, higher flow stress and a higher work hardening rate.

At 373°K and 433°K the specimens experienced very large elongations and the stress-strain curves show three stages of work hardening very similar to the results obtained in niobium[106], molybdenum[186], iron[188] and tantalum[189] single crystals of similar orientations.

The work hardening coefficients ($\frac{d\tau}{d\varepsilon}$) in stage I and stage II (θ_I and θ_{II}) are given in Table 5.4. The work hardening rate θ_I is negative for the specimen deformed at 373°K at a cross head speed of 0.5 cm./min. Stage 0 was more prominent at 373°K and only for the higher strain rates at 433°K. Stage I became shorter with increase in temperature and decrease in strain rate. Sometimes necking occurred at these high temperatures at more than one place along the gauge length.

5.5. Crystallography of Slip

The average orientation of the specimens was about 6° from the $[100]$-$[110]$ symmetry axis and ≈23° from $[100]$. The

resolved shear stress was highest on $(\bar{1}01)$ $[11\bar{1}]$ slip system and the orientation was ideal for single slip on this system. However, as will be described later, slip occurred in a few other systems with smaller resolved shear stresses.

Attempts were made to determine the slip direction from the migration of the tensile axis during plastic deformation. The Laue photographs of the specimens taken after different amounts of strain at room temperature and below showed no regular movement of the tensile axis. This may be due to more than two slip directions operating in this temperature range. However, during high temperature deformation, characterised by easy glide and three stage hardening, the tensile axis moved steadily towards the $[111]$ direction. The positions of the tensile axis after different amounts of strain are shown in Figure 5.6. and the corresponding points on the stress-strain curve are indicated in Figure 5.5. It is found that stage II starts long before the tensile axis reaches the $[100]$, $[110]$ symmetry line. After the tensile axis reaches the symmetry line, instead of migrating towards $[011]$, due to equal amounts of slip in $[111]$ and $[\bar{1}11]$ directions, it overshoots the symmetry line and continues to move towards the $[111]$ direction.

5.6. Slip Line Observation

Slip planes operating at different temperatures were determined

Table 5.4.

Work hardening coefficients $\frac{d\tau}{d\varepsilon}$ for specimens showing three stages of work hardening.

Temperature ^{o}K	Cross-head Speed cm./min.	Work Hardening Coefficient $Kg/mm.^2$			
		Stage I	θ_I	Stage II	θ_{II}
373	0.005	9.36		13.35	
	0.05	-3.95		6.00	
433	0.005	16.17		26.10	
	0.05	23.72		31.00	
	0.5	2.76		12.36	

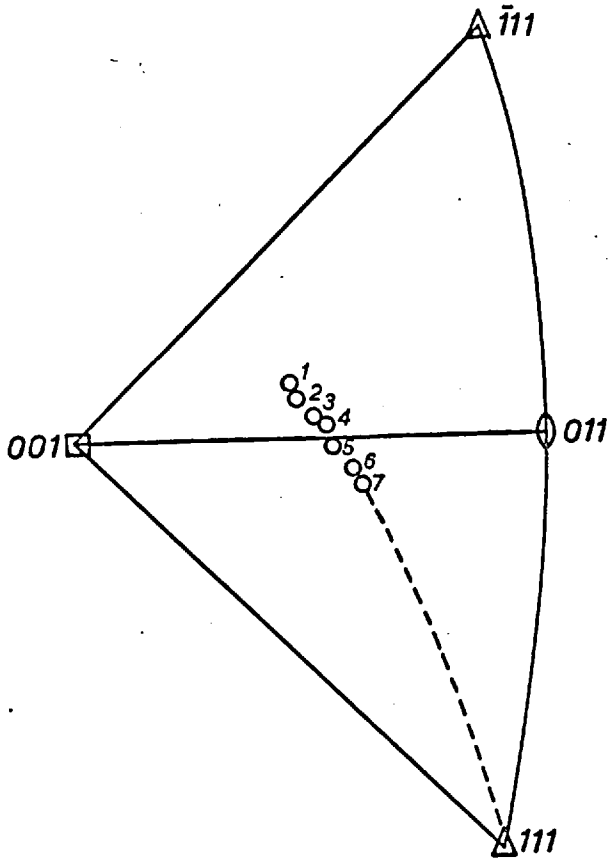


Figure 5.6. Positions of the tensile axis after different amounts of strain at 433°K.

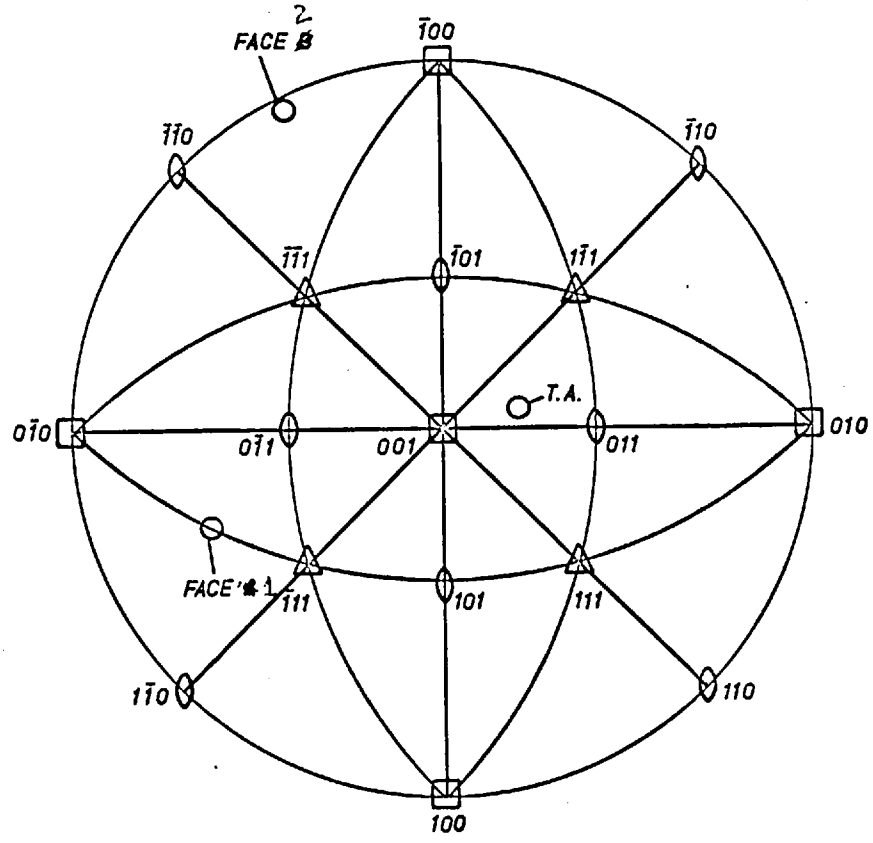


Figure 5.7. Standard (001) stereographic projection showing the orientation of tensile axis and the planes of observation for slip line studies below 273°K.

by slip line observation in deformed specimens. At 243°K and lower temperatures these observations were limited to specimens deformed till the onset of necking, but at room temperature and 433°K slip lines have been studied systematically after various amounts of strain.

The specimen orientation along with the planes of observation for the low temperature investigations are shown in the standard (001) stereographic projection in Figure 5.7. If the slip system $(\bar{1}01)\ [111]$ which has the maximum resolved shear stress were operative, the Burgers vector $[111]$ would be almost parallel to face 1 and perpecdicular to face 2. Thus the dislocations emerging on face 1 would be almost pure edge while those emerging on face 2 would be almost pure screw. Photomicrographs of specimen surfaces showing the slip lines were taken with a Reichert Projection microscope. A Laue back reflection X-ray photograph was then taken to determine the orientation of the slip traces.

The slip lines in a specimen deformed at 77°K are shown in Figure 5.8. The slip lines are reasonably straight on both surfaces, probably due to the difficulty of cross slip at this low temperature. On face 1, the slip traces indicate that two slip systems $(\bar{1}01)\ [111]$ with a Schmid factor of ≈0.5 and $(101)\ [\bar{1}11]$ with a Schmid factor of ≈0.47 may be operating. Slip lines in the former system are more numerous and continuous than in the latter system. On face 2 a set of straight slip lines



(a) x 200



(b) x 200

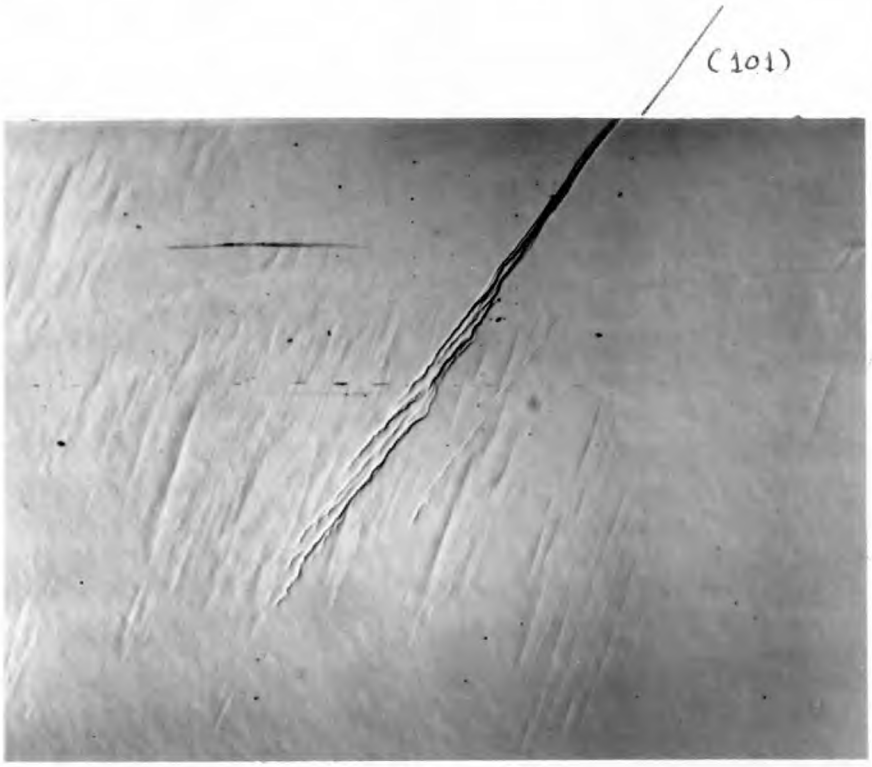
Figure 5.8. Slip lines on a specimen deformed at 77°K.

(a) face 1. (b) face 2.

belonging to $(\bar{1}01)$ $[111]$ system were identified, but it was very difficult to identify the other set of slip lines.

The nature of slip lines is somewhat different at 153°K (Figure 5.9.). On face 1 there are some very fine slip lines belonging to either the $(\bar{1}01)$ $[111]$ or $(0\bar{1}1)$ $[\bar{1}11]$ system. It is very difficult to choose between them as both of them make almost the same trace on that surface. However, the former with a larger Schmid factor is more likely to operate. In addition to this there are some discontinuous and broad slip lines coinciding with the trace of the $(0\bar{1}\bar{1})$ plane. One very interesting observation made is that there are few very deep slip lines on this surface. They start at the edge of the specimen, extend on to the surface and branch out looking very much like a broom stick. These slip lines are also continuous on face 2 where they produce long deep slip lines with very fine parallel slip lines in between. The corresponding slip system has been identified as (101) $[\bar{1}11]$. Besides this, there are short and wide slip bands on face 2 belonging to the $(0\bar{1}\bar{1})$ $[\bar{1}\bar{1}1]$ system.

At 193°K the slip lines are very similar to those at 153°K (Figure 5.10.). Only the branched slip bands are more prominent and they contain small segments representing cross slip within these bands. On face 2 the corresponding slip lines are very deep and straight with faint parallel slip

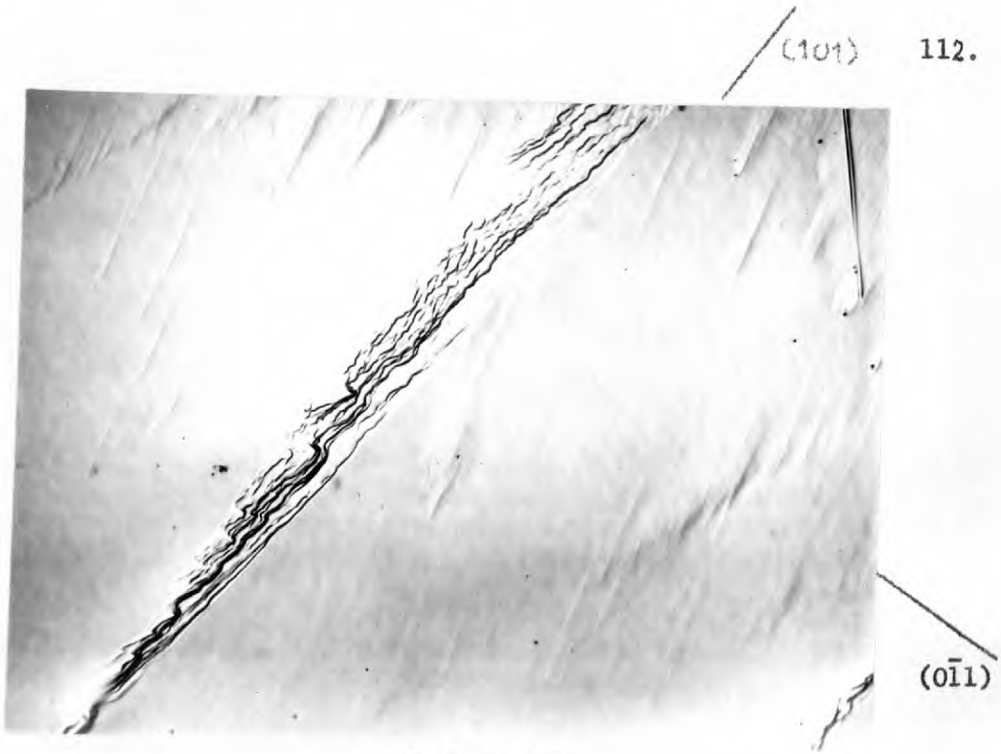


(a) x 200

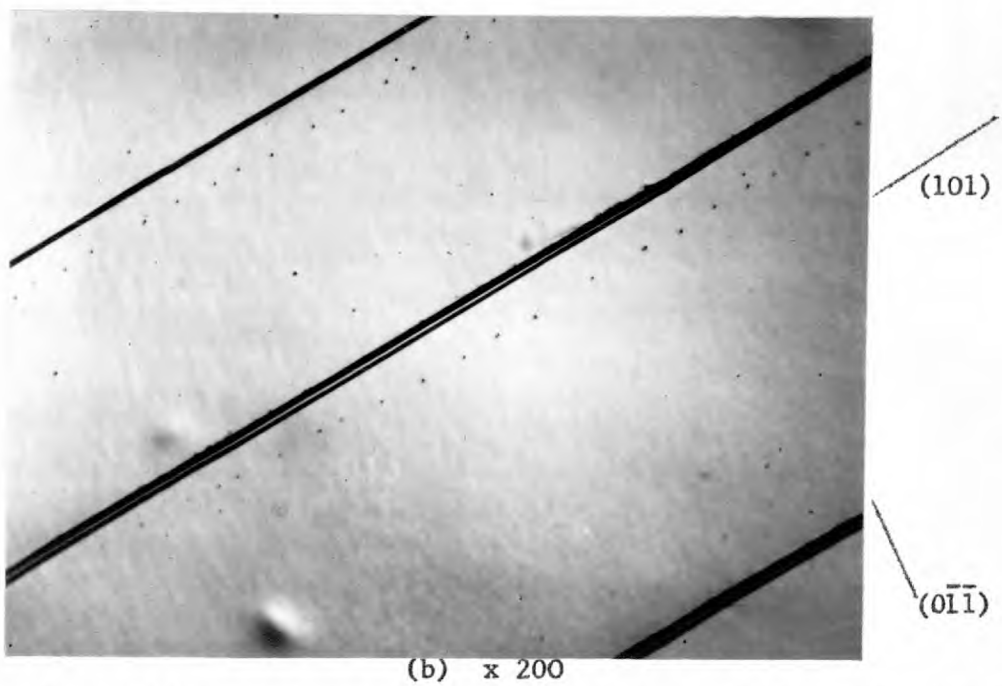


(b) x 200

Figure 5..9. Slip lines on a specimen after 12% tensile strain at 153°K. (a) face 1. (b) face 2.



(a) x 200



(b) x 200

Figure 5.10. Slip lines on a specimen after 13% tensile strain at 193°K. (a) face 1. (b) face 2.

lines in between. There are rows of small pits almost parallel to the deep slip lines.

At 243°K (Figure 5.11.) there are no branching slip bands on face 1, though a few deep and straight slip lines belonging to $(0\bar{1}1)\ [\bar{1}11]$ are observed on face 2. On face 1, there are some slip lines which may be due to slip on either $(0\bar{1}1)$ plane or the $(\bar{1}01)$ plane. Besides, traces of slip on the (101) plane can also be observed on this face.

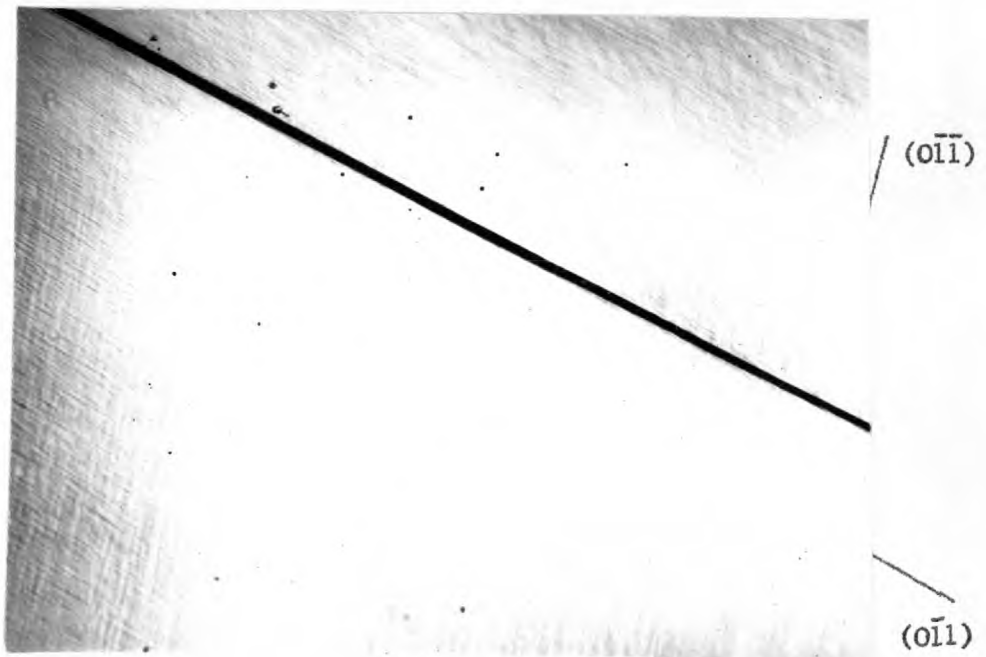
At room temperature and 433°K a set of different planes have been chosen for slip line observation and the orientation of the specimen axis along with the poles of the specimen surfaces are shown in a standard (001) projection in Figure 5.12.

At room temperature slip line observations have been made after 4%, 10%, and 12.5% tensile strain and the corresponding photomicrographs indicating the slip systems are shown in Figures 5.13., 5.14.and 5.15. On face A there are two sets of intersecting straight slip lines representing slip on the $(\bar{1}01)\ [111]$ and $(101)\ [\bar{1}11]$ slip systems. With increasing strain the slip lines belonging to the $(\bar{1}01)\ [111]$ system become more distinct and continuous. On face B the slip lines are wavy and there are signs of extensive cross slip. At all strains slip on the $(\bar{2}\bar{1}1)$and (101) planes is observed and there is indication of slip in the $(0\bar{1}\bar{1})$ plane after 12.5% tensile strain.

At higher temperatures, the slip lines in the deformed



(a) x 200



(b) x 200

Figure 5.11. Slip lines on a specimen after 12% tensile strain at 243°K. (a) face 1. (b) face 2.

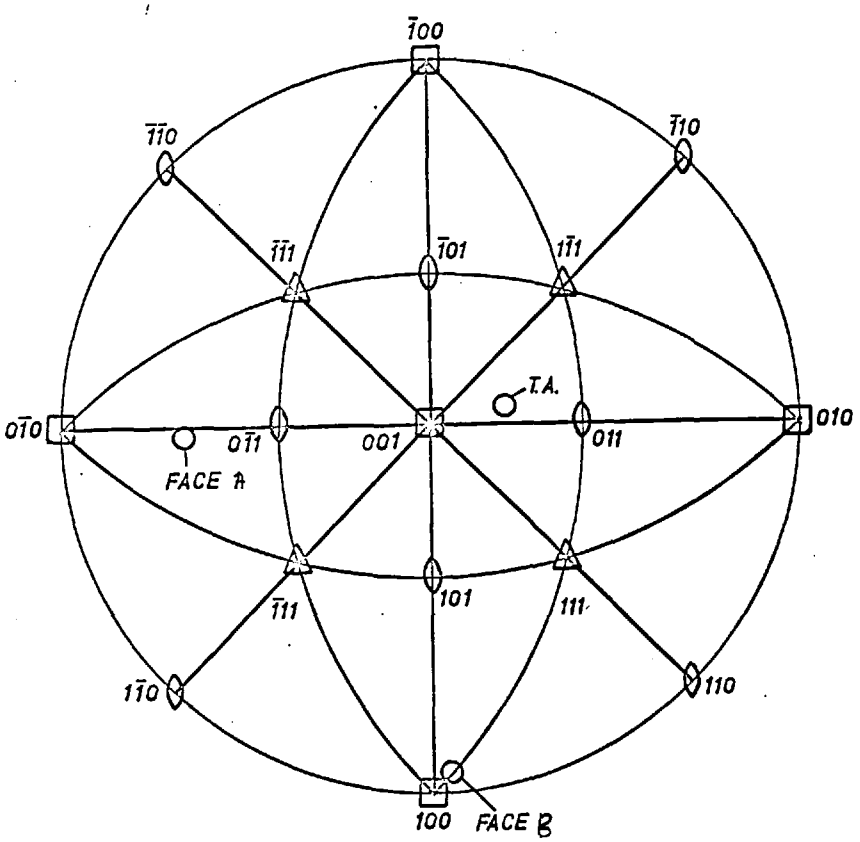


Figure 5.12. Standard (001) stereographic projection showing the orientation of the tensile axis and the planes for slip line observation at 298°K and 433°K.

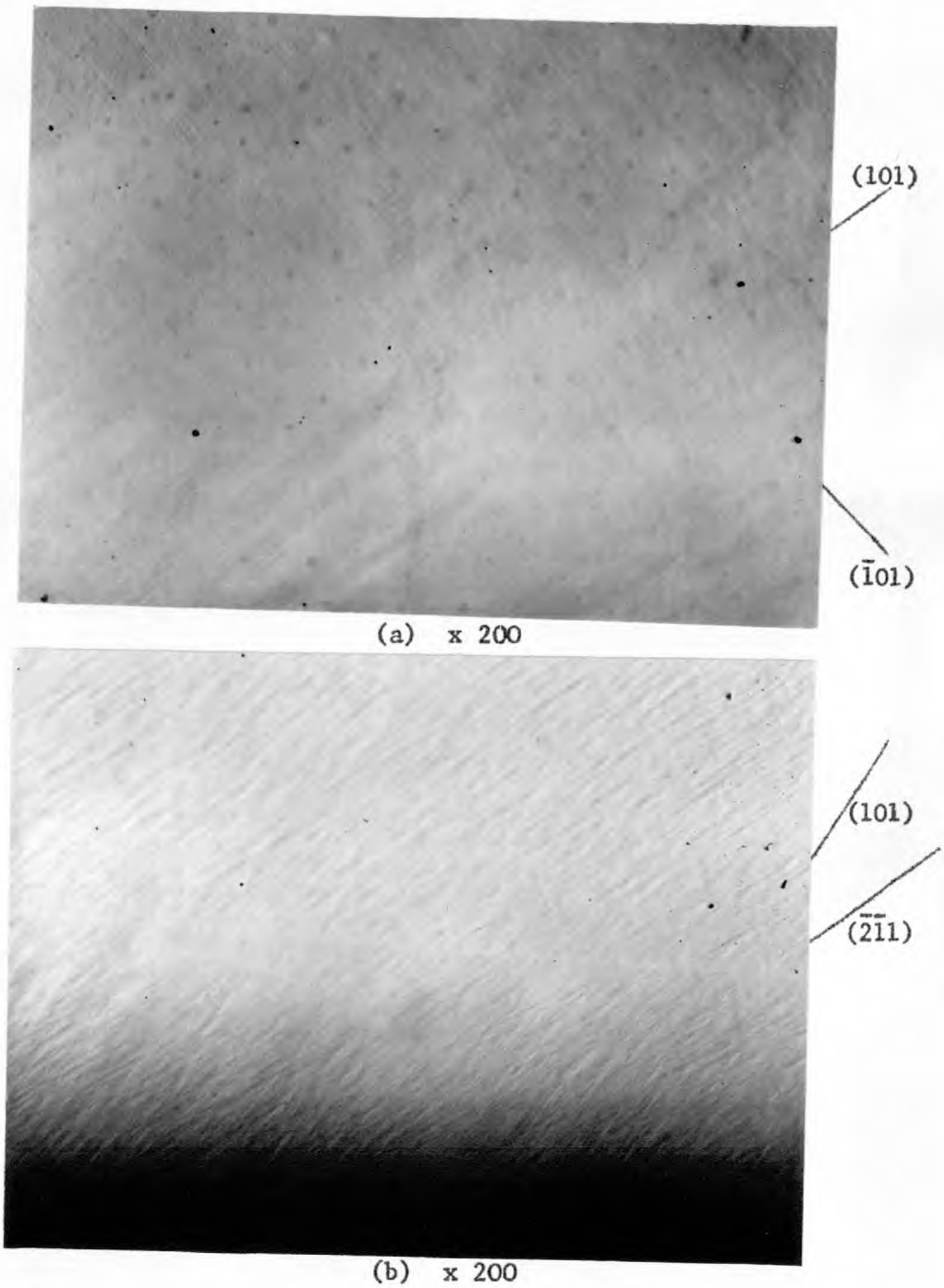
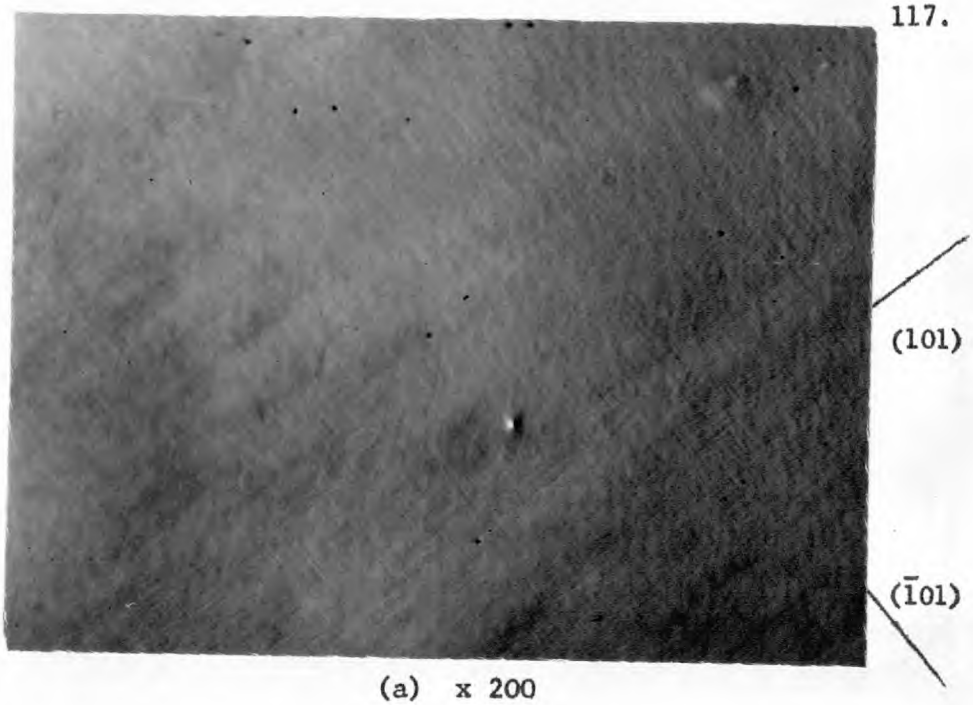


Figure 5.13. Slip lines on a specimen after 4% tensile strain at 298°K. (a) face A. (b) face B.



(a) x 200

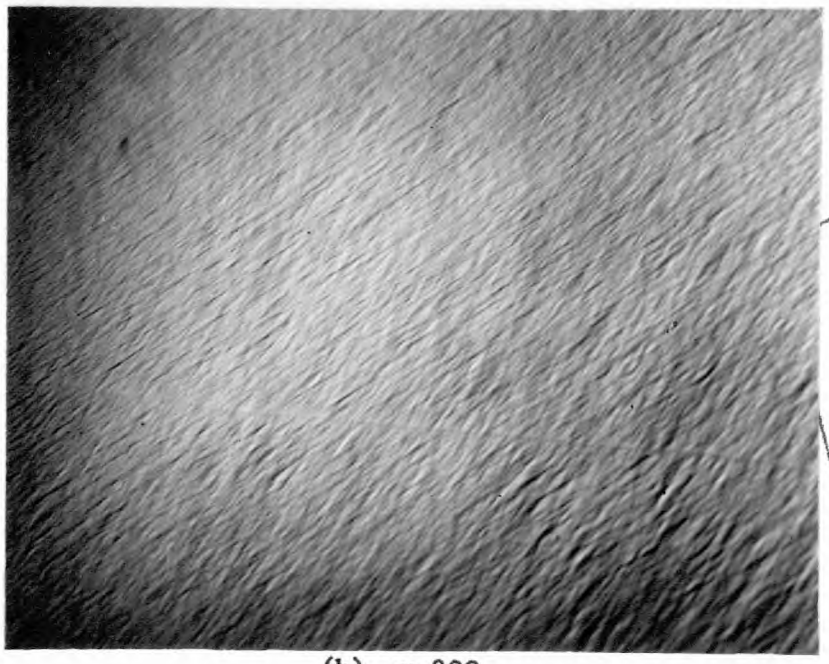


(b) x 200

Figure 5.14. Slip lines on a specimen after 9% tensile strain at 298°K. (a) face A. (b) face B.



(a) x 200

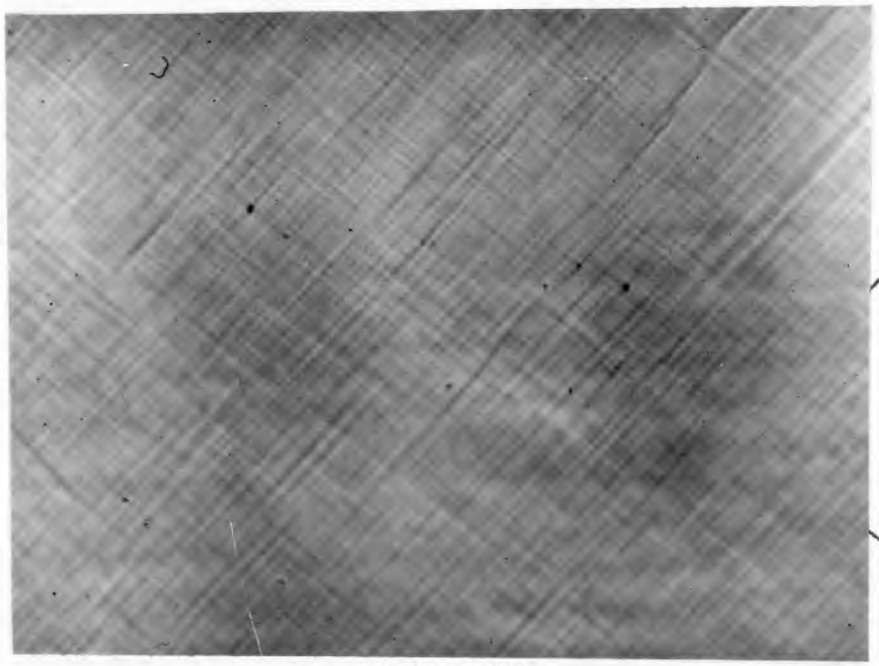


(b) x 200

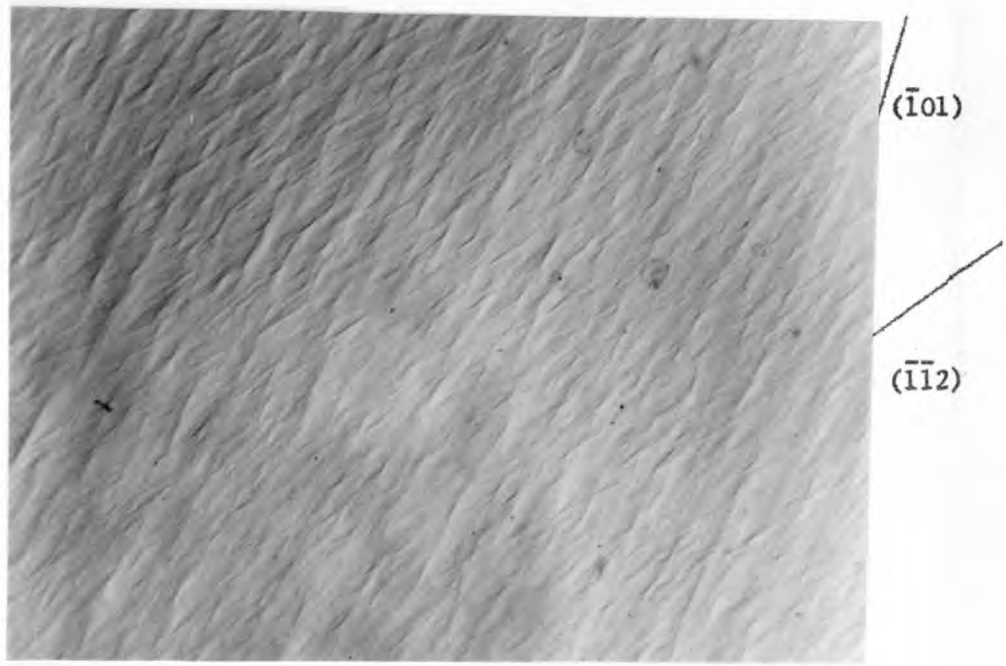
Figure 5.15. Slip lines on a specimen after 12.5% tensile strain at 298°K. (a) face A. (b) face B.

specimens are much more well developed. This is illustrated in Figures 5.16. to 5.19. for a specimen strained at 433°K. After 4% tensile strain slip lines are long and straight on face A (Figure 5.16a.). They coincide with traces of the $(\bar{1}01)$ and (101) planes on which the resolved shear stresses are higher than on any other planes. On face B (Figure 5.16b), the slip lines are wavy and discontinuous and they indicate slip on $(\bar{1}01)$ and $(\bar{1}\bar{1}2)$ planes both of which belong to the $[111]$ zone. Slip in the (101) $[\bar{1}11]$ slip system is evident from the observation of slip lines on face A, but its contribution can not be appreciable because the specimen axis steadily moves towards $[111]$ during deformation. After 10% tensile strain (Figure 5.17.) there is not much change except that slip lines are more distinct and sharp.

After 14% deformation (Figure 5.18.) $(\bar{1}\bar{1}2)$ slip traces on face B have become very faint, and there is a tendency for glide band formation due to slip on the $(2\bar{1}\bar{1})$ $[111]$ system. After 33% deformation (Figure 5.19.) traces of slip on the (101) plane observed on face A are faint, but $(\bar{1}01)$ traces look more prominent. On face B deformation bands have developed more fully and $(\bar{1}01)$ slip lines are fragmented.

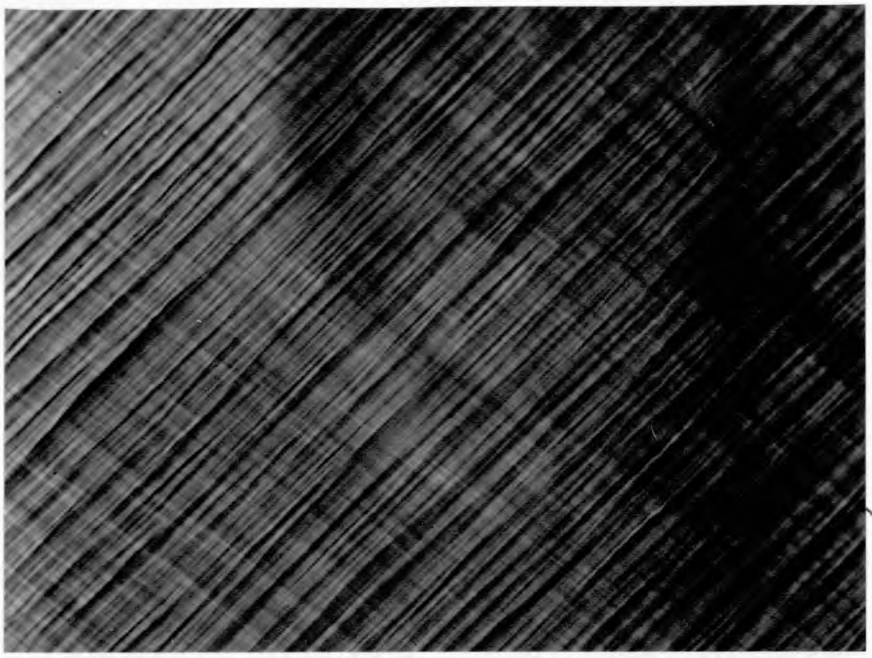


(a) x 200

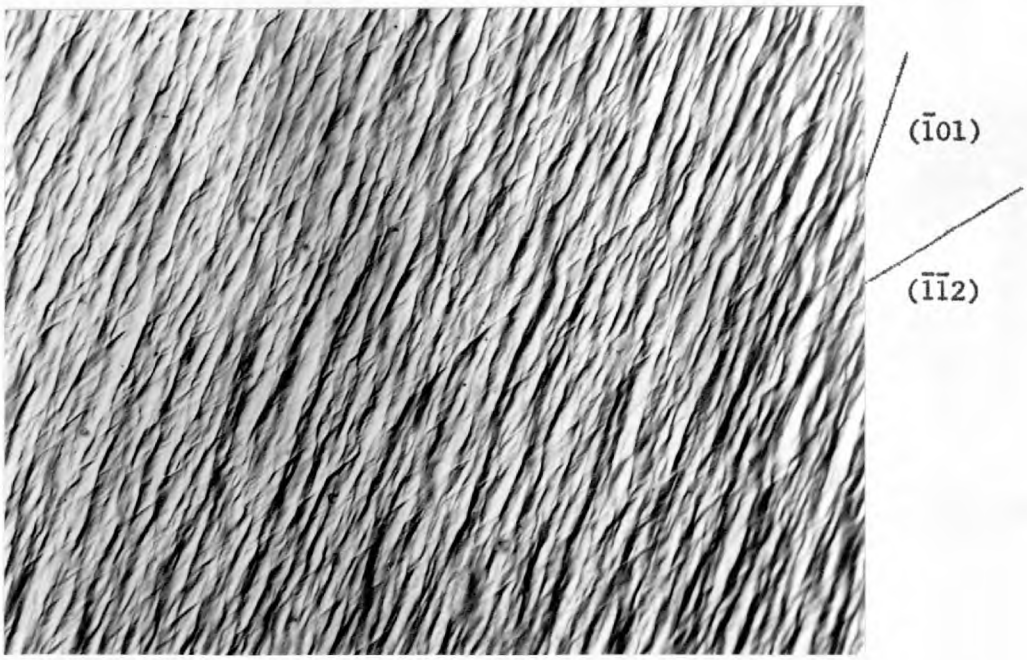


(b) x 200

Figure 5.16. Slip lines on a specimen after 4% tensile strain at 433°K. (a) face A. (b) face B.



(a) x 200



(b) x 200

Figure 5.17. Slip lines on a specimen after 10% tensile strain at 433°K. (a) face A. (b) face B.



(a) x 200

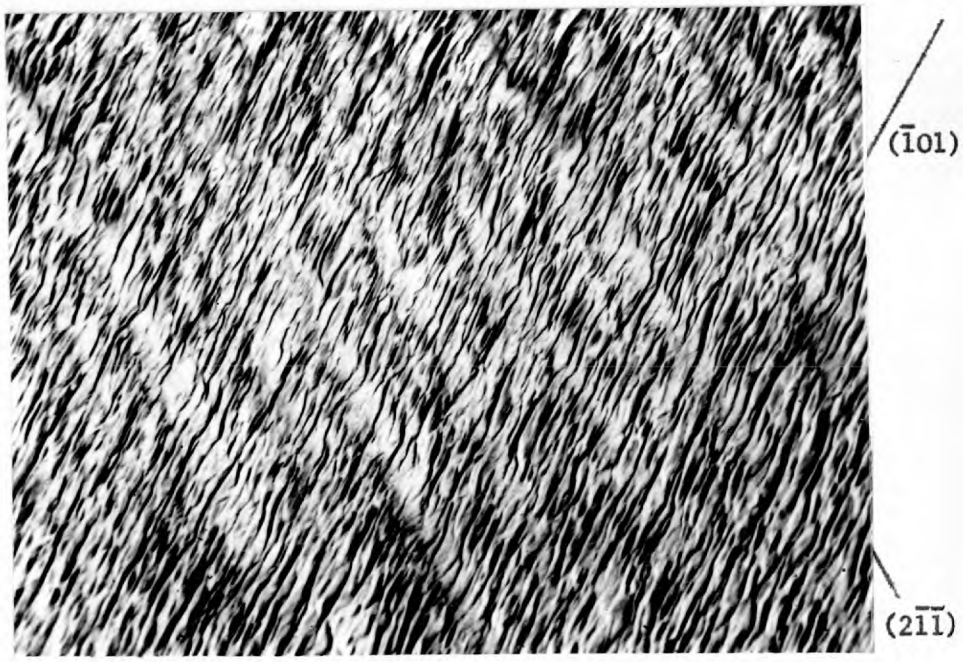


(b) x 200

Figure 5.18. Slip lines on a specimen after 14% tensile strain at 433°K. (a) face A. (b) face B.



(a) x 200



(b) x 200

Figure 5.19. Slip lines on a specimen after 33% tensile strain at 433°K. (a) face A. (b) face B.

5.7. Variation of Dislocation Density with Stress and Strain

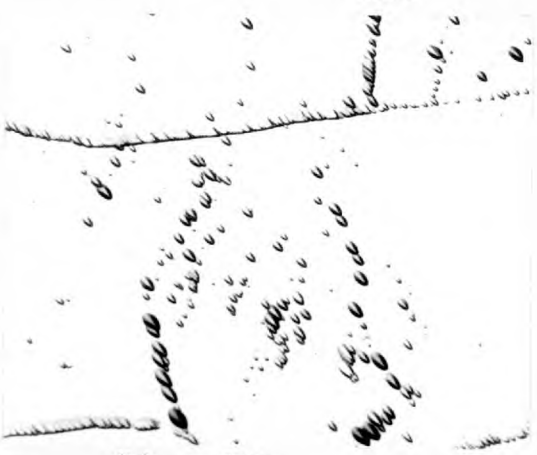
The variation of dislocation density with stress and strain was studied at 298°K and 193°K using the etch pit method. The tensile specimen was stressed to a certain stress, unloaded, polished and etched to determine the density of the dislocation etch pits. Then it was stressed to a higher load and the process was repeated till the etch pit density was too high to resolve the individual pits by optical microscopy. Figure 5.20. shows the distribution and density of etch pits in a specimen stressed to different stresses at room temperature. To eliminate any error from the non-uniform distribution of dislocations in the specimen the same region of the specimen was chosen for observation every time. The variation of dislocation density with strain is shown in Figure 5.21. At room temperature the dislocation etch pit density varies almost linearly with strain. It is unfortunate that dislocation density can be determined only at very low strains and stresses by the etch pit method. At 193°K only a few experimental points have been obtained.

The experimental data on the etch pit density ρ can be fitted into the relation

$$\rho = \rho_o + C' \varepsilon^{\alpha} \qquad (5.3.)$$



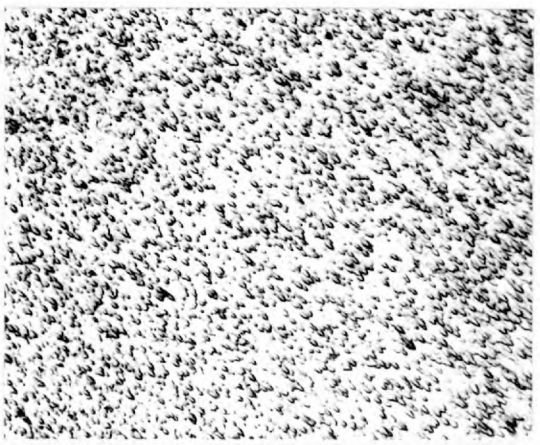
(a) x 200



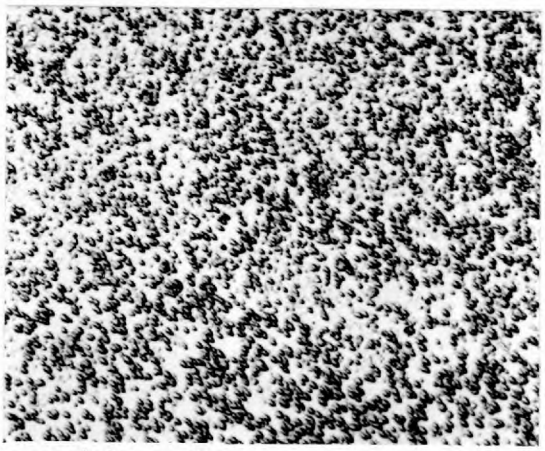
(b) x 200



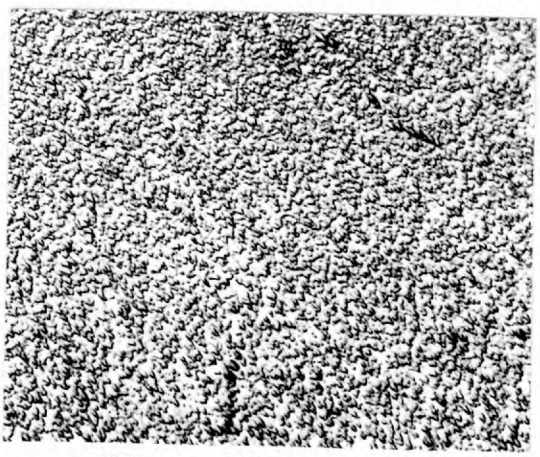
(c) x 200



(d) x 200



(e) x 200



(f) x 200

Figure 5.20. Dislocation etch pits on a plane near (112) after various amounts of strain (and stress).
(a) unstressed. (b) τ=0.99 kg/mm.^{2}. (c) ε=0.0013, τ=1.94 kg/mm.^{2}. (d) ε=0.0038, τ=3.72 kg.mm.^{2}
(e) ε=0.0052, τ=4.87 kg/mm.^{2}. (f) ε=0.0084, τ=6.43 kg/mm.^{2}.

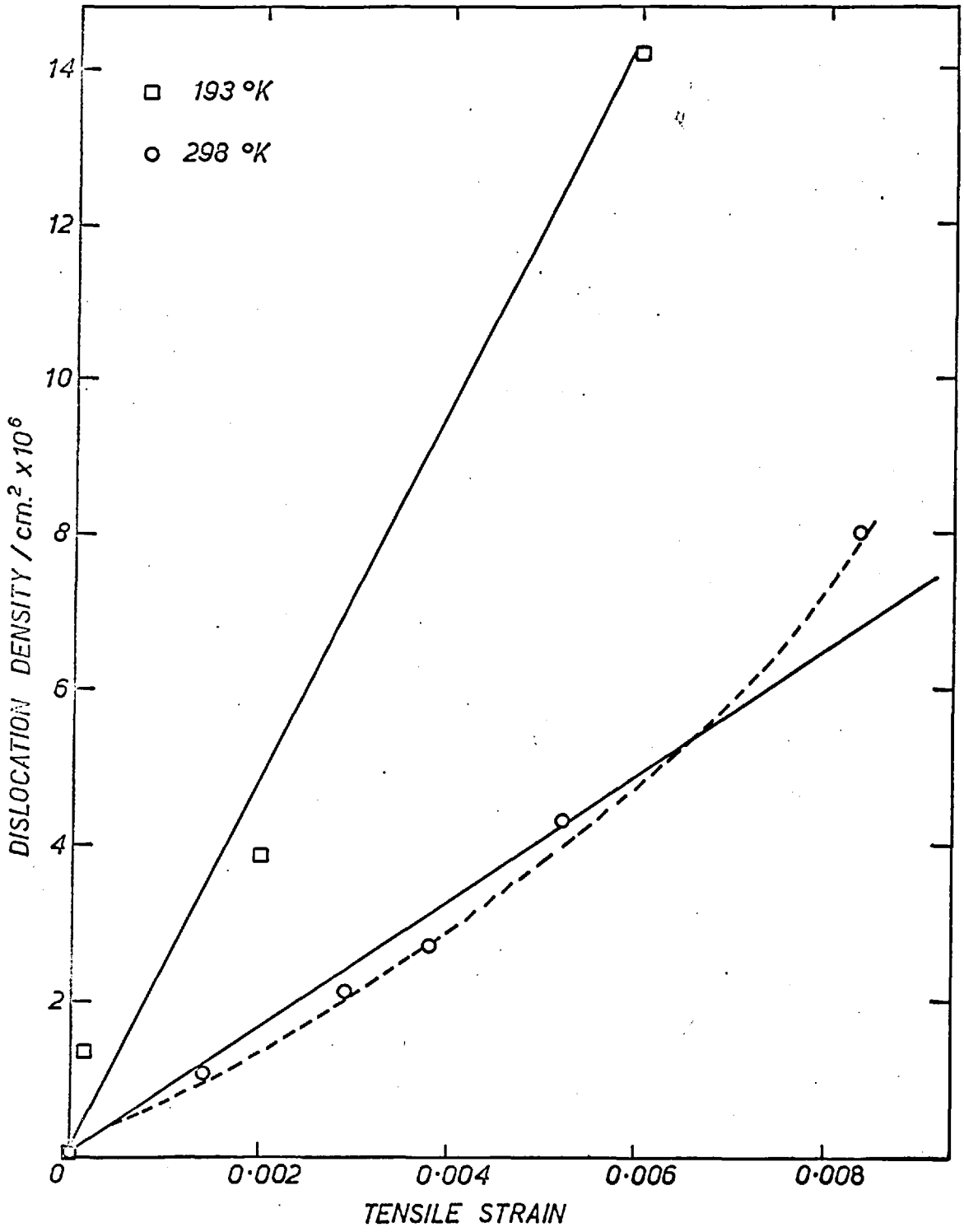


Figure 5.21. Variation of dislocation density with tensile strain.

where ρ_o is the grown-in dislocation density and C' and α are constants. In agreement with Lawley and Gaigher's[64] work on the dislocation density determined by electron microscopy, the change in dislocation density with strain($\frac{d\rho}{d\varepsilon}$) increases with decreasing temperature. However, when a linear relationship between ρ and ε is assumed (i.e. $\alpha = 1$), $\frac{d\rho}{dt} \simeq 8.2 \times 10^6/cm.^2/1\%$ strain at room temperature and the corresponding value at 193°K is $1.7 \times 10^7/cm.^2/1\%$ strain. This is about 2 orders of magnitude less than the values obtained by Lawley and Gaigher[64] in zone melted molybdenum single crystals and by Gilbert et al.[190] in polycrystalline molybdenum. This may be explained by the fact that in the present investigation the specimens have a much lower initial dislocation density ρ_o ($\simeq 6 \times 10^4/cm.^2$) in contrast to the initial dislocation density of $\simeq 5 \times 10^8/cm.^2$ in specimens used by the above mentioned workers. This low dislocation density can have a very significant effect during the early stages of deformation. The dislocations can move over very long distances without encountering any other dislocations and thus a much larger strain can be achieved with a small number of dislocations. This is supported by the very low friction stress in these low dislocation density specimens. However, the situation will change with increased strain which is accompanied by an increase in the dislocation density. Under these conditions the dislocations can travel only short distances

before encountering other dislocations. This may lead to cross slip and a faster rate of dislocation multiplication to keep up the imposed strain rate and to produce the necessary strain. Then the situation may probably be the same as in the experiments of Lawley et al. and Gilbert et al. Unfortunately this cannot be verified by the etch pit method. However, there is some evidence to support this view in the present experimental data. At higher strains the etch pit density increases much more rapidly with strain and the dotted curve in Figure 5.21. ($\alpha > 1$) fits the experimental data better than the solid straight line at room temperature.

Figure 5.22. shows the variation of dislocation density ρ with resolved shear stress τ. τ varies as the square root of the dislocation density and the relation

$$\tau = \tau_o + k\sqrt{\rho} \qquad (5.4.)$$

is satisfied. τ_o is the composite frictional stress and has a value of $\simeq$0.5 kg/mm.^{2} at room temperature and $\simeq$1.6 kg/mm.^{2} at 193°K which seems unusually low compared to 7.3 kg/mm.^{2} and 8.2 kg/mm.^{2} as determined by Lawley et al[64] at similar temperatures. Again this may be due to the low initial dislocation density in the present case. It is also noted that there is a large increase in dislocation density at the proportional limit as shown by the dotted line joining the

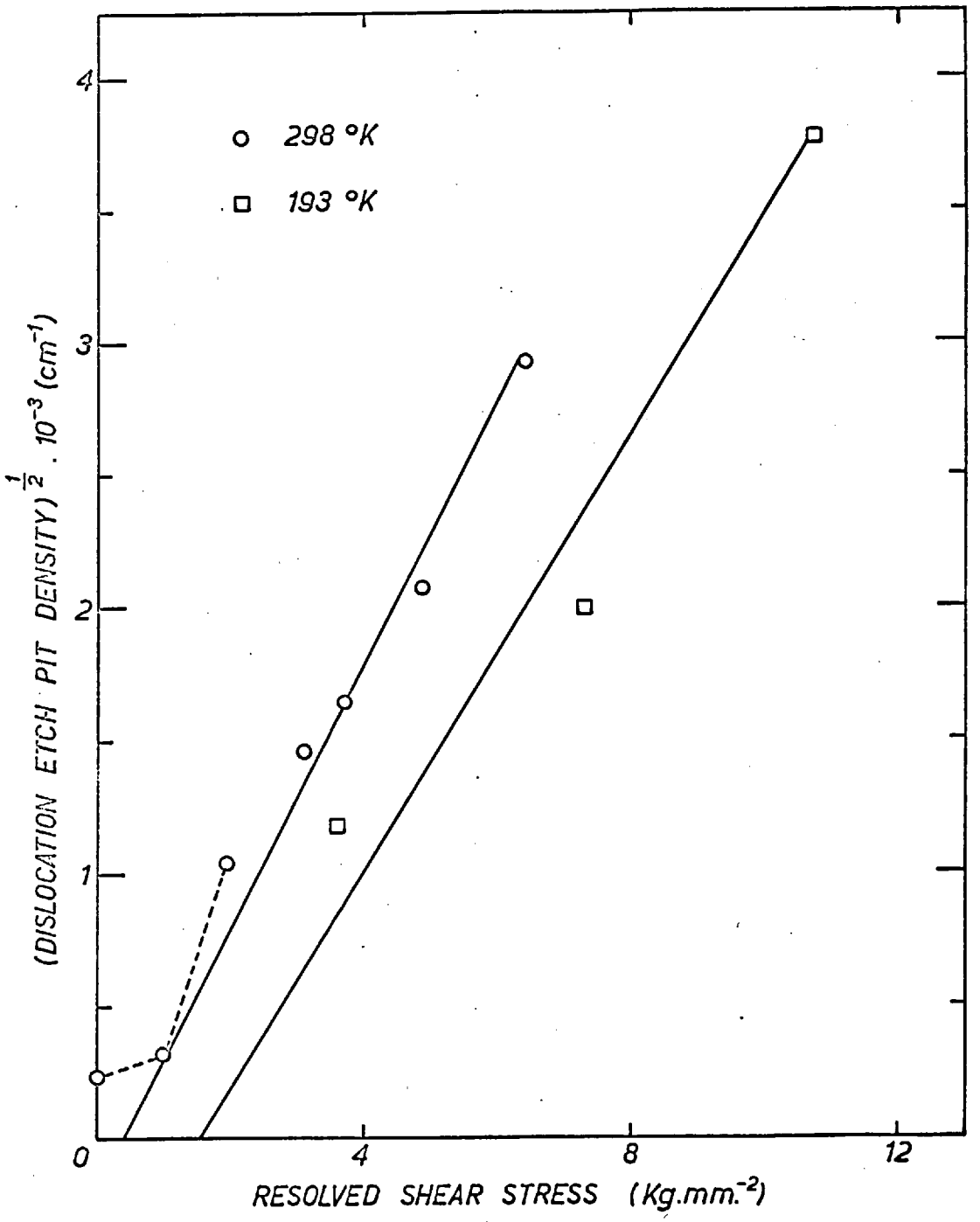


Figure 5.22. Dependence of flow stress on dislocation density.

first three points at room temperature (Figure 5.22).

5.8. Strain Rate Sensitivity of Flow Stress

Strain rate change experiments were performed by changing the cross head speed of the Instron machine between 0.005 cm./min. and 0.05 cm./min. This produced an effective change in tensile strain rate between approximately 6×10^{-5} and 6×10^{-4} sec.$^{-1}$. Strain rate change tests were done at 77^{o}, 153^{o}, 193^{o}, 243^{o}, 273^{o}, 298^{o}, 373^{o} and 433^{o}K and the corresponding stress strain plots at some of these temperatures are shown in Figure 5.23. All measurements have been made during the transition involving an increase in stress. No yield point was observed on increasing the strain rate and the stress increment $\Delta\tau$ has been determined by an extrapolation method as shown in Figure 5.23.

The strain rate sensitivity λ $(= \frac{d\tau}{d \log \dot{\gamma}})$, where $\dot{\gamma}$ is the shear strain rate, is plotted against the resolved shear stress τ at different temperatures in Figures 5.24. and 5.25. It is found that λ decreases slightly with stress at 77^{o}K, and remains almost constant with stress at 153^{o}K. At 193^{o}K and 243^{o}K λ increases with τ at lower values of τ, but then levels off during the later stages of deformation. At 273^{o}K and 298^{o}K λ increases steadily with increasing stress; but at 373^{o}K and 433^{o}K λ increases with τ, reaches a maximum at $\simeq$7.5 to 8.5

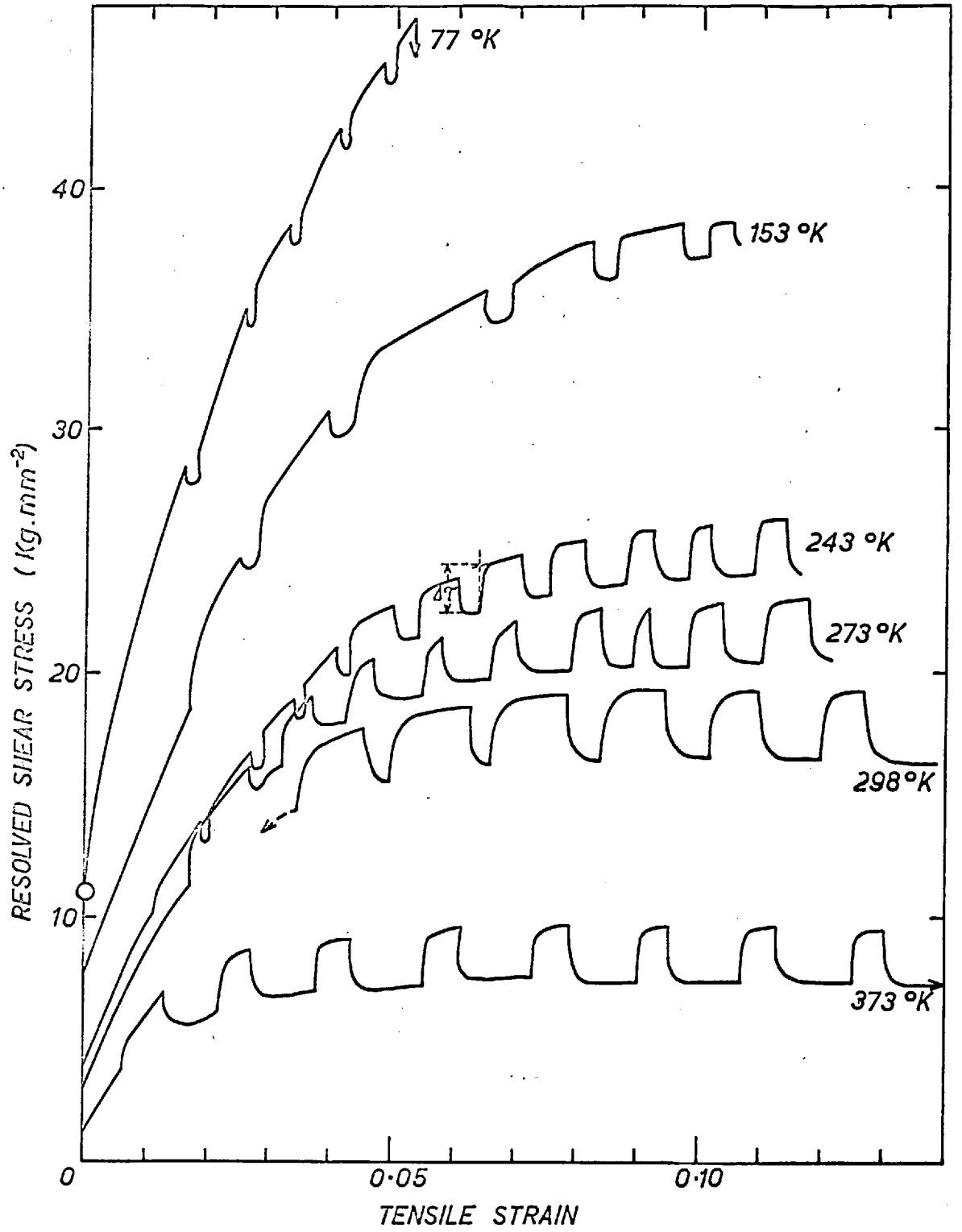


Figure 5.23. Stress-strain curves for strain rate change experiments at various temperatures.

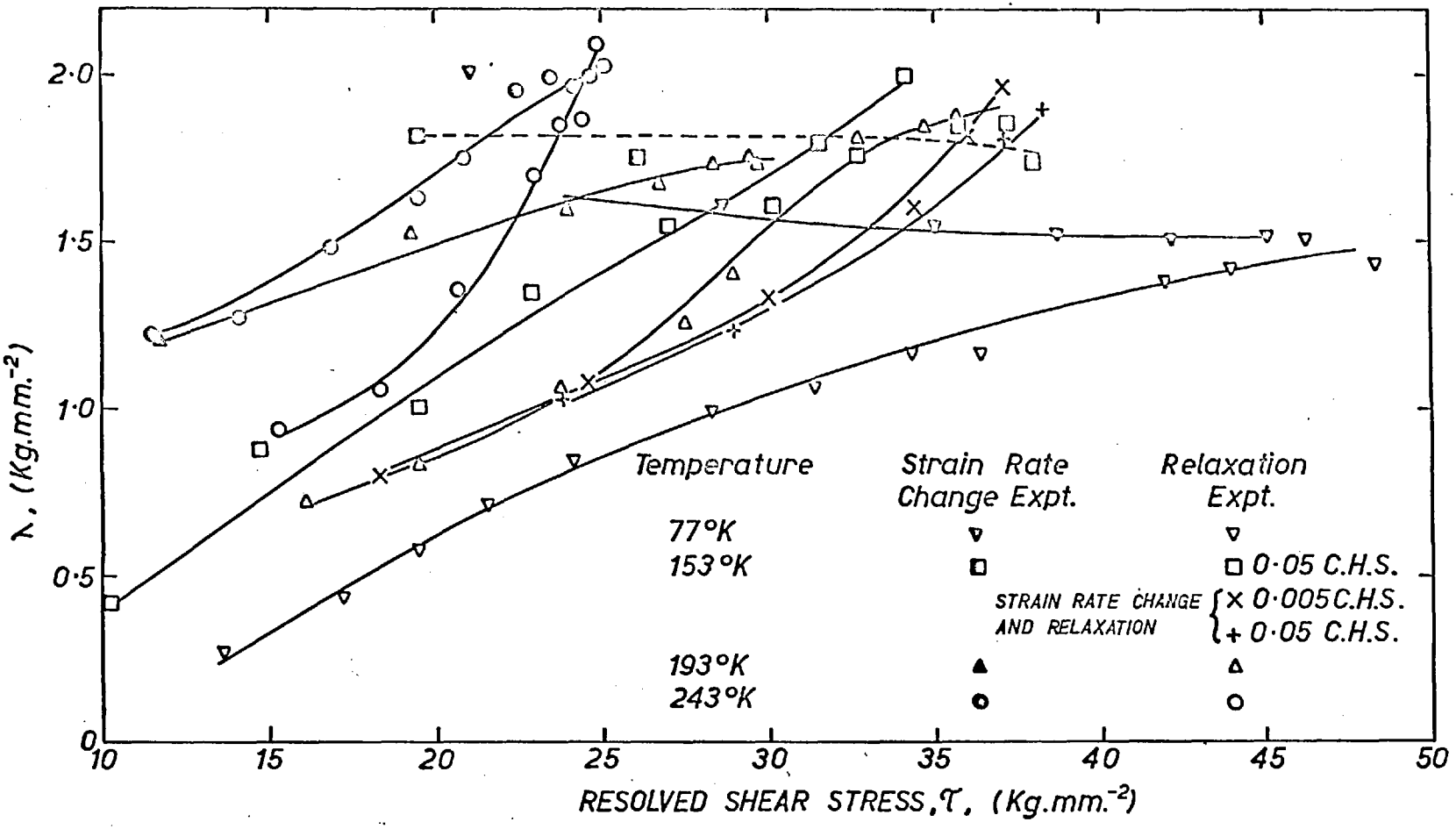


Figure 5.24. Variation of the strain rate sensitivity with applied stress at 77°K, 153°K, 193°K and 243°K.

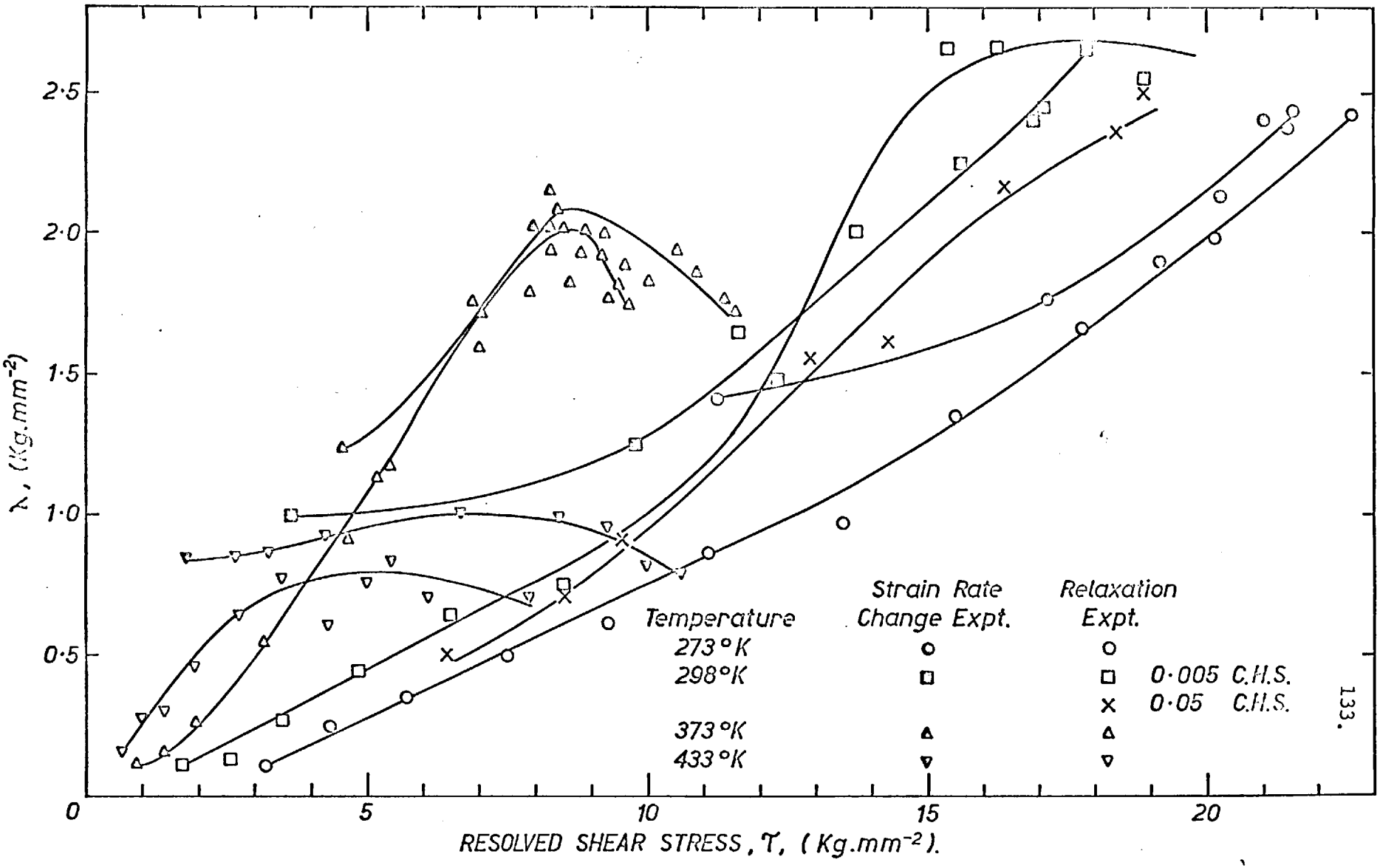


Figure 5.25. Variation of the strain rate sensitivity with applied stress at 273°K, 298°K, 373°K and 433°K.

$kg/mm.^2$, and decreases again. Considering the variation of λ with temperature, it is found that λ increases as the temperature is decreased, reaches a maximum in the range 298^oK to 273^oK and then decreases slightly at lower temperatures.

5.9. Temperature Sensitivity of Flow Stress

The effect of temperature on the flow stress was investigated by differential temperature cycling tests. In order to facilitate the calculation of activation energy, the constant temperatures (T's) of strain rate cycling and relaxation tests were used as the mean temperatures for the temperature change experiments. The temperature was cycled between T + 15^oK and T - 15^oK above 243^oK and between T + 10^oK and T - 10^oK below 243^oK. The specimen was partially unloaded during a change in temperature. This did not introduce any unloading yield drop at higher temperatures, but a small rounded yield drop was sometimes noticed at lower temperatures. When a yield drop was present the stress increment was calculated by taking the difference between the upper yield point and the stress immediately before the temperature change. In other cases an extrapolation method as shown in Figure 5.26. was used. Stress strain curves for temperature change tests are shown in Figures 5.26 and 5.27. Temperature sensitivities of the flow stress $(\frac{\Delta\tau}{\Delta T})_{\dot{\gamma}}$ at different mean temperatures have been plotted

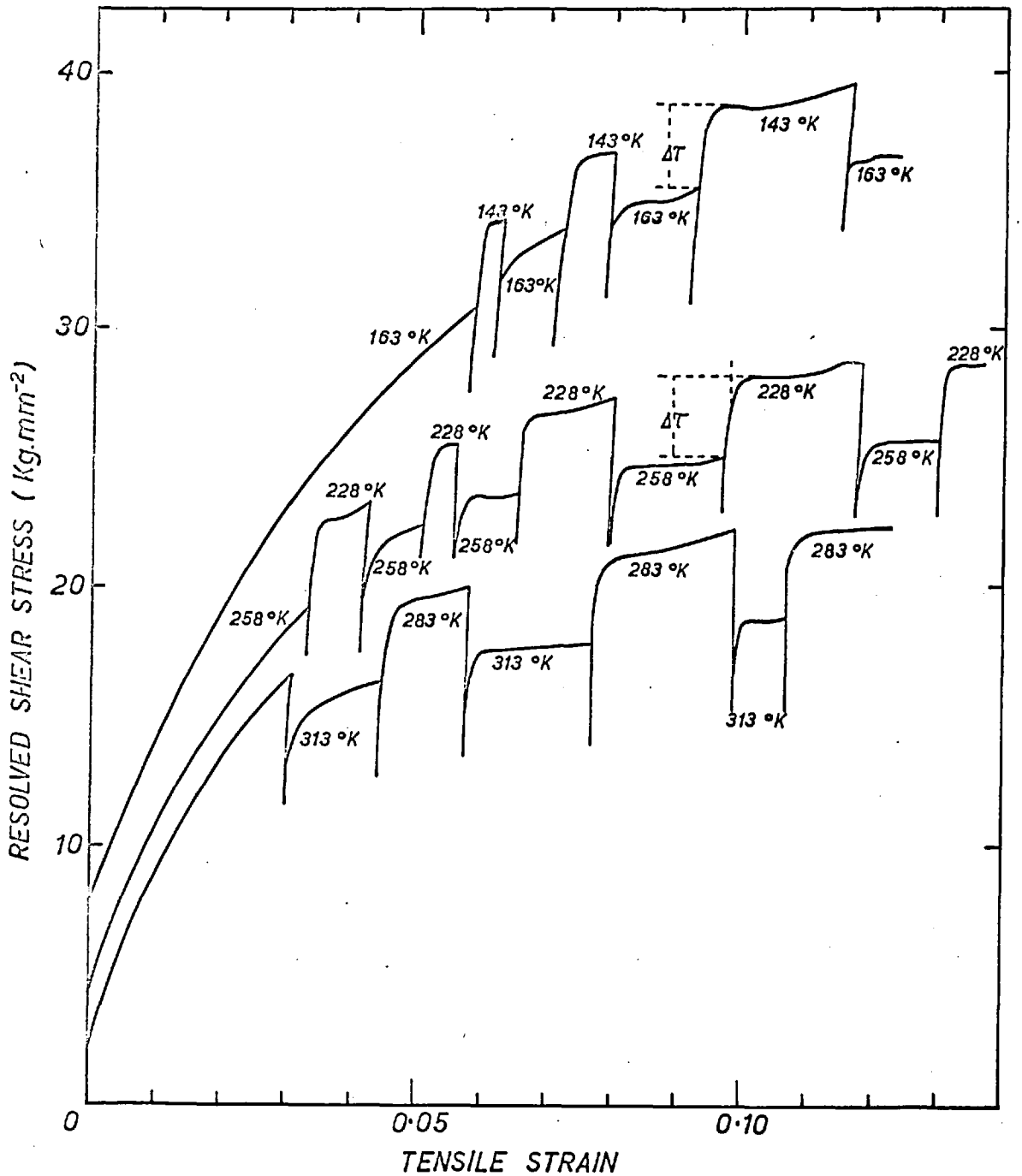


Figure 5.26. Stress-strain curves for temperature cycling experiments.

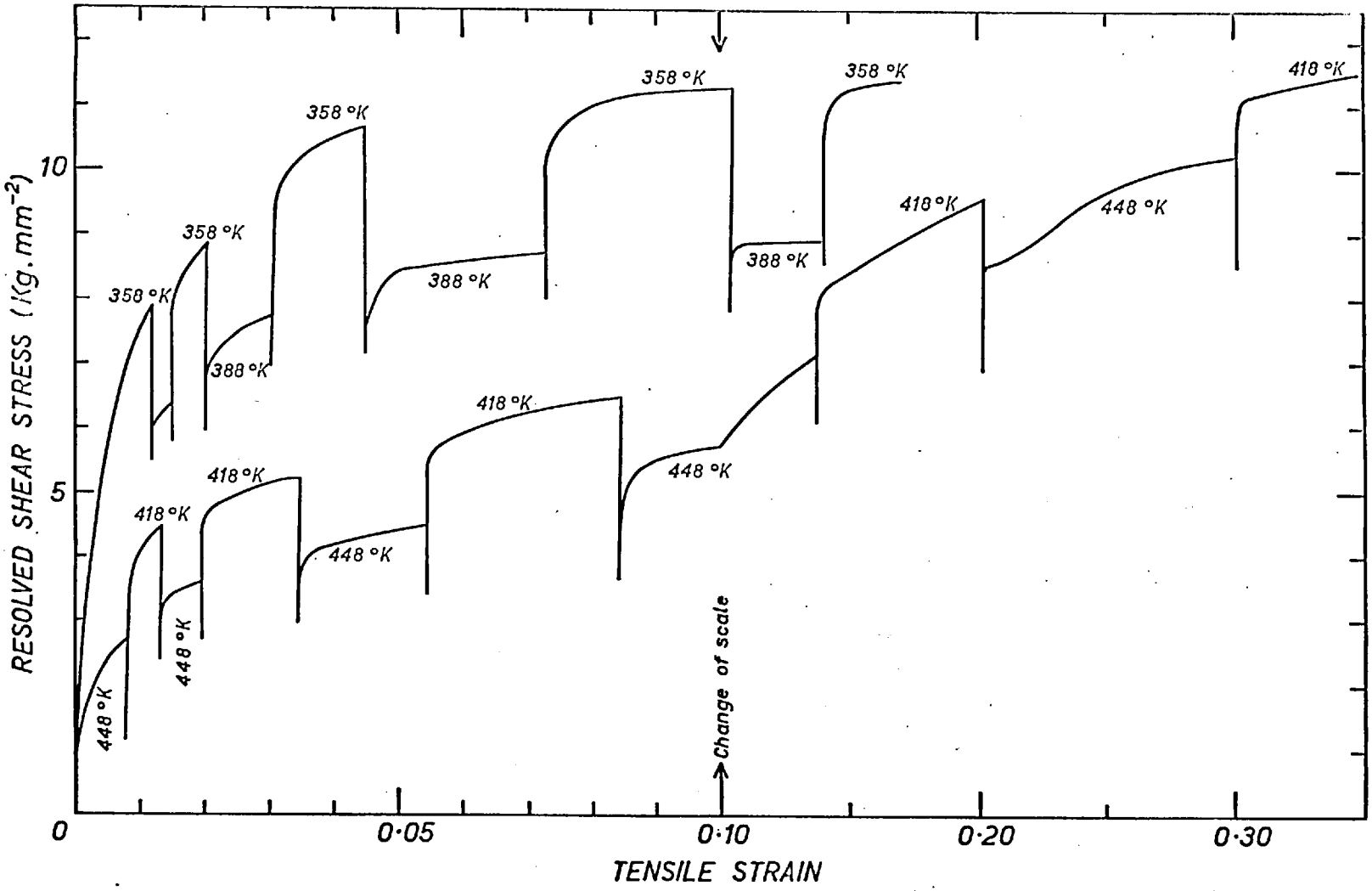


Figure 5.27. Stress-strain curves for temperature cycling experiments.

against the resolved shear stress, τ, in Figure 5.28. It is noticed that at 433°K $(\frac{\Delta\tau}{\Delta T})_{\dot{\gamma}}$ increases with stress initially and then decreases. At 373°K and 298°K there is a steady increase in $(\frac{\Delta\tau}{\Delta T})_{\dot{\gamma}}$ with stress. $\frac{\Delta\tau}{\Delta T}$ is independent of stress at 243°K and decreases with stress at lower temperatures.

Also included in Figure 5.28. is a dotted line obtained from continuous stress-strain curves at 243°K and 298°K. The experimental points indicate $(\frac{\Delta\tau}{\Delta T})_{\dot{\gamma}}$ values obtained from differential temperature cycling tests between these two temperatures conducted at the same strain rate. It is found that within experimental error there is good agreement between the $(\frac{\Delta\tau}{\Delta T})_{\dot{\gamma}}$ values obtained by both methods. This indicates that the variation of long range internal stress, τ_μ, with temperature is negligible.

5.10. Stress Relaxation Experiments

Strain rate sensitivity has also been determined using a stress relaxation method. This method has several advantages over conventional strain rate change experiments.

a. It is possible to measure the strain rate sensitivity, λ, at early stages of deformation where the work hardening rate is very high.

b. True values of λ can be obtained at a definite stress rather than at a mean stress.

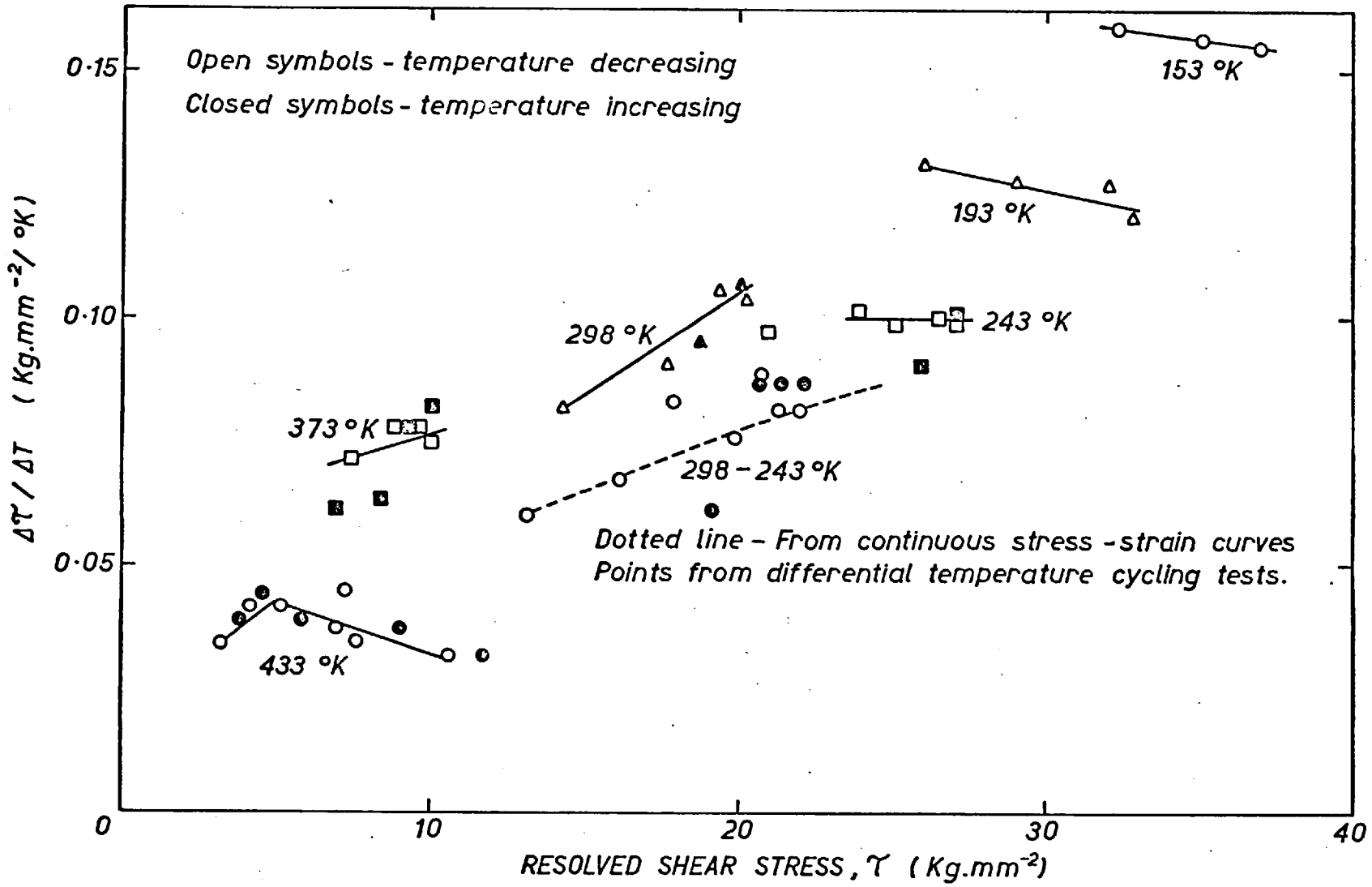


Figure 5.28. Variation of $\frac{\Delta\tau}{\Delta T}$ with applied stress at various temperatures.

During the relaxation experiments the specimen was loaded to a certain stress and the cross head was stopped. The specimen continued to deform under a decreasing stress and a decreasing strain rate. From the variation of the load with time a relaxation curve can be plotted showing the resolved shear stress τ as a function of time. While plotting such a curve a correction has to be applied to take into account the relaxation of the machine itself. Strain rate sensitivity λ can be calculated from this curve using any of the following two relations[79]:

$$\lambda_{(\tau^*)} = \frac{d\tau}{d \log \dot{\gamma}} = \frac{d\tau^*}{d \log (-\dot{\tau}^*)} \simeq \frac{d\tau}{d \log(-\dot{\tau})} \qquad (5.5.)$$

The slope of the plot τ versus $\log (-\dot{\tau})$ gives the value of λ. Also

$$\tau - \tau_o = \lambda \log C - \lambda \log (t + C) \qquad (5.6.)$$

where τ_o is the resolved shear stress at the start of the relaxation (time, $t = 0$). The constant C is chosen so that the plot τ versus $\log (t + C)$ is linear. The positive value of the slope of this plot is the strain rate sensitivity at that stress.

λ has been determined at different temperatures using

both methods. There was reasonable agreement between the two methods and mean values of λ have been plotted against applied resolved shear stress at these temperatures (Figure 5.24. and 5.25.). A specimen was strain rate cycled at 153^{o}K and relaxation tests were carried out at each strain rate in between strain rate changes. The λ values, calculated at both strain rates are plotted in Figure 5.24. It is found that λ is somewhat smaller at the higher strain rate than at the lower strain rate. Similar results were also obtained at 298^{o}K where relaxation tests were carried out in two specimens deformed at two different strain rates.

It is noted in Figures 5.24. and 5.25. that strain rate sensitivity increases with increasing stress at temperatures up to 273^{o}K. At 298^{o}K λ increases initially and then levels off at higher stresses. However, at 373^{o}K and 433^{o}K λ versus τ curves show a maximum at 5 kg/mm.^{2} and 8 kg/mm.^{2} respectively.

5.11. Calculation of Activation Parameters

Activation volume v^{*}, activation energy, H, and frequency factor υ for yielding and flow have been determined from the strain rate cycling, temperature cycling and relaxation experiments using equations 1.12., 1.11. and 1.13. In all these calculations it has been assumed that a single thermal activation process is rate controlling, the total energy to overcome the

obstacles to flow is not a function of stress, υ does not change during a change in temperature or strain rate, and the variation of the long range internal stress, τ_μ, with a change in temperature or strain rate is negligible in comparison to the corresponding variation in the effective stress τ^*, i.e. $\Delta\tau \simeq \Delta\tau^*$.

5.11.1. Activation Volume

Activation volume v^* has been obtained from the relation

$$v^* = \frac{2.3\ kT}{\lambda} \qquad (5.7.)$$

using the λ values derived from strain rate change and relaxation experiments. The corresponding values of v^* have been plotted as a function of resolved shear stress in Figures 5.29. and 5.30. In these graphs applied shear stress τ rather than effective shear stress τ^* $(=\tau - \tau_\mu)$ has been used. However, it has been experimentally verified in Section 5.9. that the variation of τ_μ with temperature is negligible and the only effect of using τ instead of τ^* is to shift the curves to the right.

Activation volume is found to decrease with increasing stress. At lower stresses v^* and reaches values of a few hundred times b^3, but at higher stresses v^* tends to level off

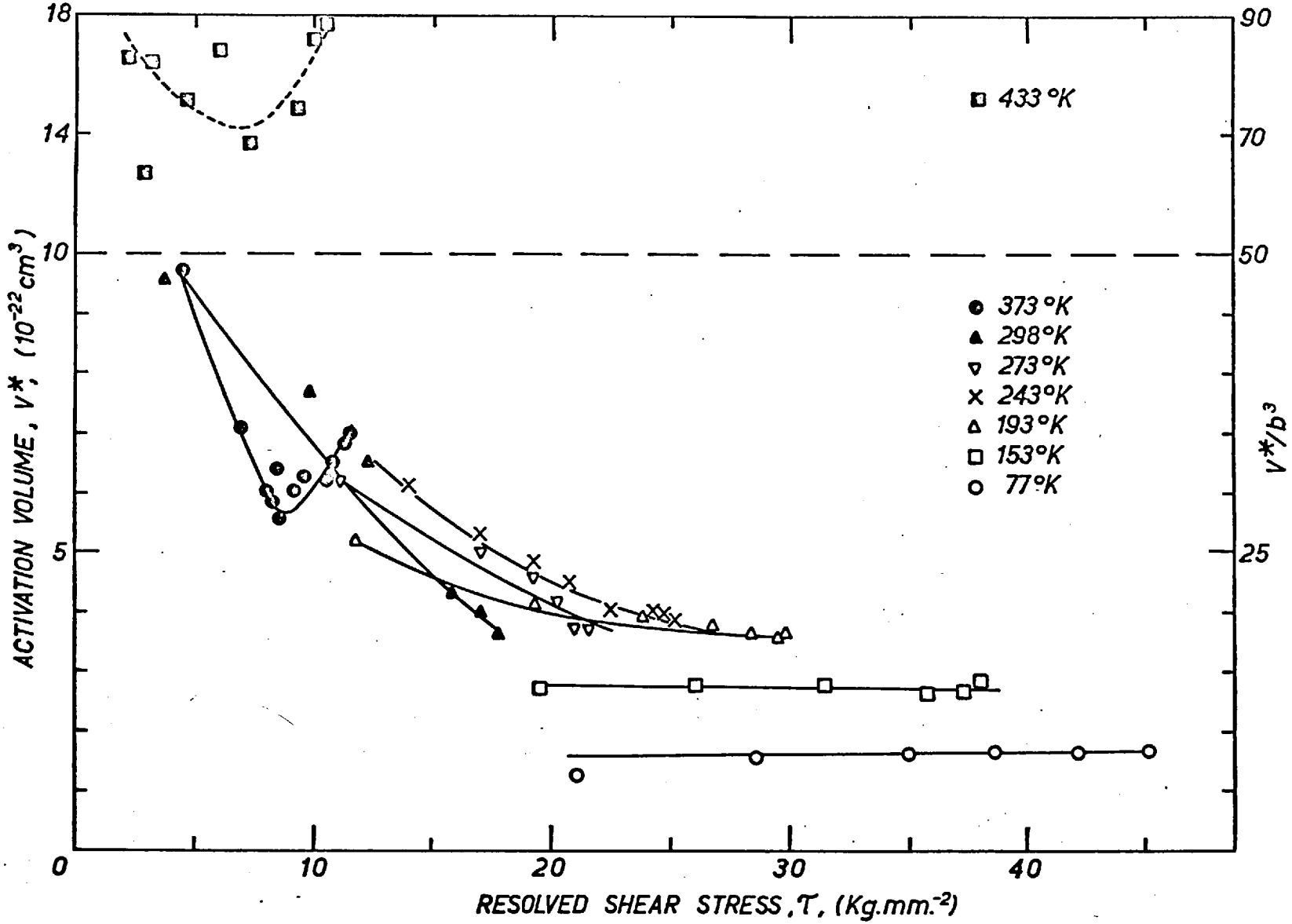


Figure 5.29. Variation of the activation volume with applied stress at various temperatures (calculated from strain rate change experiments).

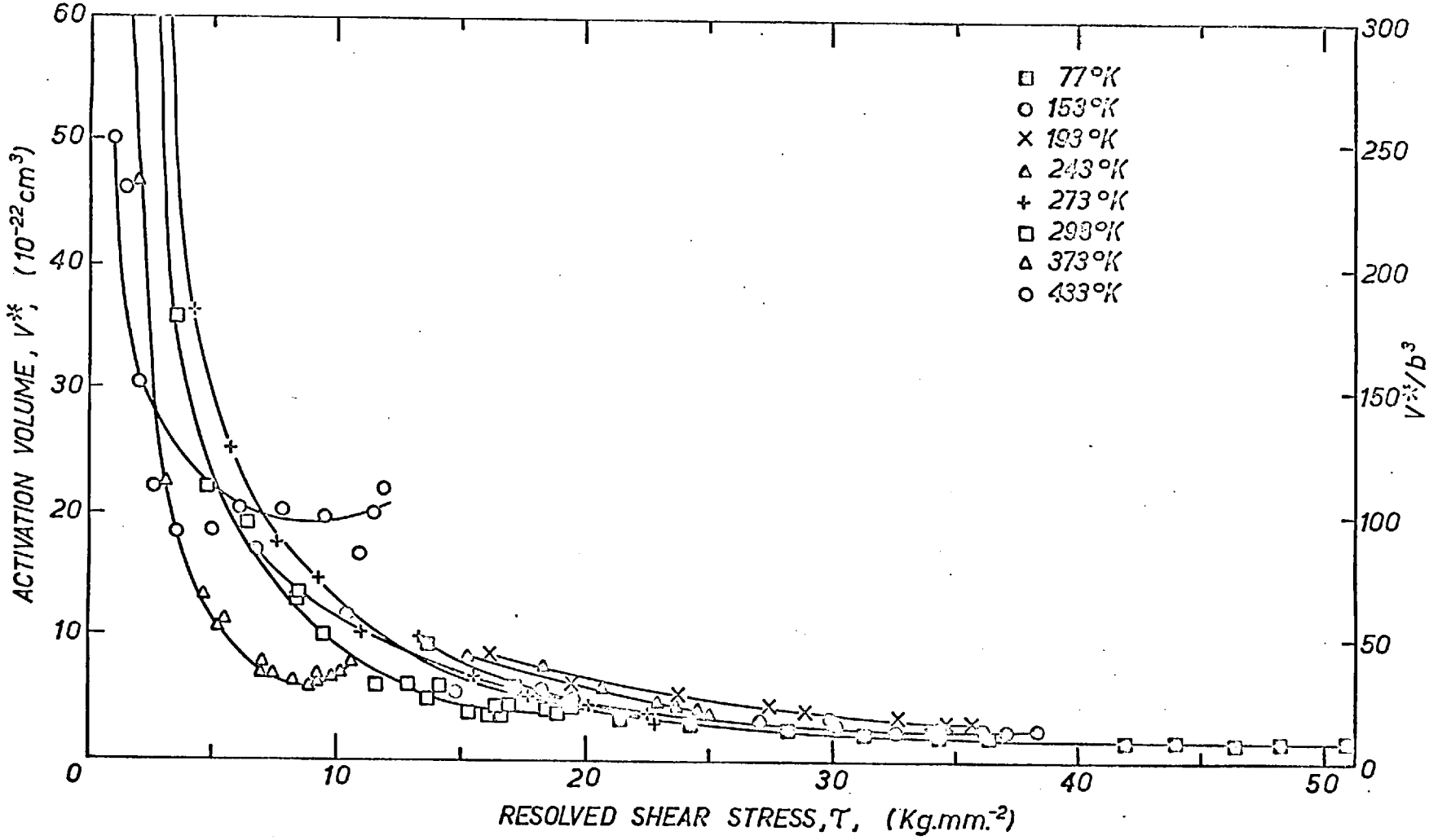


Figure 5.30. Variation of activation volume with applied stress at various temperatures (calculated from relaxation experiments).

at $\simeq 10\ b^3$ (Figure 5.30.). At 433°K and 373°K the v* versus τ plots go through a minimum which corresponds to the maximum observed in λ versus τ plot at these temperatures.

5.11.2. Activation Energy

Activation energy, H, has been calculated from the strain rate sensitivity, and the temperature sensitivity of flow stress using the relation:

$$H = -2.3 \frac{kT^2}{\lambda} \left(\frac{d\tau}{dT}\right)_{\dot{\gamma}}$$

$$= -T\, v^* \left(\frac{d\tau}{dT}\right)_{\dot{\gamma}} \qquad (5.8.)$$

The values of H, λ and v^* at a few strains and mean stresses are calculated at various temperatures and the results are given in Table 5.5. H has been plotted against temperature at a constant strain in Figure 5.31. It is more or less a linear plot and ν can be determined from the slope of this plot. H has also been plotted as a function of stress (Figure 5.32.) and is found to increase with decreasing stress.

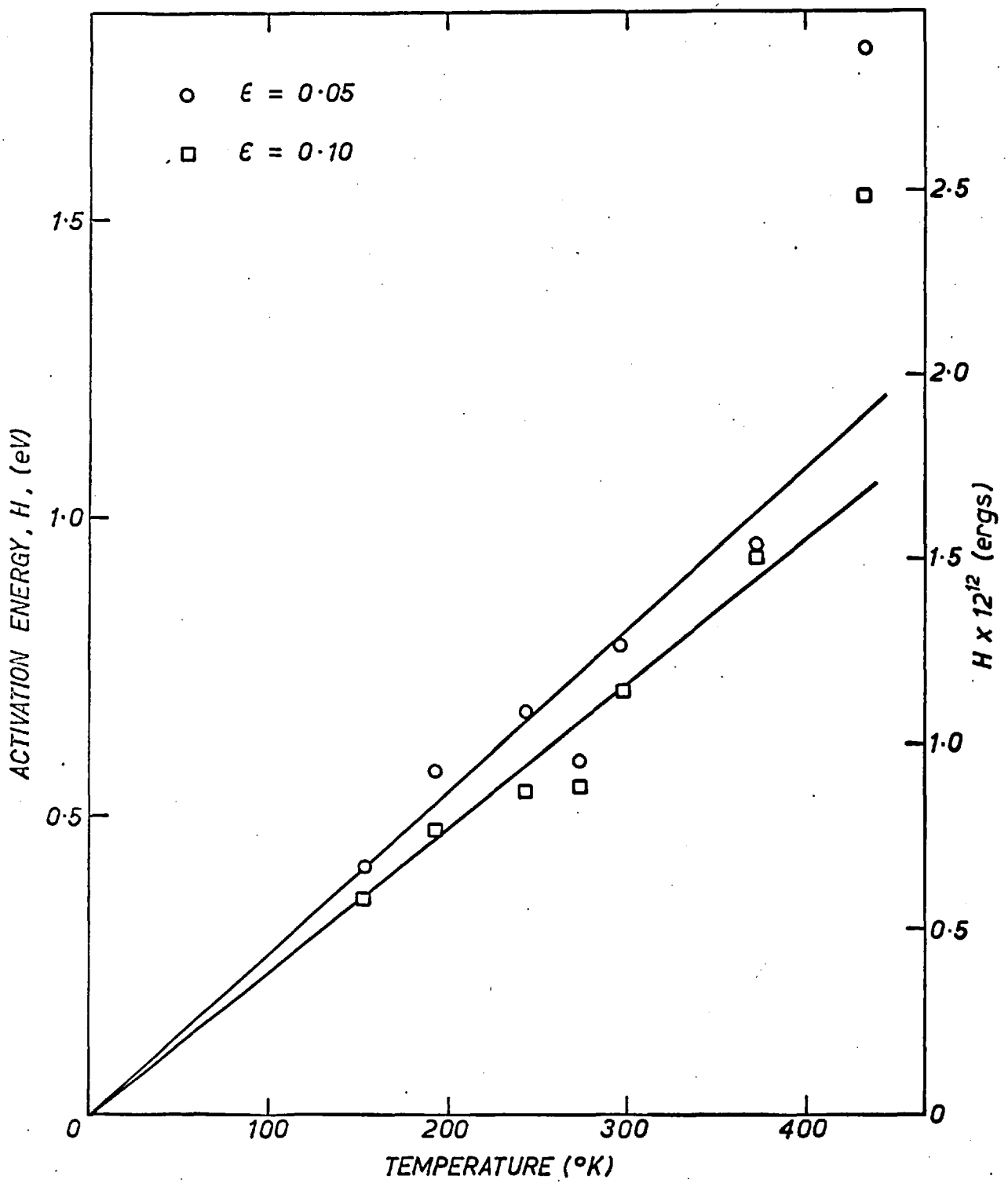


Figure 5.31. Variation of activation energy with temperature.

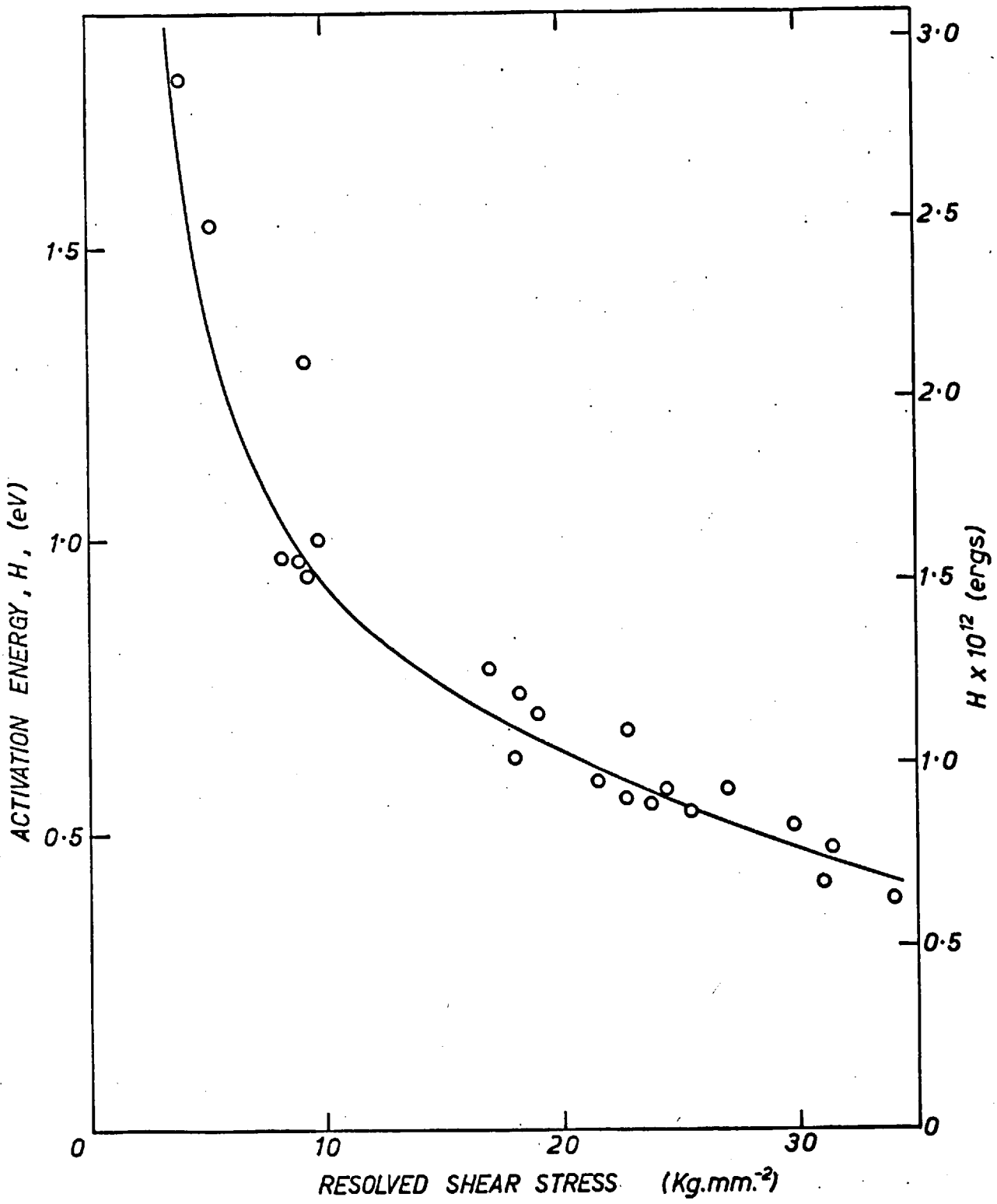


Figure 5.32. Variation of activation energy with applied stress.

Table 5.5.

Activation Parameters

Mean Temperature	Tensile Strain	Mean Stress ($kg/mm.^2$)	Activation Volume (10^{-22} $cm.^3$)	Activation Energy (10^{-12} ergs.)	Activation Energy (ev)
153	0.05	31.0	2.8	0.668	0.414
	0.07	34.8	2.7	0.628	0.390
	0.10	37.6	2.5	0.577	0.358
193	0.05	27.1	3.8	0.9294	0.576
	0.07	29.8	3.6	0.8293	0.514
	0.10	31.4	3.3	0.7652	0.474
243	0.033	20.2	6.4	1.360	0.843
	0.050	22.8	5.0	1.089	0.675
	0.07	24.5	4.3	0.930	0.576
	0.010	25.5	4.0	0.866	0.537
273	0.03	18.0	4.8	1.101	0.627
	0.05	21.5	4.2	0.945	0.586
	0.07	22.8	3.9	0.898	0.557
	0.10	23.7	3.85	0.886	0.549
298	0.033	15.0	4.7	0.9616	0.596
	0.05	17.0	4.4	1.26	0.781
	0.07	18.2	4.0	1.192	0.739
	0.10	19.1	3.7	1.135	0.704

Mean Temperature ^{o}K	Tensile Strain	Mean Stress ($kg/mm.^2$)	Activation Volume (10^{-22} $cm.^3$)	Activation Energy (10^{-12} ergs.)	Activation Energy (ev)
373	0.03	8.2	6.2	1.565	0.970
	0.05	8.9	6.0	1.536	0.952
	0.10	9.2	5.8	1.507	0.934
	0.15	9.8		1.622	1.00
433	0.3	4.0	16.0	2.888	1.79
	0.05	3.9	16.0	2.888	1.79
	0.10	5.2	14.7	2.497	1.54
	0.30	9.2	15.5	2.106	1.30

5.12. Discussion

5.12.1. Stress-Strain Curves

The stress-strain curves for molybdenum single crystals with the tensile axis near the centre of the unit stereographic triangle are parabolic in shape with a high initial work hardening rate. The proportional limit values are very low and are plotted against temperature in Figure 5.33. for the three different strain rates used. Also included in this figure are the corresponding plots obtained by Guiu[157] for specimens of similar orientation, but with a much larger dislocation density. It is noted that in the present case the proportional limit values are considerably lower than those obtained by Guiu. This is also confirmed by the higher proportional limit of the unannealed specimen tested at 243^{o}K.

At first sight the lower proportional limit of specimens with the low dislocation density may look ambiguous, since to keep up the imposed strain rate and to show a detectable amount of deformation these dislocations would have to move long distances at a fast speed, which requires a higher stress. However, the applied stress at the proportional limit consists of a long range internal stress and an effective stress acting on the dislocation. It is possible that in specimens of high dislocation density the long range internal stress may be quite high so that the effective stress is much lower than the applied stress. In the present

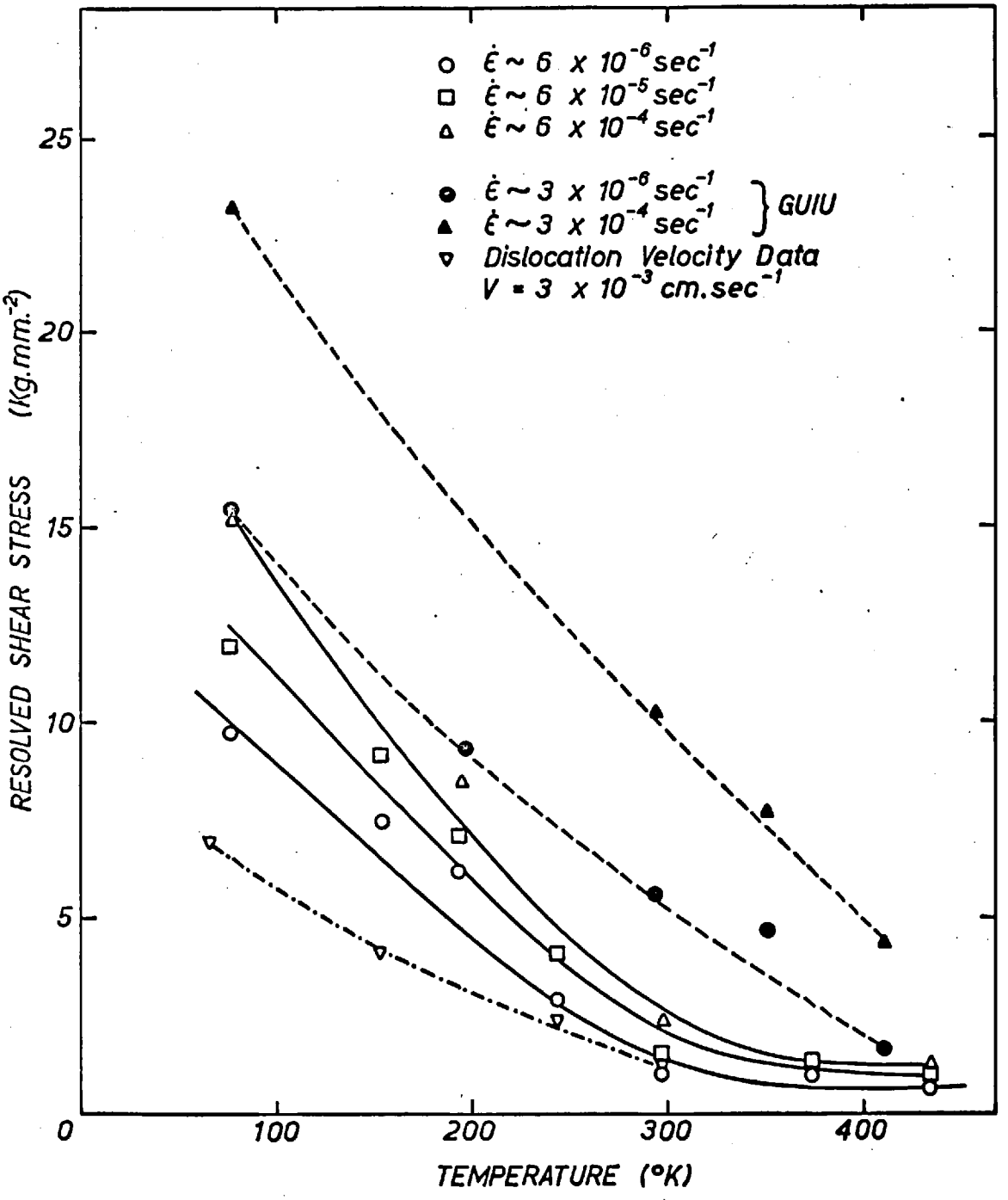


Figure 5.33. Effect of temperature on the proportional limit.

case, due to the low initial dislocation density, the long range internal stress is probably very small and the applied stress to start macroscopic yielding may be consequently lower. At temperatures lower than 300°K the temperature dependence of proportional limit is almost the same for specimens of both high and low dislocation density. However, above 300°K the proportional limit of low dislocation density specimen shows very little change, whereas that of the high dislocation density specimen still continues to decrease with increasing temperature. It is possible that in the former case the thermal obstacles to the movement of dislocations at the proportional limit may be becoming transparent at this temperature and the applied stress has to overcome only the long range internal stress.

The flow stresses of crystals at 2% tensile strain have been plotted against temperature in Figure 5.34. for the various strain rates used. The corresponding curve obtained by Guiu[167] is also included in this figure for comparison. It is found that the specimens of low dislocation density have a lower flow stress and the temperature dependence of the flow stress is also lower. However, this lower temperature dependence may as well have been a result of purification during the long high temperature annealing. One striking difference between the temperature dependence of the flow stress and the

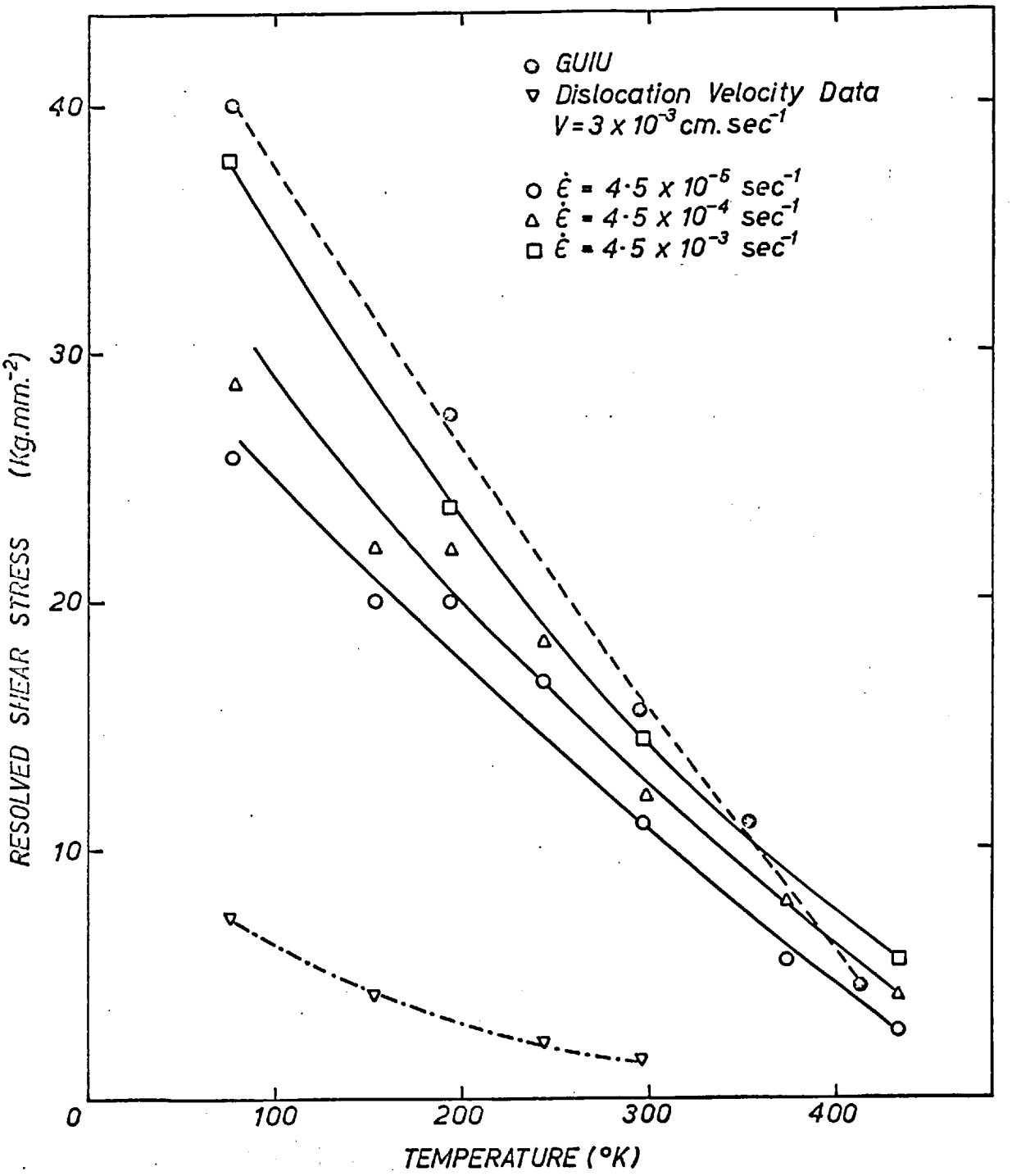


Figure 5.34. Flow stress at 2% tensile strain plotted against temperature.

proportional limit in the low dislocation density specimens is that the flow stress steadily decreases even up to 433°K whereas the proportional limit tends to level off after approximately 300°K. In the former case one is dealing with a large density of dislocations whereas in the latter case the dislocation density is still very small. So a possible explanation for this difference in temperature dependence may be the creation of new thermal barriers during deformation in this temperature range. This barrier may be the nonconservative motion of jogs produced by cross slip during the multiplication process, or may be the intersection of dislocations.

The work hardening rates at various temperatures in the present case are almost the same as that obtained by Guiu, but they are still much larger than the corresponding values obtained by Lawley and Gaigher[64] in specimens of a similar orientation, machined by electropolishing. It cannot be explained in terms of the initial dislocation density as the annealed specimens used in the present investigation have a considerably lower dislocation density. No definite explanation can be offered in the absence of a proper understanding of the work hardening mechanisms in b.c.c. metals.

The range of temperature and strain rates used to study three stage hardening in the present case are not very extensive,

but the limited number of results compare well with those obtained by Mitchel et al.[106] in niobium single crystals. From Figure 5.5. and Table 5.4. one finds that θ_I increases with increasing temperature, and θ_{II} decreases with increasing strain rate as shown in Figures 10 and 12 of Mitchel et al.'s paper[106] respectively.

The softening observed in Stage I may be the result of the collapse of obstacles formed during the high work hardening in Stage 0. It is also noted in Figure 6.5. that when Stage 0 is longer the softening in Stage I is more pronounced. This may be due to the collapse of larger number of obstacles. These results indicate the similarity between Group VA and Group VIA metals in their deformation behaviour. The difference between these metals is the recovery transition temperature above which easy glide and three stage hardening may occur. This temperature is lower in case of Group V metals.

5.12.2. Crystallography of Slip and Active Slip Systems

Though the orientation of the specimens is favourable for single slip in the $(\bar{1}01)$ $[111]$ system slip takes place in a number of systems during deformation at all the temperatures. Similar observations have been made by Lawley and Gaigher[64] and Guiu[167] in molybdenum single crystals of similar orientations. Even at high temperatures, at which three stage hardening takes place and the specimen axis moves towards $[111]$

multiple slip is observed from the early stages of deformation. The other observation at these temperatures is the tensile axis, overshooting of the $[\bar{1}00]$ $[\bar{1}10]$ symmetry line by a large angle. Similar overshooting has been observed by Mitchel et al.[106] and Taylor et al.[181] in niobium single crystals and by Keh[188] in iron single crystals. This may be due to the hardening in the secondary system or the lower density of mobile dislocations in the secondary system.

$(\bar{1}01)$ $[\bar{1}11]$ and (101) $[\bar{1}11]$ slip systems with Schmid factors of 0.5 and 0.47 respectively are operative at all temperatures. Slip on {112} planes is scarcely observed below room temperature but at higher temperatures there is evidence of cross slip on {112} planes.

In b.c.c. metals slip has been reported in a number of slip systems and it is believed that slip can occur in any of the {110}, {112} and {123} planes of the <111> zone. Andrade and Chow[191] have tried to correlate the active slip systems with the test temperature. Schadler[192] and Erickson[51] working with tungsten and silicon iron single crystals respectively found that {110} slip planes are favourable at lower temperatures and {112} at higher temperatures. Slip on the plane of maximum resolved shear stress has been reported by Sestak and Libovicky[193] and Noble and Hull[194] in silicon iron and by Ferris et al.[180] in tantalum. It is also possible that

noncrystalline slip or even slip in {112} planes may be a result of composite slip on non-parallel {110} planes.

The present investigation lends support to the view that slip is crystallographic in molybdenum single crystals and takes place predominently on {110} planes, though{112} planes may operate at higher temperatures. As the specimens were oriented near the centre of the unit stereographic triangle with maximum resolved shear stress on a $(\bar{1}01)$ plane it is difficult to draw any general conclusion as to whether {110} or {112} slip is more favourable. However, the present observations are in contrast to those of Guiu[167] who observed predominently {112} slip in his specimens. It is difficult to predict how the initial dislocation density could possibly have affected the operating slip systems.

Considering the nature of slip lines, the long deep slip lines observed at low temperatures must have formed continuously as no load drop was observed during the tensile test. The branching of the broom stick slip band might have resulted from profuse cross slip during the growth of the band.

5.12.3. Deformation and Dislocation Density

The possible reasons for the low value of C' ($= \frac{d\rho}{d\varepsilon}$) have been discussed in Section 5.7. Those explanations get further support from Reid et al.[195] who have found a striking

correlation between the initial dislocation density, ρ_o, and C' in different materials. The relation :

$$C' = K\sqrt{\rho_o}$$

where K is a constant is found to hold good for molybdenum. C', determined by Gilbert et al.[190] for polycrystalline molybdenum and by Lawley et al.[64] for molybdenum single crystals is about 10^2 times larger than that of the present investigation. However, the initial dislocation density in the present case is about 10^4 times less than those of the above mentioned workers, which explains the smaller value of C'. It may be inferred from these results that the average distance travelled by a dislocation is a sensitive function of ρ_o, and ρ_o plays an important role in the multiplication of dislocations during the deformation.

The small intercept on the stress axis, in the $\sqrt{\rho}$ versus τ plot, indicates that the composite friction stress is almost negligible in specimens of low dislocation density.

5.12.4. Strain Rate and Temperature Sensitivities of Flow Stress

Conflicting results have been reported in the literature on the temperature and strain rate sensitivities of the flow stress in b.c.c. metals. Basinski and Christian[120] found that in iron λ decreases with stress at 300°K, is independent of stress at 180°K and increases with stress at 78°K. Conrad and Frederick's[196] result in vacuum melted iron indicates a decrease in λ with stress at 200°K and higher temperatures and no stress dependence at lower temperatures. Christian and Masters[121] found that for Group VA and Group VIA metals λ shows a decrease in the early stages of the deformation and then remains almost constant. Single crystals of iron[114] have shown an increase in λ with stress at higher temperatures and stress independence at lower temperatures. Guiu[133] has reported that in molybdenum single crystals of $[\bar{1}10]$ orientation λ increases very rapidly at the proportional limit and remains constant during subsequent flow. On the other hand, for [100] orientation λ shows a steady increase with stress. At 413°K both orientations have a maximum in λ-τ plot.

In the present investigation, crystals with tensile axis near the centre of the unit stereographic triangle behave somewhat differently. At 433°K and 373°K the maximum in the λ-τ plot occurs at the stress where easy glide region starts. The initial increase in λ may be associated with the large work

hardening rate in Stage O, when new obstacles are created. In the easy glide region these obstacles collapse and the number of mobile dislocations increases. To keep up the increase in strain rate, the dislocations do not require a high stress and λ decreases consequently.

At temperatures between 298°K and 193°K λ increases steadily with stress and at lower temperatures λ is almost independent of stress. One may explain this variation λ-τ relation with temperature in terms of the change in dislocation configuration with strain at different temperatures. In molybdenum single crystals of similar orientation Lawley and Gaigher[64] have found that dislocation tangling occurs more readily with deformation at higher temperatures, whereas at lower temperatures dislocations are comparatively straight and uniformly distributed. When the dislocations get more and more tangled with increasing strain the effective number of mobile dislocations will be smaller and a higher stress increment would be necessary to keep up the same increment in strain rate. At lower temperatures the density of mobile dislocations probably remains fairly constant with stress.

One may note in Figures 5.24. and 5.25. that at lower stresses the values of λ calculated from strain rate change experiments are much larger than the corresponding values calculated from stress relaxation tests. This may be due to

the high initial work hardening in the stress-strain curves at lower stresses which gives a large stress increment when the strain rate is increased. For the same reason the $\Delta\tau$ values during a decrease in strain rate would be smaller as has been verified experimentally.

Temperature change experiments of Basinski and Christian[120] in iron indicate that $(\frac{\Delta\tau}{\Delta T})_{\dot{\varepsilon}}$ is independent of stress. On the other hand, Conrad and Frederick[196] have found a decrease in $(\Delta\tau/\Delta T)_{\dot{\varepsilon}}$ with stress. In iron single crystals of Mordike and Haasen[114] $\frac{\Delta\tau}{\Delta T}$ was found to increase with stress at temperatures above 78°K. The present results showing an increase in $(\Delta\tau/\Delta T)_{\dot{\varepsilon}}$ with stress at higher temperatures may again be a result of increasing dislocation tangling with strain at higher temperatures. But it is difficult to explain why it should decrease with stress at lower temperatures. However, the absolute value of $(\frac{\Delta\tau}{\Delta T})_{\dot{\varepsilon}}$ increases with decreasing temperature in agreement with the results of other workers.

5.12.5. Activation Parameters

The variation of activation volume with stress (Figures 5.29. and 5.30) is similar to the results obtained by Conrad and co-workers[118,119] in iron and other b.c.c. metals. The values of activation volume are almost the same as those obtained by Conrad[119] from yielding and flow data of both polycrystalline and

single crystal molybdenum.

v* is found to be dependent on temperature and at the same stress, it is larger at higher temperature (Figure 5.30.). However, the stress values reported here are applied stress rather than effective stress. The other point that may be noted here is that the activation volume goes on decreasing even after the proportional limit. This may be because v* depends on the structure or else the effective stress increases with increasing strain.

Activation energy is found to be a sensitive function of stress, but is independent of strain ~~and temperature~~. Between 373°K and 433°K there is a sudden increase in H. This may be due to a change in the rate controlling mechanism or the effective stress nearly becoming zero at this temperature. However, the τ-T curves at 2% tensile strain show that τ is still decreasing at 433°K. However, Conrad's value of 450°K[119] for T_o (for $\tau^*=0$) is not very far from 433°K and, although Conrad used experimental data for a different material, it will be interesting to do some tensile tests at temperatures above 433°K.

The structure ~~and temperature~~ independence of H favours the P.N. force as the rate controlling mechanism. The activation energy values are also in agreement with the double kink nucleation mechanism of Seeger[92] and Dorn and Rajnak[95].

The frequency factor ν has been calculated from the slope

of H-T plot in Figure 5.31. ν has an average value of 2.75×10^{10} at 5% tensile strain and 5.08×10^{8} at 10% tensile strain. The lower value of ν at the higher strain indicates that the density of mobile dislocations or the distance moved by the dislocation after a successful thermal activation may be decreasing with increasing strain.

CHAPTER 6.

MOBILITY OF DISLOCATION IN MOLYBDENUM SINGLE CRYSTALS

6.1. Introduction

A knowledge of the mobility of individual dislocations is essential for a proper understanding of the plastic deformation of materials. In the past few years such studies in single crystals of alkali halides, semiconductors and certain metals and alloys have modified some of our ideas in the field of yielding and flow. However, the direct measurement of dislocation velocity has been rather limited to a few metals due to the many inherent difficulties. During the present investigation with molybdenum single crystals two such primary obstacles, namely development of a suitable etchant and the reduction of grown-in dislocation density were surmounted, and as a next step it was decided to measure dislocation velocities as a function of the applied stress and temperature.

6.2. Experimental Techniques

The experimental technique used in the present investigation for the measurement of dislocation velocities was very similar to the scratch method of Stein and Low for dislocation mobility studies in silicon-iron single crystals.

6.2.1. Ageing of Specimens

The annealed specimens were aged in vacuum at a temperature of 450°C for 5 hours and then slow cooled to pin the grown-in dislocations and prevent their motion during the subsequent application of load. At 77°K the aged dislocations were effectively pinned, but at higher temperatures unpinning became a problem.

6.2.2. Introduction of Fresh Dislocations

Fresh dislocations were introduced into the specimen surface by drawing a scratch with a diamond scriber, shown in Figure 6.1. The scriber unit consists of a ground point polished scribing tool with a 60° angle and minimum nose radius, supplied by Indusmond Diamond Tool Ltd. It is mounted on a stainless steel holder screwed in to one end of a horizontal tuffnol rod. This rod acts as a lever system and is balanced by a movable weight at the other end. During the scribing, load is applied by putting dead weights on a pan mounted directly over the tool holder.

The scriber is driven by a variable speed, reversible, 12 volt motor. The specimen is held in a stainless steel jig with its long edge parallel to the direction of scribing. Just below the specimen holder, a polystyrene beaker encased in a stainless steel beaker and an insulating container, is mounted

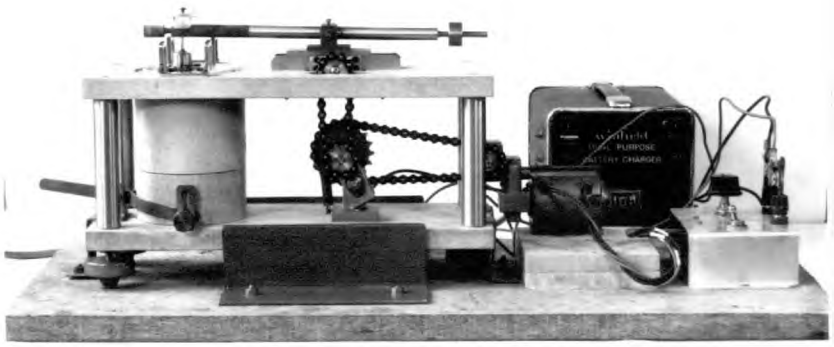


Figure 6.1. Diamond scriber to draw a scratch on the specimen.

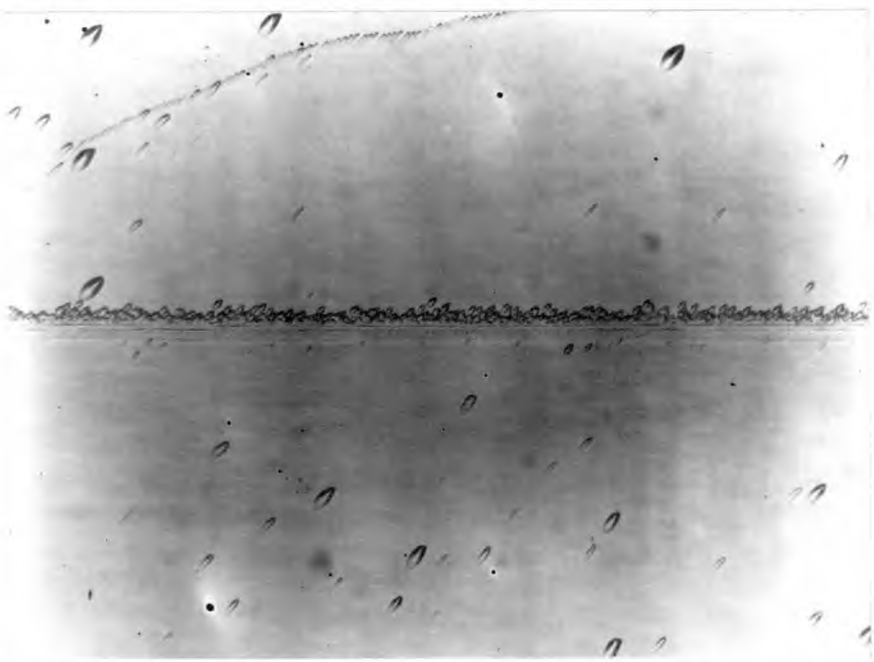


Figure 6.2. Etch pits near a scratch in molybdenum single crystal. x 200.

on a lifting device. The diamond tool is set at an inclination so that it makes an angle of approximately 2^{o} with the specimen surface.

Before the scratch was drawn the polystyrene beaker was filled with liquid nitrogen and lifted up so that the specimen remained immersed in liquid nitrogen. Scratching at a low temperature was necessary to prevent the pinning of fresh dislocations near the scratch by the migration of interstitial impurity atoms. A load of 2 grams and a tool travel speed of 4 cm./min. were used during scratching.

Dislocation etch pits near a scratch are shown in Figure 6.2. It is found that there are more dislocation etch pits on one side of the scratch than on the other. Similar observations have been made in silicon iron and tungsten[50, 57]. This may have been due to an uneven stress distribution on both sides of the scribing tool during scratching. When a load was applied to the scratched specimen, dislocations usually moved from the side with a larger number of dislocations.

6.2.3. Application of Load

The specimen was stressed in a four-point bending jig with a span of 20 mm. between the end contact points and a 10 mm. span between the middle contact points. (Figure 6.3) Load was applied with a table Instron (Model TM-M-L) provided with a 100 kg. load cell.

A high cross head speed was used so that the time to reach the desired load was very short and the load was maintained manually by moving the cross head at a slow speed to compensate for any relaxation in the specimen or the machine.

The test temperature was obtained by immersing the frame, jig and specimen (Figure 6.4.) in a low temperature bath contained in a Dewar flask. About 20 minutes were allowed between the immersion of the specimen in the temperature bath and the load application so as to reach equilibrium.

6.2.4. Measurement of Dislocation Velocity and Stress Calculation

To measure the velocity of dislocations, the annealed and aged specimen was electropolished, etched and scratched under liquid nitrogen with the diamond scriber. Then it was stressed in four point bending at a predetermined load for a predetermined length of time and re-etched. The maximum distance travelled by the dislocation etch pits from the scratch was measured under a Reichert photomicroscope at a magnification of x 200 or x 500. That, the outermost dislocations in an array were the first to move was verified by repeated electropolishing and etching, when the outermost ones were the last to disappear.

In all these measurements the stress was always below the macroscopic yield stress and was calculated assuming complete elastic behaviour. The standard equation for maximum fibre



Figure 6.3. Four-point bending jig with a specimen.

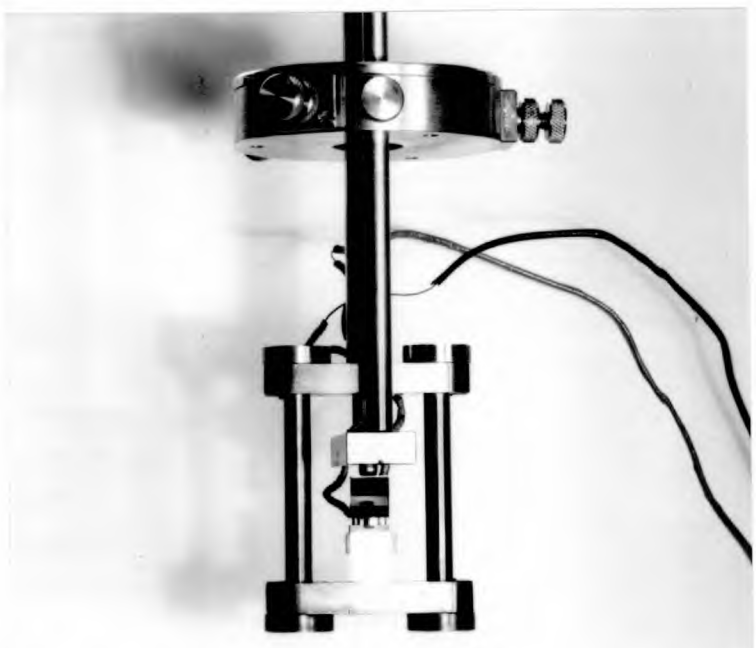


Figure 6.4. Frame, jig and specimen in the Instron machine.

stress, σ_{max}, in a laterally loaded symmetrical beam was used.

$$\sigma_{max} = \frac{M}{Z} \qquad (6.1.)$$

where M is the bending moment and Z is the section modulus. In the case of a rectangular cross section $Z = \frac{bh^2}{6}$, where b and h are the width and the thickness of the specimen respectively.

Distance moved by dislocations from the scratch was measured only in the centre span where the stress remained constant. A large number of measurements could be made in this region and the average value seemed most reasonable. Velocity of dislocation was calculated by dividing the distance by the time of loading.

In these measurements, a correction should be applied for the residual stress associated with the scratch. Assuming that this residual stress acts in the same sense as the applied stress, the dislocations would move faster in the region over which the residual stress acts. Using Erickson's method[51], a correction of 30μ was experimentally estimated and was subtracted from the actual distance travelled by the dislocations from the scratch. This correction is very approximate, but considering the long distance of dislocation motion (≃300μ) the error involved must be negligible.

The other sources of error were subgrain boundaries and the

shape of the specimen as discussed by Schadler[57]. In the present investigation, the dislocations moving from the scratch were very often held up when they encountered a subgrain boundary (Figure 6.5.). Sometimes when the misorientation across the sub-grain boundary was very small the dislocations could pass through it (Figure 6.6.). However, the sub-grain boundaries did not present a great problem, as dislocation motion at a constant stress was observed over a length of 10 mm. along the specimen surface. Though in some places the dislocations were held up at the sub-grain boundaries, this still left plenty of regions where dislocations had moved to the maximum distance without encountering any sub-grain boundaries or grown-in dislocations.

During electropolishing more material is removed at the edge of the specimen. This affects the stress calculation and also leads to a variation of stress across the specimen. This error was minimised by measuring the dislocation mobility in the centre section of the specimen surface.

The constancy of dislocation velocity at constant stress was checked by stressing a scratched specimen at the same stress for different lengths of time. It was found that within experimental error the distance moved was proportional to the time of loading, confirming that dislocation velocity is independent of the time of loading.

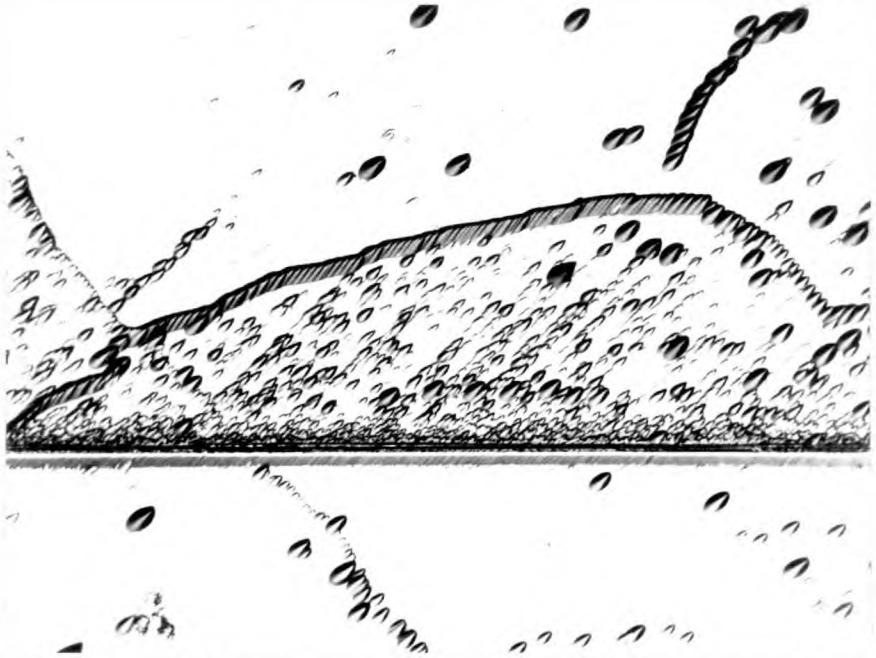


Figure 6.5. Dislocation motion from a scratch stopped at a sub-grain boundary. x 200.



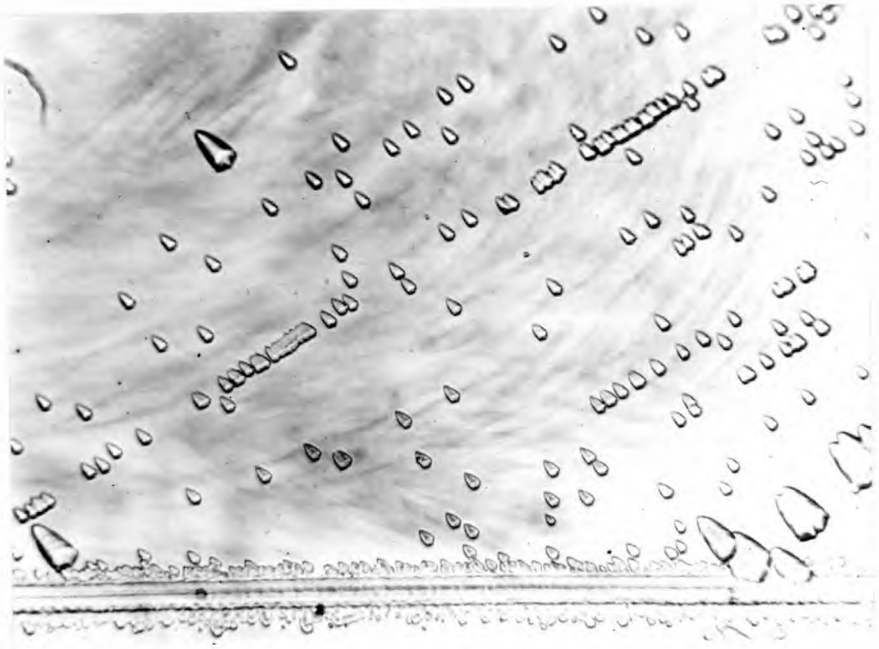
Figure 6.6. Dislocation motion from a scratch crossing the sub-grain boundary. x 500.

6.3. Results of Some Preliminary Experiments

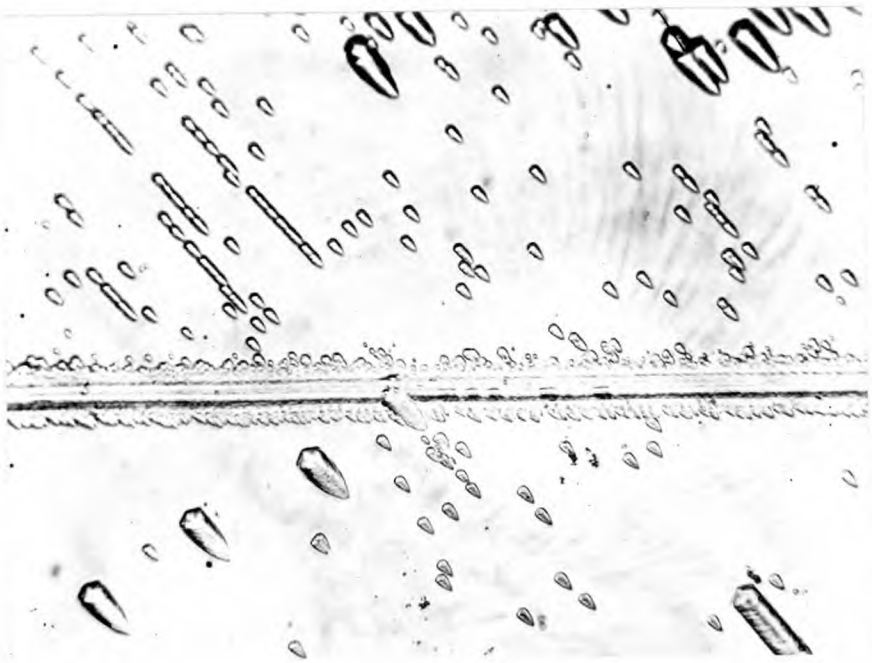
Before the development of the new etchant, some preliminary experiments were performed using the available etchants and the results are presented here in brief. As these etchants could not etch {112} or {110} planes, it was decided to measure the velocity of pure screw dislocations, for which the planes of observation were etchable. In the specimen, for pure screw dislocation motion in a $\{112\}\langle 11\bar{1}\rangle$ system, the dislocations moved very irregularly from the scratch. In the other batch of specimens for dislocation movement in a $\{110\}\langle 1\bar{1}1\rangle$ system. The dislocations did not move perpendicular to the scratch as expected. Instead, they moved at an angle of approximately 35°. The corresponding slip system was analysed and was found to be another $\{110\}\langle 1\bar{1}1\rangle$ system with a much lower Schmid factor than the expected system.

Next attempts were made to measure the velocities of mixed dislocations with 95% edge component and 5% screw component on a {110} plane. The plane of observation was {113}type. On application of a load two $\{110\}\langle 1\bar{1}1\rangle$ systems with very similar Schmid factors were found to operate and the dislocations moved in two different directions at an angle of approximately 90° with each other (Figure 6.7.).

However, this difficulty was solved with the new etchant which could etch planes very close to {112}, so that velocities



(a) x 200



(b) x 200

Figure 6.7. Dislocation motion in a specimen etched with the old etchant.

of almost pure edge dislocations could be measured.

6.4. Orientation and Geometry of the Specimens

The orientation of specimens used for the measurement of the velocity of almost pure edge dislocations is shown in Figure 6.8. The plane of observation was approximately 33° from (100) towards (111), i.e. about 2° from (112). The specimen was oriented for single slip with a Schmid factor of 0.5 on $(1\bar{1}0)[\bar{1}\bar{1}1]$ slip system.

6.5. Dislocation Motion at Various Stresses and Temperatures

The velocities of dislocations in molybdenum single crystal specimens were measured at four different temperatures; $77^{\circ}K$, $153^{\circ}K$, $243^{\circ}K$ and $298^{\circ}K$. At $77^{\circ}K$ the dislocation motion was very uniform and the etch pits were well aligned along the traces of the active slip plane (Figure 6.9.). But at higher temperatures the alignment of etch pits was less and less conspicuous. Figure 6.10. (a and b) shows the dislocation motion under a low applied stress at $243^{\circ}K$ and $298^{\circ}K$ respectively. This irregular motion may be due to cross slip becoming easier at higher temperatures.

Two other difficulties were encountered at higher temperatures. When the applied stress was low, i.e. at low velocities, relatively smaller number of dislocations were found to move from

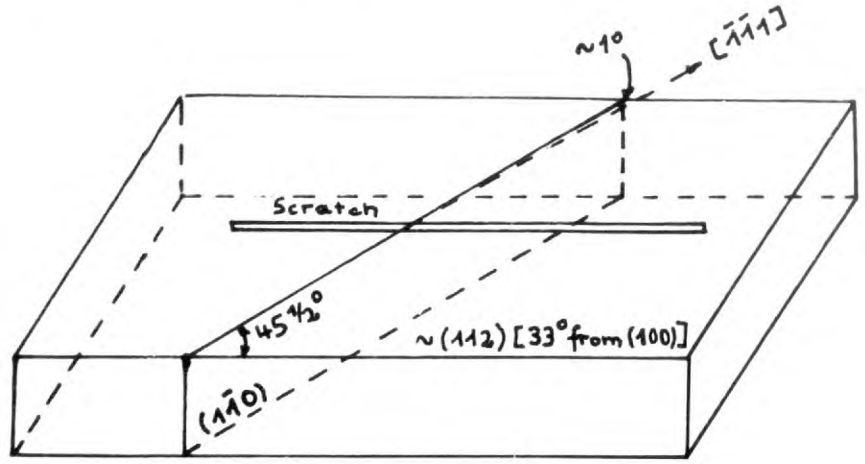


Figure 6.8. Orientation of a specimen used for edge dislocation velocity measurement on $(1\bar{1}0)$ plane. x 200

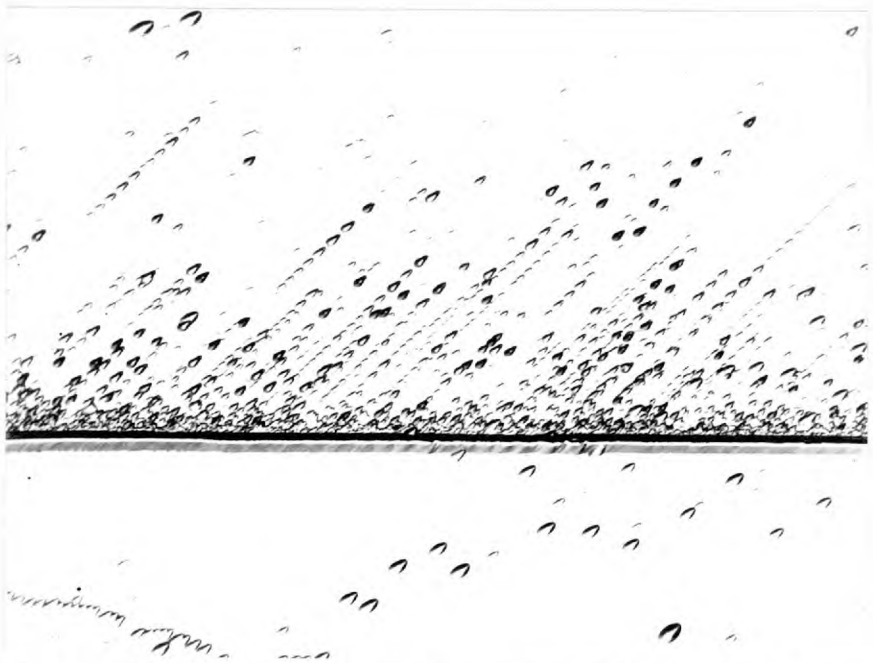


Figure 6.9. Dislocation motion from a scratch on a specimen stressed at a shear stress of 9.9 kg/mm.^{2} at 77°K for 100 sec. x 200.



Figure 6.10. (a) Dislocation motion from the scratch at 243°K. x 500.



Figure 6.10. (b) Dislocation motion from the scratch at 298°K. x 500.

the scratch. It is possible that some of the fresh dislocations introduced by scratching may be getting pinned by the migration of interstitial impurities. This is very much probable because at low stresses long times of loading were necessary to move the dislocations to a reasonable distance. At high stresses unpinning and multiplication of grown-in dislocations was a serious problem. Sometimes the motion of dislocations from the scratch was overshadowed by the formation of bands of etch pits running across the specimens along the traces of the active slip planes. Due to these reasons the results obtained at higher temperatures were not as reliable as those at 77°K.

6.6. Determination of the Slip System for Dislocation Motion by the Etch Pit Method

In Chapter 5, the analysis of the slip lines has shown that though the crystal was oriented for single slip in $(\bar{1}01)$ $[\bar{1}11]$ system, other slip systems with lower resolved shear stresses operated over the whole range of temperature. For dislocation velocity measurement one should precisely know the slip system in which the dislocations may be moving at a stress, lower than the macroscopic yield stress. As slip lines can be observed only at higher strains, when the situation is complicated by multiple slip, it was decided to determine the slip plane operating in the very beginning of plastic deformation.

This was done for specimens stressed in bending and tension, using the etch pit method.

The bending specimens had the same orientation and geometry as in velocity measurement (Figure 6.8.). The annealed specimens were electropolished, etched and then stressed just above their proportional limit in four point bending at different temperatures. The alignment of dislocation etch pits on the two perpendicular surfaces was studied after a second etch.

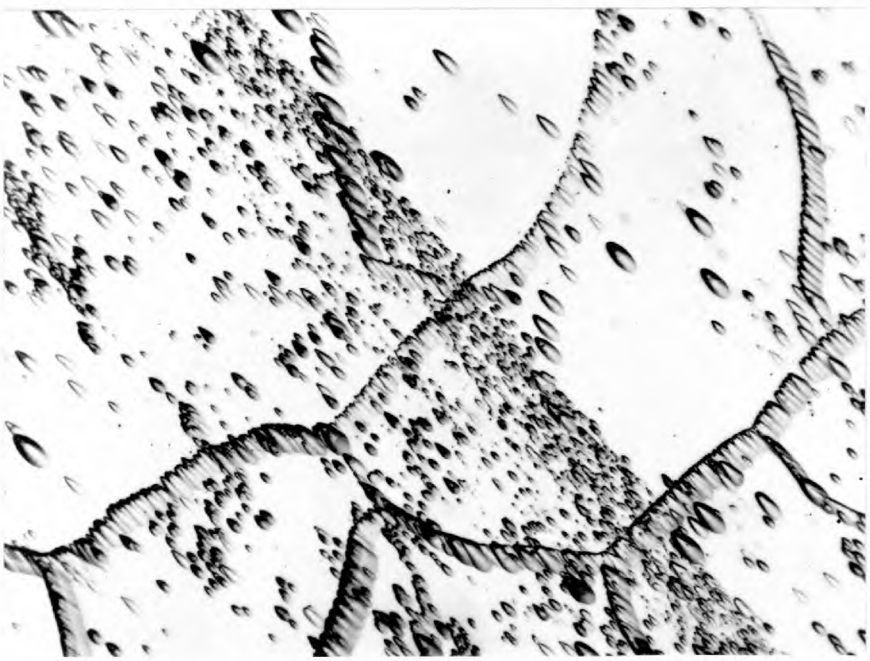
Figure 6.11. and 6.12. show the etch pit distribution on the top, ≈(112), surface and the side surface of a specimen stressed at 183°K. The results were very similar at 153°K, 203°K and 243°K. A few differences noted at 298°K and 77°K will be discussed later.

The alignment of the etch pits is identical on both the tension and compression surfaces of the specimen. Also on the faces perpendicular to the bending axis etch pit bands in the lower (tension) and upper (compression) parts make the same angle with the long edge of the specimen. This indicates that the same slip system is operating both in compression and tension in molybdenum single crystals, oriented near the centre of the unit stereographic triangle.

If the $(1\bar{1}0)\ [\bar{1}\bar{1}1]$ slip system with a Schmid factor of 0.5 were operative, the etch pit bands on the top face ≈(112) should make an angle of approximately $45\frac{1}{2}^{\circ}$ with the long edge of the



(a) x 50



(b) x 150

Figure 6.11. Dislocation etch pits on the (112) surface of the specimen (Figure 6.8.), stressed just above the proportional limit.



(a) x 50



(b) x 150

Figure 6.12. Dislocation etch pits on the side face of the specimen (Figure 6.8.), stressed just above the proportional limit.

specimen and would be perpendicular to the long edge on the side face, as is expected from the orientation. It is noted in Figure 6.11a. that etch pits are aligned at approximately 48^{o} to the long edge of the specimen on ≈(112) surface, but on the side face the etch pit alignment is at approximately 25^{o} to the long edge. The plane making these two traces is found to be (011). Taking the possible slip direction as $[1\bar{1}1]$, the corresponding Schmid factor would be ≈0.3. The same results were also obtained with a tensile specimen. When the applied stress was higher and in regions of stress concentration a second system was found to operate at the same temperature as shown in Figure 6.13. The plane for this trace is most probably $(0\bar{1}1)$, though there is a distant possibility that it may be $(1\bar{1}0)$.

At liquid nitrogen temperature, when the stress was low , dislocations moved on the (011) plane. This was also verified by stressing a specimen about ≈$[112]$ axis in an effort to measure the velocity of pure screw dislocations on (110) plane. As one can find in Figure 6.14., the dislocations instead of moving perpendicular to the scratch have moved at an angle. The wavy motion might have been due to cross slip. However, when the stress was higher dislocations also moved on $(1\bar{1}0)$ plane perpendicular to the scratch (Figure 6.15.).

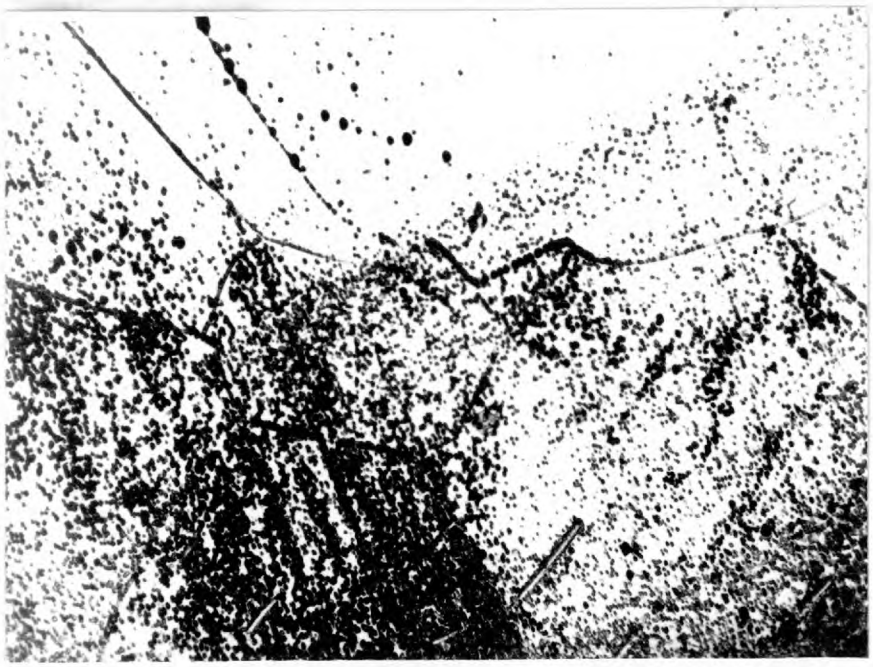


Figure 6.13. Dislocation etch-pits on the side face of the specimen (Figure 6.8.), stressed just above the proportional limit. A second slip system operating in a region of stress concentration. x 150.

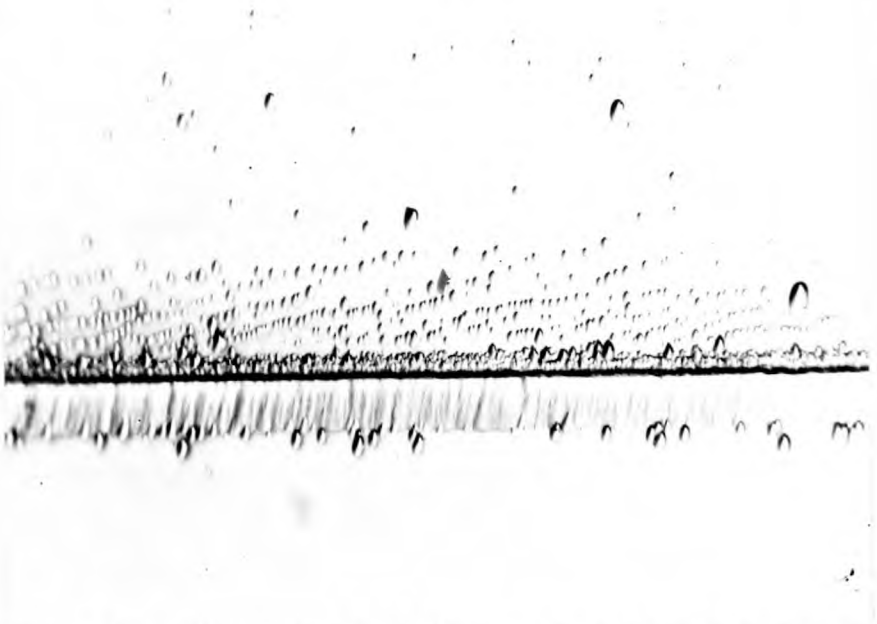


Figure 6.14. Movement of dislocations on the face of the specimen for pure screw dislocation observation at a low stress at 77°K. x 500

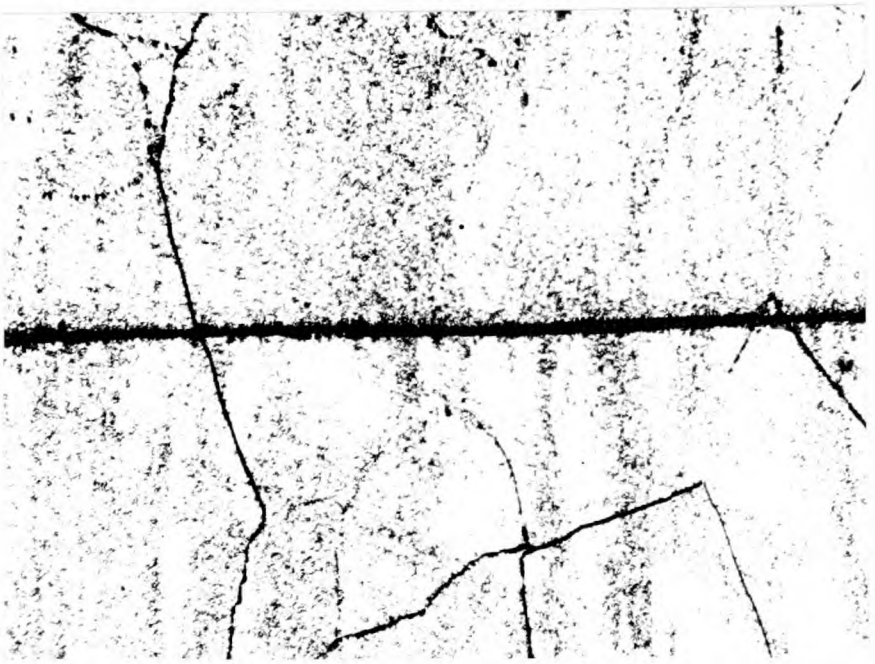


Figure 6.15. Movement and multiplication of dislocations on the same specimen as Figure 6.14., but at a higher stress. x 80.

6.6.1. Stress Dependence of Dislocation Velocity

During the present investigation, velocity of dislocations has been measured over four orders of magnitude in velocity between 10^{-6} cm./sec. and 10^{-2} cm./sec. It is found to be a very sensitive function of applied stress. The stress dependence of dislocation velocity at four different temperatures is presented in Figure 6.16. It is noted that in agreement with the results in other materials the logarithm of the velocity, v, varies linearly with the logarithm of the applied stress, τ. The empirical relationship of Johnston and Gilman[49]

$$v = \left(\frac{\tau}{\tau_o}\right)^m$$

where τ_o is the shear stress for v = 1 cm./sec. is satisfied at all temperatures. The constants m and τ_o at various temperatures are given below.

Temperature	m	τ_o kg/mm.^{2}
77^{o}K	12.2	11.8
153^{o}K	10.9	6.7
243^{o}K	9.6	4.3
298^{o}K	7.2	3.6

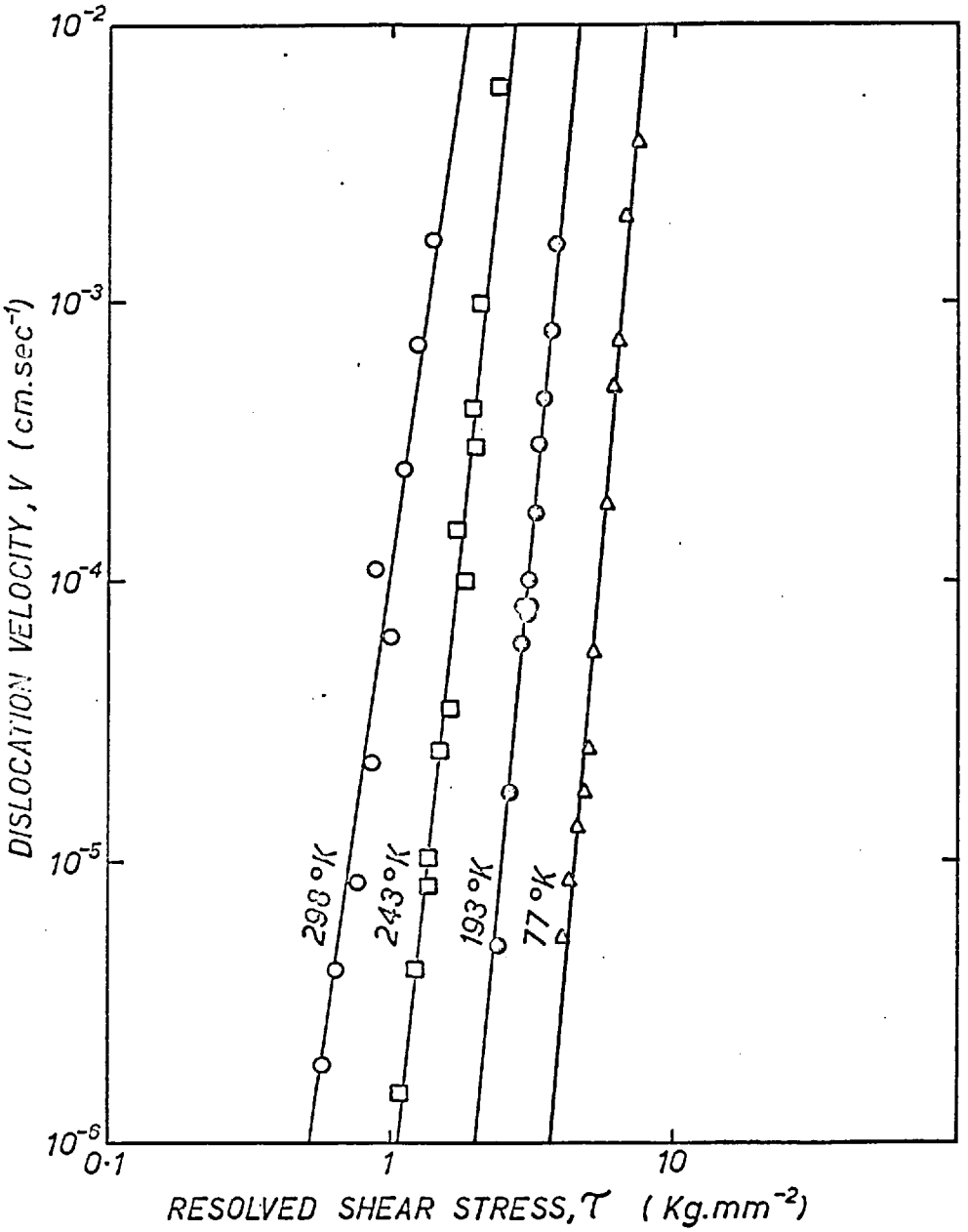


Figure 6.16. Stress dependence of the average velocity of dislocation moving on {110} type slip planes in molybdenum at four different temperatures.

It is noted that m decreases systematically with increasing temperature. The scatter in the data is larger at higher temperatures due to experimental difficulties discussed in Section 6.5.

In order to test whether the parameters m and τ_o vary in different crystals, dislocation velocities have been measured at 77°K in specimens from two different crystals. The plots of log v versus log τ are given in Figure 6.17. It is noted that there is some difference between the two crystals. m values are 12.2 and 11.6 and the corresponding values of τ_o are 11.8 kg/mm.^{2} and 12.4 kg/mm.^{2} respectively.

Dislocation velocities have also been plotted against $\frac{1}{\tau}$ to find out whether Gilman's functional relationship[61]

$$v = v_o e^{-D/\tau}$$

where v_o is the elastic shear wave velocity in the material and D is a characteristic drag stress is satisfied in molybdenum single crystals. Figure 6.18. shows that log v varies linearly with $\frac{1}{\tau}$, although the scatter in the experimental data is considerable at higher temperatures. However, the curves do not extrapolate to the elastic shear wave velocity at infinite stress.

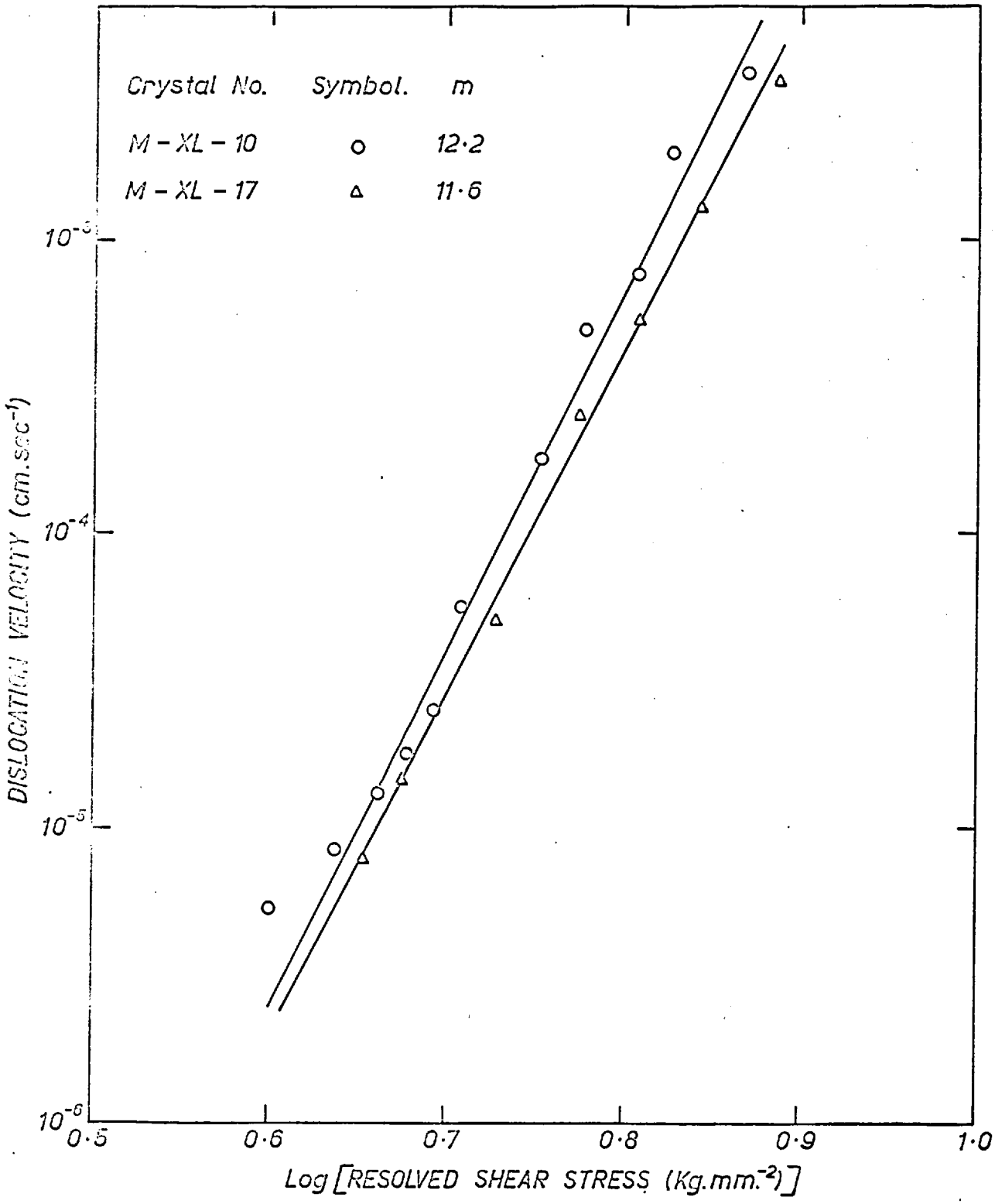


Figure 6.17. Stress dependence of dislocation velocity for two different molybdenum single crystals at 77°K.

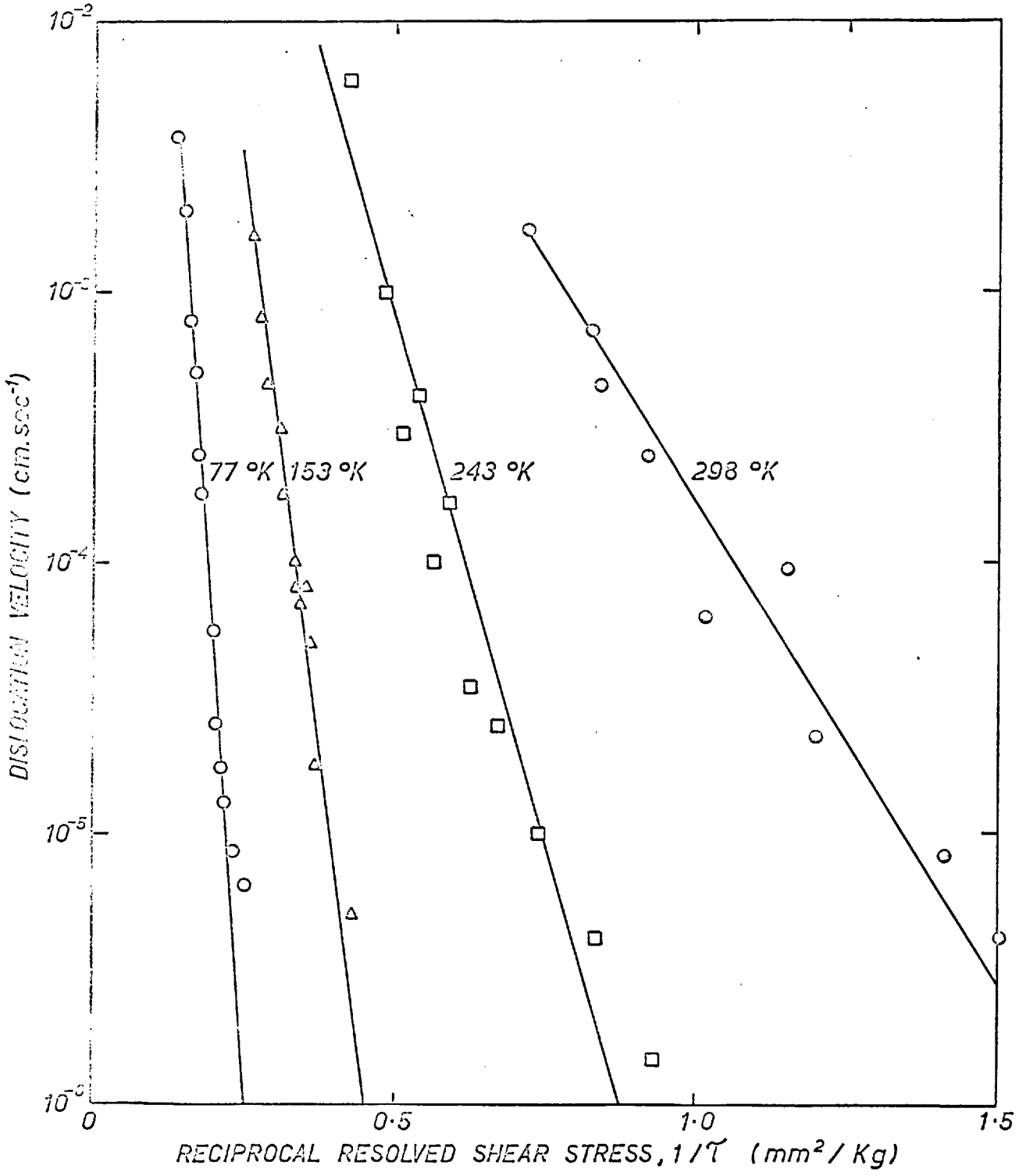


Figure 6.18. Variation of dislocation velocity with reciprocal of applied shear stress.

6.7. Determination of Activation Volume

Activation volume v* for dislocation motion can be determined from the dislocation mobility data using the equation:

$$v^* = kT \left(\frac{\delta \ln v}{\delta \tau} \right)_T \qquad (6.2.)$$

The logarithm of dislocation velocity has been plotted against shear stress at different temperatures in Figure 6.19. and 6.20. Activation volume at different stresses has been calculated from the slopes of these curves and has been plotted as a function of stress at various temperatures in Figure 6.21. It is noted that activation volume for dislocation motion decreases with an increase in stress.

6.8. Temperature Dependence of Dislocation Velocity

In order to determine the temperature dependence of dislocation velocity the stress for a constant velocity from Figure 6.16. was cross plotted against temperature to get a set of constant velocity stress-temperature curves. From this plot velocity at a constant stress has been plotted as a function of reciprocal temperature (Figure 6.22.). The results are very similar to those obtained by Stein and Low[50] for silicon iron. At low stresses an Arrhenius type relationship is satisfied and linear plots are obtained, but as the stress increases, the

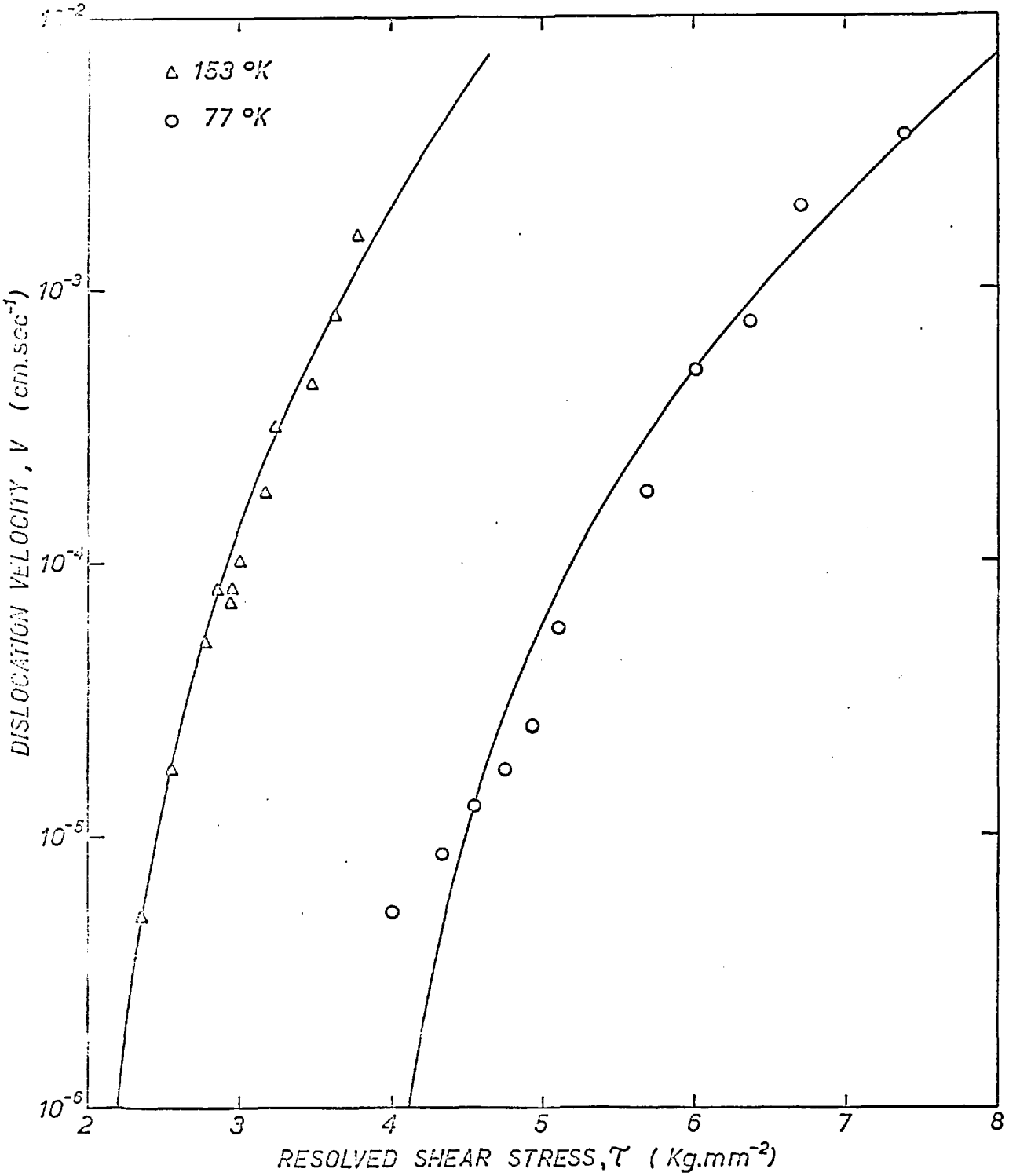


Figure 6.19. Log. dislocation velocity versus resolved shear stress plot at 77°K and 153°K.

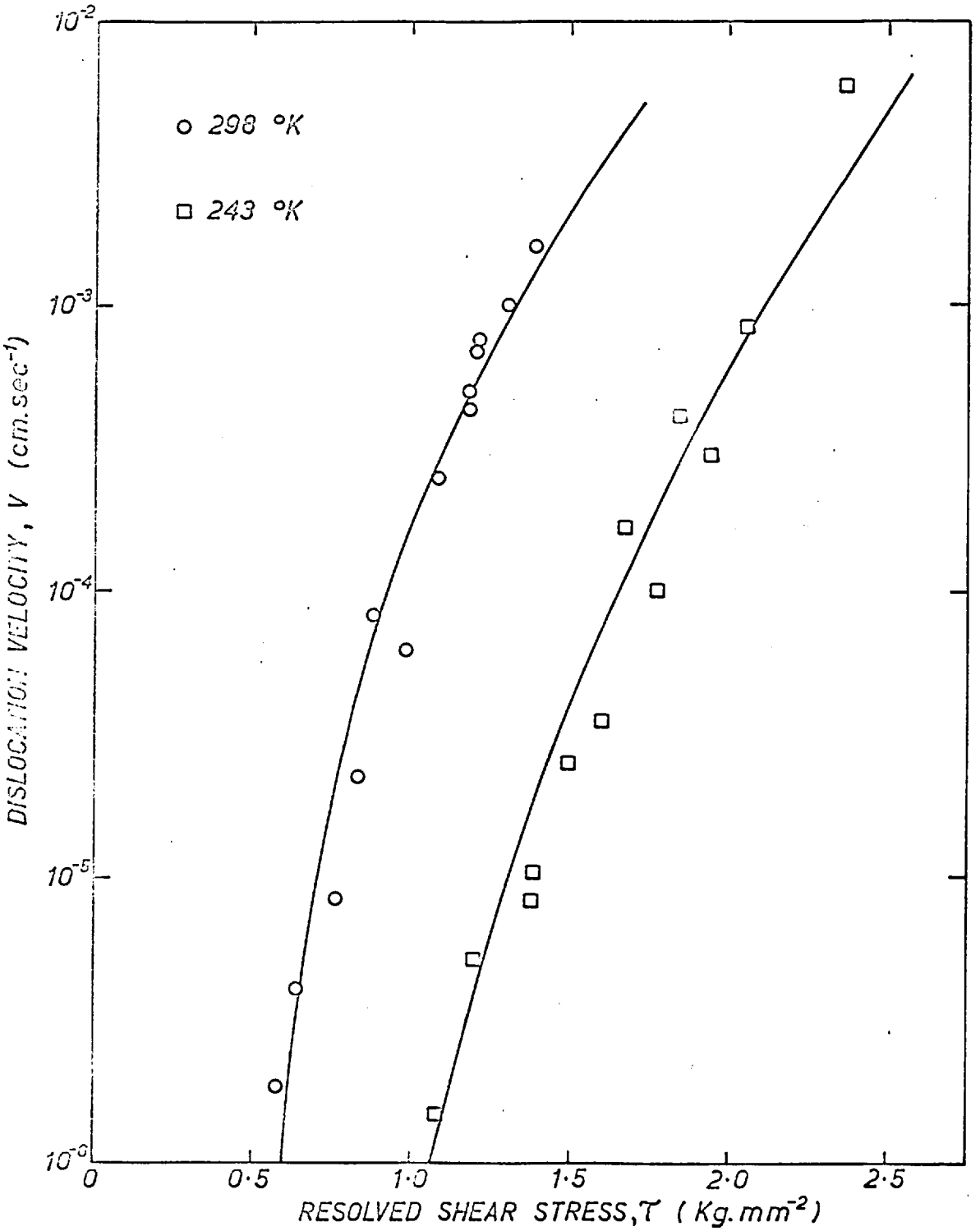


Figure 6.20. Log. dislocation velocity versus resolved shear stress plot at 243°K and 298°K.

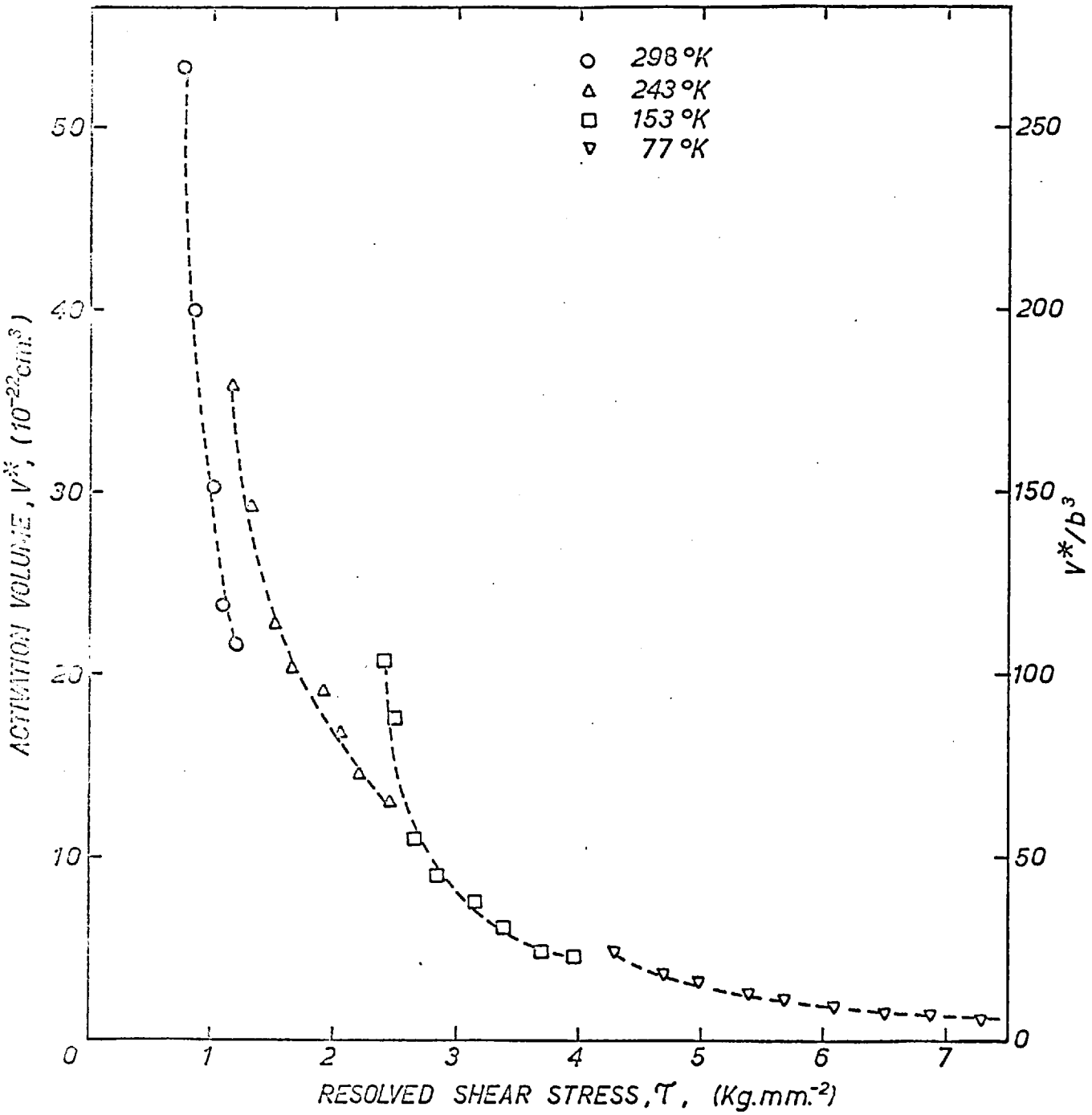


Figure 6.21. Variation of activation volume for dislocation motion with resolved shear stress.

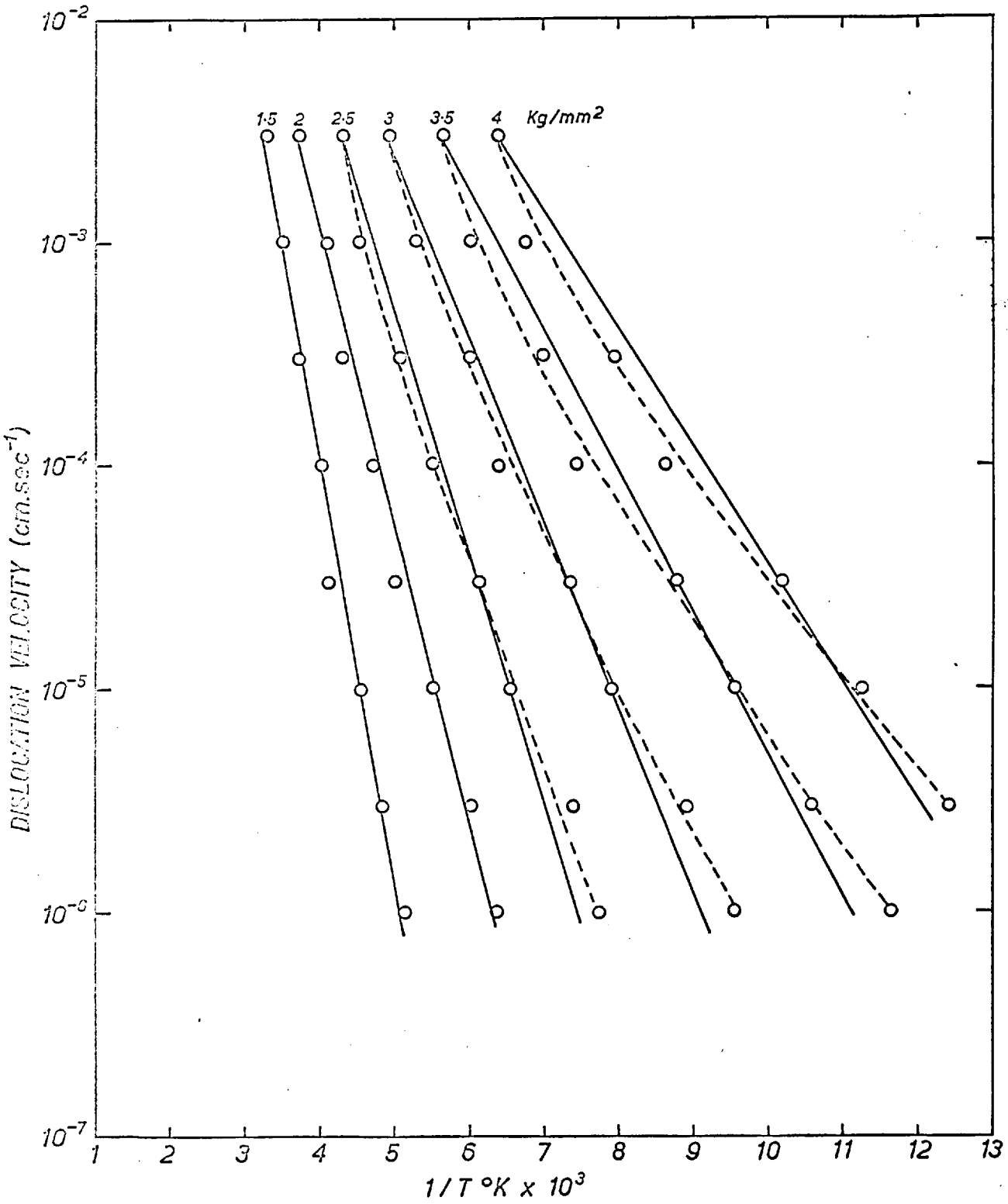


Figure 6.22. Log. velocity - $\frac{1}{T}$ plot for dislocation velocities at various constant stresses.

deviation from linearity also increases. However, the curvature at higher stress may as well have been the effect of temperature rather than stress.

6.8.1. Calculation of Activation Energy for Dislocation Motion

The non-linearity of $v - \frac{1}{T}$ plots of Figure 6.22. indicates that more than one thermally activated mechanism may be rate controlling during dislocation motion. But one can still calculate activation energy, H, from this figure by using the conventional relationship

$$H = -k \left(\frac{\delta \ln v}{\delta \frac{1}{T}} \right)_{\tau} \qquad (6.3.)$$

The H values so obtained are plotted against stress in Figure 6.23. The extent of scatter at various stresses due to the curvature in v versus $\frac{1}{T}$ plot is also shown in this figure.

6.9. Calculation of the Stress Dependence of Dislocation Velocity by Indirect Methods

The power dependence of dislocation velocity on stress, m, has been calculated by both strain rate change and stress relaxation methods. The experimental details for these methods have been discussed in Chapter 5, and only the experimental results will be presented here.

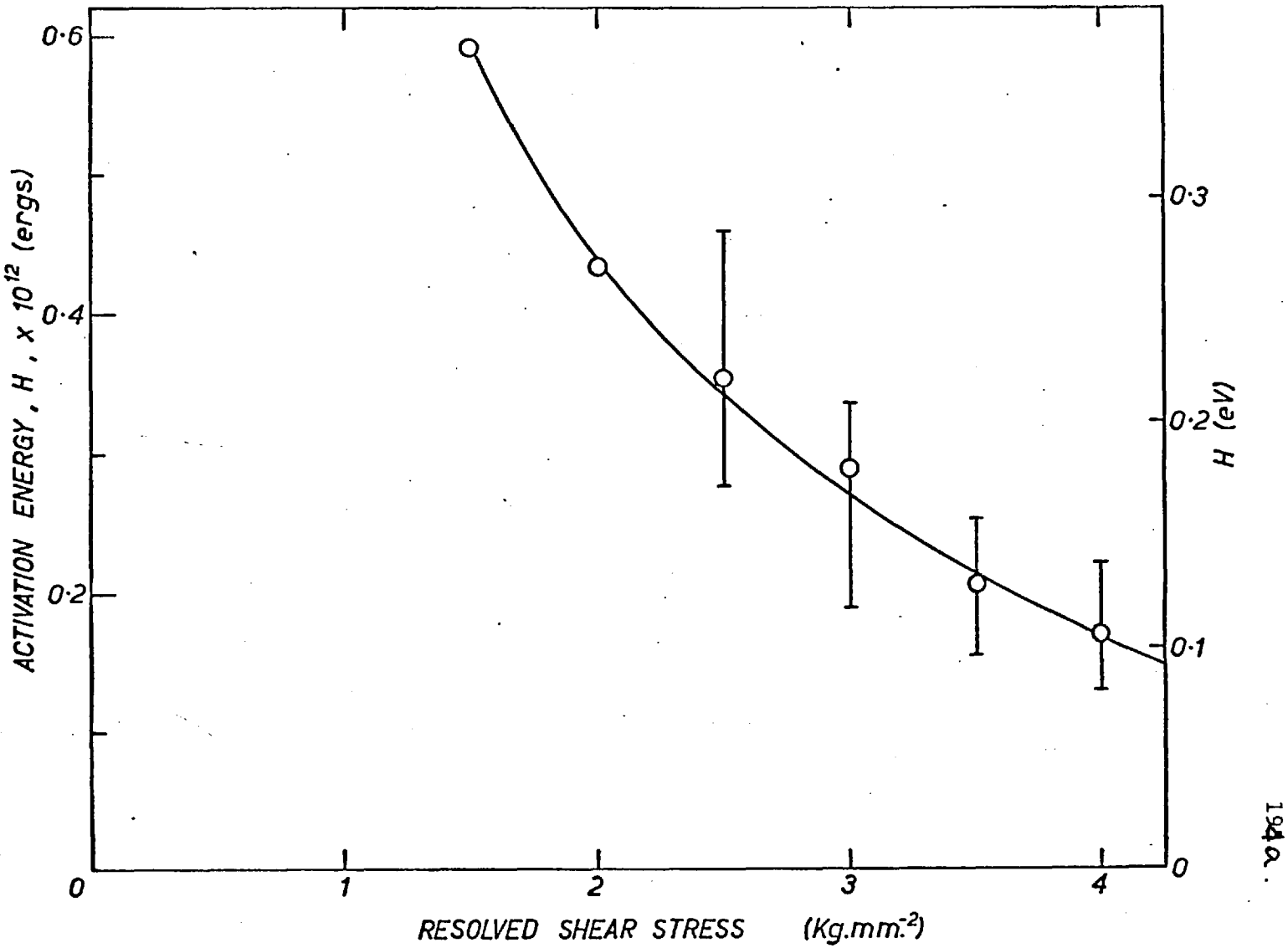


Figure 6.23. Activation energy as a function of resolved shear stress.

6.9.1. Strain Rate Change Experiments

m' has been calculated at different temperatures using the relation

$$m' = \left(\frac{\Delta \log \dot{\varepsilon}}{\Delta \log \tau}\right)_T \qquad (6.4.)$$

The calculated values of m' are plotted against tensile strain at various temperatures in Figure 6.24. In evaluating m', only the upward changes in the stress have been used.

In common with other materials, m' is found to decrease with increasing temperature. At 77°K, 153°K, 373°K and 433°K, m' increases almost linearly with increasing strain. At 193°K and 243°K, m-ε plot is parabolic. At 273°K and 298°K m' increases initially, reaches a maximum and then decreases to a constant value. Following Johnston and Stein's[72] method, m' has been extrapolated to zero strain, but the extrapolated values are still larger than m, calculated by the etch pit method.

6.9.2. Stress Relaxation Experiments

m' has also been determined from stress relaxation experiments, using Noble and Hull's[77, 78] method. The slope of the plot, log τ versus log t, where t is the relaxation time is $\frac{1}{1-m'}$. Values of m' at various temperatures calculated by this method are plotted in Figure 6.25. The values of m' have also

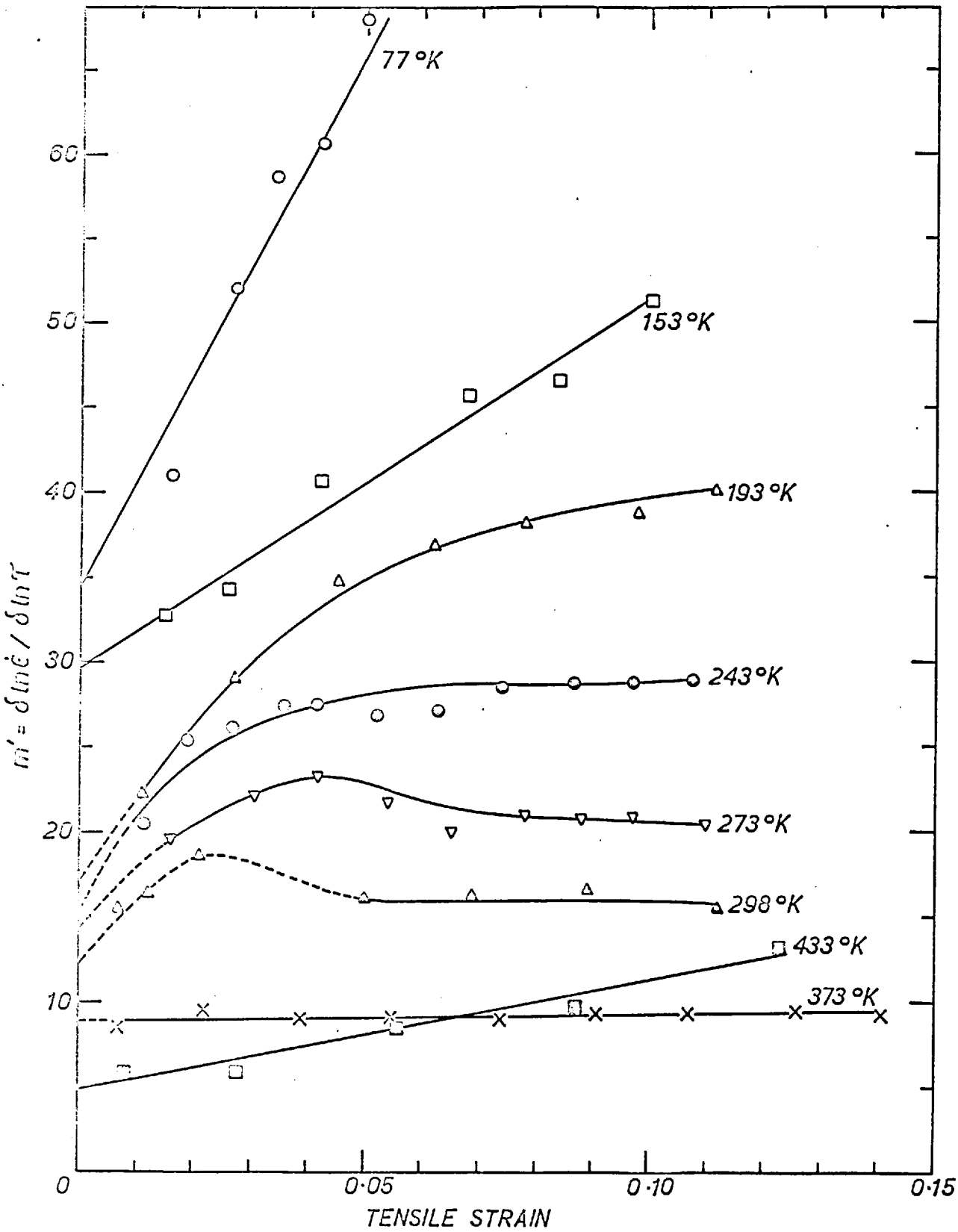


Figure 6.24. Variation of m' with tensile strain (from strain rate change experiments).

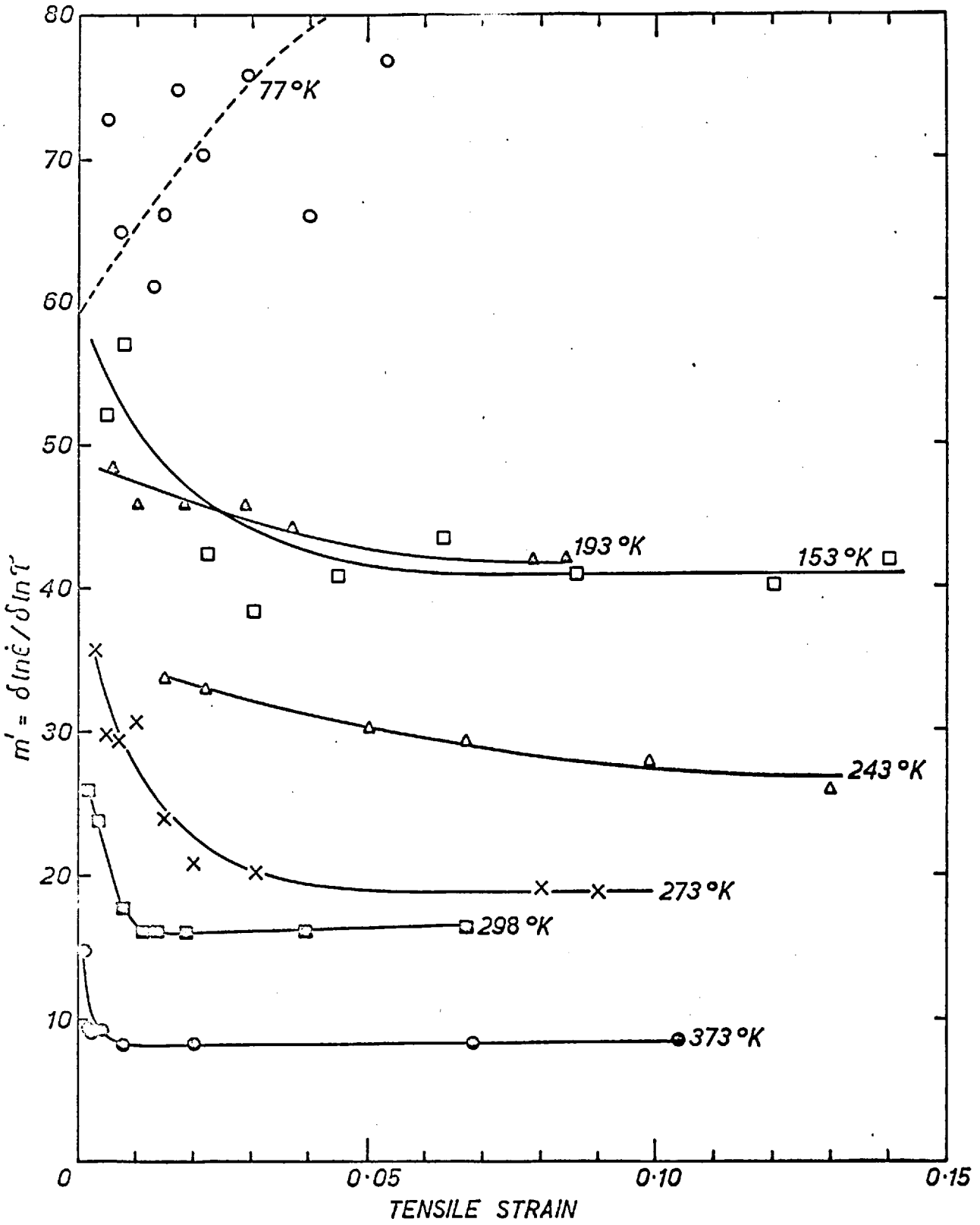


Figure 6.25. Variation of m' with tensile strain (from relaxation experiments using Noble and Hull's method).

been calculated from the strain rate sensitivity λ determined from stress relaxation experiments in Section 5.10. The relation

$$m' = \frac{2.3\tau}{\lambda} \qquad (6.5.)$$

has been used and m' has been plotted against tensile strain for various temperatures in Figure 6.26.

It is noted that both the methods give very similar results. At $77^{o}K$ there is too much scatter in the experimental data and m' seems to increase with strain. Between $153^{o}K$ and $298^{o}K$, m' decreases rapidly with strain in the beginning of deformation, but in later stages it remains constant. At $373^{o}K$ and $433^{o}K$ m' decreases initially and then increases steadily with increasing strain.

In view of the nature of the $m'-\varepsilon$ plots, Johnston and Stein's[72] extrapolation method cannot be applied to the present results.

6.10. Discussion

6.10.1. Stress Dependence of Dislocation Velocity

The relation $v = \left(\frac{\tau}{\tau_o}\right)^m$ is obeyed in the ranges of temperature and velocity used. The decrease of m from 12.2 to 7.2 is very similar to the results obtained in silicon-iron[50, 51] and tungsten[57]. However, Guberman[58] has reported an

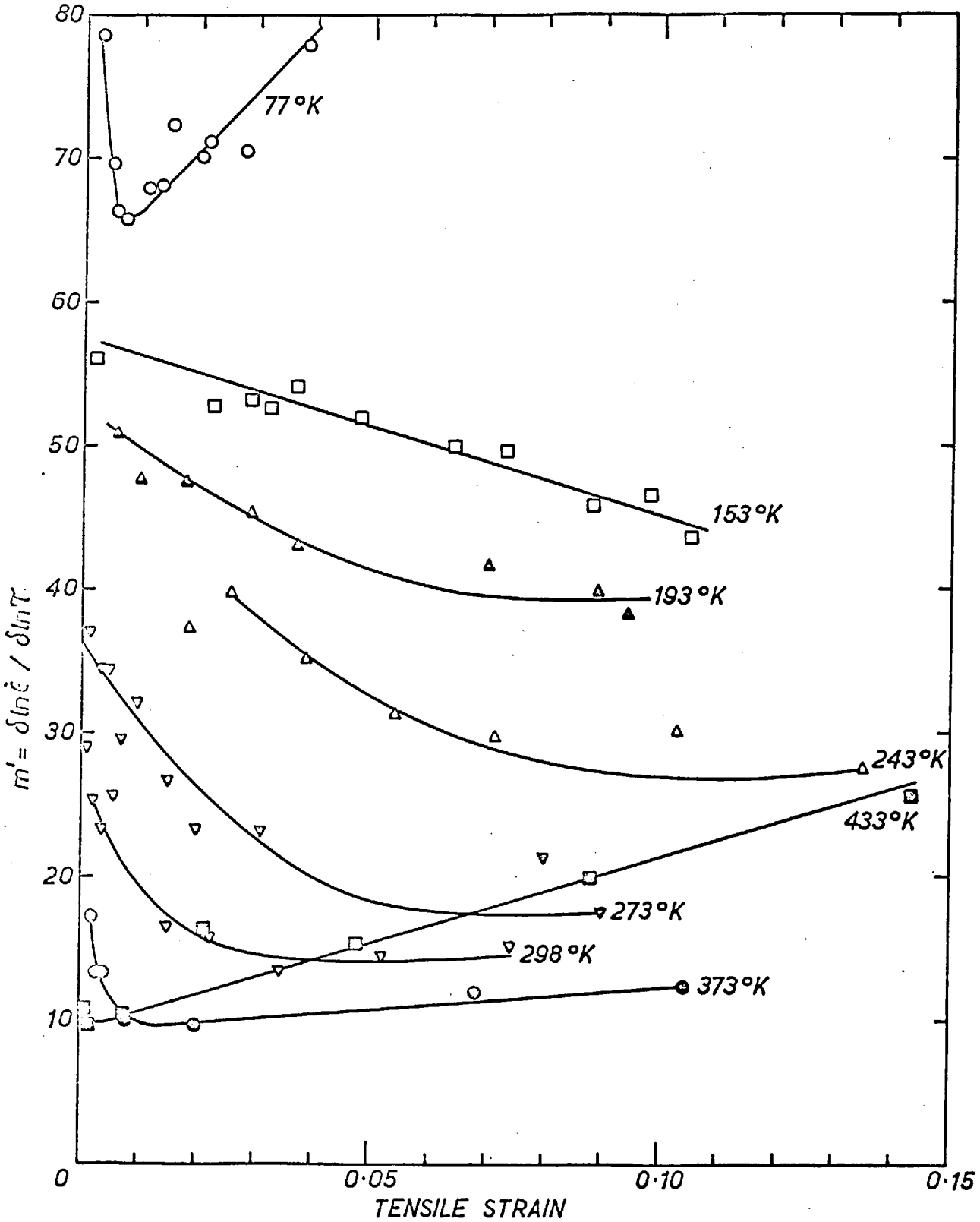


Figure 6.26. Variation m' with tensile strain (from relaxation experiments using strain rate sensitivity λ).

increase in m from 7.5 to 14 in niobium when the temperature is increased from 77°K to 298°K. In tungsten[57] the average value of m is 10.5 at 77°K and 4.8 at 298°K. Both molybdenum and tungsten belong to the same group in the periodic table and have very similar mechanical and physical properties. The agreement in the m values may therefore be noted.

Recently Prekel and Conrad[197] have published the results of dislocation velocity measurements in molybdenum single crystals at room temperature and have obtained m = 6.38 and τ_o = 5.45 kg/mm.^{2}. The present values of m = 7.2 and τ_o = 3.6 kg/mm.^{2} may be compared with their result. The variation in m for different crystals tested at the same temperature is not appreciable and might have been due to either the effect of impurities or experimental error.

The failure of $v - \frac{1}{\tau}$ plot to extrapolate to elastic shear wave velocity at $\frac{1}{\tau} = 0$ may be compared with a similar observation in tungsten single crystals. For molybdenum v_o $(\frac{1}{\tau} \to 0) = 10^2$ cm./sec. whereas the corresponding figure for tungsten[57] is 10^3 cm./aec. However, v_o decreases considerably with increasing temperature. In silicon-iron the extrapolated value is much larger than the theoretical limiting velocity. Gilman[82] has applied a correction term for the back stress in silicon-iron to show the validity of his exponential relationship. However, no such correction can possibly be applied to molybdenum or

tungsten, since the extrapolated velocities are lower than the limiting velocity.

6.10.2. Slip System for Dislocation Motion

It has been found during the present investigation that dislocations move on a {110} plane with a lower resolved shear stress. However, slip line observations at higher strains, indicate that even though multiple slip is occurring in the specimens oriented for single slip, the active slip planes are those with the higher resolved shear stresses. This difference in the operating slip systems for deformation at larger strains and for dislocation motion at stresses below the macroscopic yield stress is interesting. Probably due to some reason the highly stressed planes are passive in the microdeformation range, but operate when the dislocation motion in the lowly stressed planes is exhausted with increasing strain. However, this is purely a speculation. Prekel and Conrad[197] have observed dislocation motion on a {112} plane with a lower resolved shear stress, in molybdenum single crystal specimens of similar orientation.

Another observation has been made during the study of the alignment of etch pits. The deformation in the early stages takes place by the lateral growth of glide bands rather than by the formation of new glide bands. Similar observations have been

made in lithium fluoride[49] and silicon-iron[109].

6.10.3. Comparison of Proportional Limit, Flow Stress and the Stress to Move Fresh Dislocations

The stress for a constant dislocation velocity of 3×10^{-3} cm./sec. has been plotted in Figure 5.33. along with the variation of the proportional limit with temperature and also in Figure 5.34, where the flow stress for 2% tensile strain has been plotted against temperature. It is noted that the curve for the dislocation mobility data is not parallel to those for proportional limit or flow stress. This difference in the temperature dependence of these stresses is in contrast to the observation of Stein and Low[50] in silicon iron. One may try to explain this in terms of a difference in operating slip systems in the two cases or an increase in the internal stress with temperature. However, it is difficult to conceive why the dislocation mobility data which is for edge dislocations and flow stress data which is associated with the movement of screw dislocations should have the same temperature dependence.

6.10.4. Activation Parameters and Rate Controlling Mechanism for Dislocation Motion

The deviation from linearity of the log v versus $\frac{1}{T}$ plot at constant stress indicates that there may be more than one rate

controlling mechanism for dislocation motion. Guiu[133] has also assumed two thermally activated rate controlling mechanisms to explain his results in molybdenum single crystals.

The values of activation volume determined from the dislocation mobility data compare well with those obtained from the strain rate sensitivity for macroscopic flow. The difference in activation volume at the same stress for different temperatures casts some doubt as to the validity of the P.N. force as the rate controlling mechanism. Activation energy is found to decrease with increasing stress and is rather small. But as there is evidence for more than one rate controlling mechanism operating, much importance cannot be attached to this.

6.10.5. Determination of m from Indirect Methods

The values of m' calculated by either strain rate change or relaxation experiments are always much higher than those from the direct etch pit method. Even m' from strain rate change experiments extrapolated to zero strain has a value still larger than m. However, this extrapolation method is doubtful in this case. Due to the high initial work hardening in molybdenum it is difficult to measure m' at less than 1% strain. This has already been pointed out by Schadler[57] for tungsten and he has used the strain rate sensitivity of the proportional limit to calculate m'. In the present case, the strain rate sensitivity

of proportional limit gives m' values comparable to $\frac{d\ln v}{d\ln \tau}$ within experimental error. This comparison is given in Table 6.1.

Table 6.1.

m and m' calculated by direct and indirect methods.

Temperature ^{o}K	m direct	m' C.T.-P.L.	m' C.T.-P.L.(G)	m' [110]P.L.(G)
77	12.2	11.4	11.1	38.5
153	10.9	10.9		
243	9.6	7.2		16.1
298	7.2	6.5	6.2	13.5

C.T. = Centre of unit triangle orientation.

P.L. = Proportional limit.

G = Experimental data of Guiu[157].

Values of m', calculated from the proportional limit data of Guiu[157] for specimens of higher dislocation density compare well with the present results. One may infer from this that probably dislocation density has no effect on the power dependence of dislocation velocity on stress. m' calculated from the proportional limit of specimens with [110] orientation is much higher. Schadler[57] has tried to explain a similar observation

in tungsten in terms of the higher proportional limit and flow stress for [110] orientation. However, this does not seem very convincing and the agreement between m determined by the direct method and the strain rate sensitivity of the proportional limit may be purely a coincidence.

Li and Michalak[76] have attributed the larger values of m from indirect methods to the internal stresses acting on the dislocations. Michalak[73] has calculated the effective stress and the internal stress in high purity iron by using the extrapolated value of m' to zero strain as m. In the present investigation, the effective stress has been calculated with the m values from the etch pit method and the data of strain rate change experiments. It is found that at $77^{\circ}K$ and $153^{\circ}K$, the effective stress remains constant with strain at ≈ 7.5 kg/mm.^{2}; at $243^{\circ}K$ and $298^{\circ}K$ m increases with strain and reaches a value of ≈ 7.2 kg/mm.^{2} at higher strains. One may try to explain this variation of the effective stress with strain in terms of the dislocation configuration at different temperatures. However, the effective stress calculated by this method is independent of temperature at higher strains. This is contrary to the very conception of the effective stress. So the validity of this method seems doubtful.

CHAPTER 7

CONCLUSIONS AND SUGGESTIONS FOR FUTURE WORK

7.1. Conclusions

1. With the available etchants for molybdenum, planes only up to 30° from {100} can be etched and the density of etch pits increases on planes with increasing angle from {100}. The newly developed etchant has much better etching characteristics. It does not show the rapid increase in etch pit density and can etch planes up to $\approx 35^{\circ}$ from {100}. It can also distinguish between the grown-in and fresh dislocations. The reliability of the etchant has been verified.

2. Spark planing introduces much less surface deformation than the mechanical grinding and the depth of the cold worked layer is less than 0.1 mm.

3. It is possible to decrease the density of the grown-in dislocations from $5 \times 10^{5}/cm.^{2}$ to $4 \times 10^{4}/cm.^{2}$ by annealing in high vacuum at $2200^{\circ}C$. Most of the reduction in dislocation density occurs during the first few hours of annealing.

4. The initial dislocation density has a significant effect on the yielding and flow of molybdenum single crystals. The proportional limit and flow stress are lower for specimens with a low dislocation density.

5. In molybdenum single crystals, oriented near the centre

of unit stereographic triangle multiple slip occurs from the early stages of macroscopic deformation. Slip occurs predominently in {110} planes, though at higher temperatures {112} planes may operate mostly as cross slip planes. Usually the active slip planes are the highly stressed ones. However, etch pit alignment in specimens stressed just above the proportional limit indicates that dislocation motion occurs on a {110} plane with a Schmid factor of approximately 0.3. In the early stages, deformation proceeds by the lateral growth of the existing glide bands rather than by the creation of new glide bands.

6. The multiplication of dislocations is a very sensitive function of the initial dislocation density, ρ_o. Strain dependence of dislocation density $\frac{d\rho}{d\varepsilon}$ is found to obey the relation $d\rho/d\varepsilon = \alpha\sqrt{\rho_o}$. Flow stress varies linearly with $\sqrt{\rho}$ and the composite friction stress is small due to the low grown-in dislocation density.

7. Strain rate sensitivity and temperature sensitivity are relatively insensitive to strain at lower temperatures ($<243^{o}K$) and increase with strain at higher temperatures. This may be due to the effect of temperature on the dislocation configuration in the deformed specimens. At higher temperature, the effective number of mobile dislocations may be decreasing with strain due to dislocation tangling.

8. Dislocation velocity, v, satisfies the empirical relation $v = \left(\frac{\tau}{\tau_o}\right)^m$. The power dependence of dislocation velocity on stress, m, is 12.2 at 77°K and decreases to 7.6 at 298°K. Though log v varies linearly with $\frac{1}{\tau}$, it does not extrapolate to the transverse shear wave velocity at infinite stress as Gilman's exponential velocity-stress relation would suggest.

9. The motion of dislocations is very uniform at 77°K, but at higher temperatures it becomes irregular due to cross slip. Also the pinning of the fresh dislocations at low stresses and the unpinning of the grown-in dislocations at high stresses are two problems encountered at higher temperature.

10. The values of the power dependence of dislocation velocity on stress obtained from strain rate change and relaxation experiments are higher than those from the direct etch pit method. However, when the strain rate sensitivity of the proportional limit is used, comparable values are obtained.

11. There is reasonable agreement between the activation parameters determined from flow stress data and dislocation mobility data. Activation energy as a function of stress is independent of strain and temperature which favours the P.N.F. as the rate controlling mechanism. But the non-linearity of the $\log v - \frac{1}{T}$ plot indicates that there may be more than one rate controlling mechanism for dislocation motion.

7.2. Suggestions for Future Work

Some of the observations made in the course of the present work need further investigation. It will be interesting to study the mobility of pure screw dislocations in molybdenum. Recently a lot of controversy has arisen regarding the role of impurities and P.N.F. as the rate controlling mechanisms during the yielding and flow of b.c.c. metals. So the effect of impurities on the dislocation mobility may be worth investigating.

The alignment of etch pits in slightly deformed molybdenum single crystal specimens indicates that a {110} plane with a low resolved shear stress is operating in the early stages of deformation. Also the active slip system is the same on both the compression and tension sides of a bending specimen. Similar experiments with crystals of other orientations are necessary to find out whether it is an orientation effect or occurs for all orientations.

The dislocation etch pitting method as well as the dislocation mobility data may be used to study crack propagation in molybdenum. Finally, one may investigate the effect of the low dislocation density on the yielding and flow in molybdenum single crystals of different orientations.

REFERENCES

1. J. Frenkel; Zeit Phys. 37 572 (1926).
2. R. Baker; Zeit Phys. 26 919 (1925).
3. G. I. Taylor; Proc. Roy. Soc. A145 362 (1934).
4. M. Polanyi; Zeit Phys. 89 660 (1934).
5. E. Orowan; Zeit Phys. 89 605, 634 (1934).
6. W. L. Bragg and W. M. Lomer; Proc. Roy. Soc. A196 171 (1949).
7. W. K. Burton, N. Cabrera and F. C. Frank; Phil. Trans. Roy. Soc. A243 299 (1951).
8. L. J. Griffin; Phil. Mag. 41 196 (1950).
9. L. J. Griffin; ibid 42 775, 1337 (1951).
10. A. R. Verma; Phil. Mag. 42 1005 (1951).
11. S. Amelinckx; J. Chem. Phys. 49 411 (1952).
12. A. J. Forty; Advan. Phys. (Phil. Mag. Supplement) 3 1 (1954).
13. F. H. Horn; Phil. Mag. 43 1210 (1952).
14. A. A. Hendrickson and E. S. Machin; Acta Met. 3 64 (1955).
15. W. Bontinck; Phil. Mag. 2 516 (1957).
16. S. Amelinckx; Acta Met. 2 848 (1954).
17. F. W. Young and A. T. Gwathmey; J. Appl. Phys. 31 225 (1960).
18. W. R. Hibbard and C. G. Dunn; Acta Met. 4 306 (1956).
19. G. K. Wehner; J. Appl. Phys. 29 217 (1958).
20. R. Backish; Acta Met. 6 120 (1958).
21. A. B. Michael and F. J. Huegel; Acta Met. 5 339 (1957).
22. J. D. Livingstone; J. Appl. Phys. 31 1071 (1960).

23. I. Berlec; J. Appl. Phys. 33 197 (1962).

24. P. J. Holmes; Acta Met. 7 283 (1959).

25. J. M. Hedges and J. W. Mitchel; Phil. Mag. 44 223 357 (1953).

26. W. C. Dash; J. Appl. Phys. 27 1193 (1956).

27. J. Newkirk; Phys. Rev. 110 1465 (1958).

28. J. Newkirk; Trans. Met. Soc. A.I.M.E. 215 483 (1959).

29. A. R. Lang; Acta Cryst. 12 249 (1959).

30. K. A. Carlson and R. Wegener; J. Appl. Phys. 32 125 (1961).

31. U. Bonse and E. Kappler; Z. Naturforsch 13a 348 (1958).

32. G. Borrmann, W. Harting and H. Irmler; ibid 423 (1958).

33. J. W. Menter; Proc. Roy. Soc. A236 119 (1956).

34. H. Hashimato and R. Oyeda; Acta Cryst. 10 143 (1957).

35. P. B. Hirsch, R. W. Horne and M. J. Whelan; Phil. Mag. 1 677 (1956).

36. P. B. Hirsch, A. Howie and M. J. Whelan; Phil. Trans. Roy. Soc. A252 499 (1960).

37. W. Bollmann; Phys. Rev. 103 1588 (1956).

38. H. Tomlinson; Phil. Mag. 3 861 (1958).

39. V. A. Phillips; Phil. Mag. 5 571 (1960).

40. S. Amelinckx and P. Delavignette; "Direct Observation of Imperfections in Crystals" Interscience (N.Y.) p. 295 (1962).

41. M. J. Whelan, P. B. Hirsch, R. H. Horne and W. Bollmann; Proc. Roy. Soc. A240 524 (1957).

42. P. B. Hirsch, J. Silcox, R. E. Smallman and K. H. Westmacott; Phil. Mag. 3 897 (1958).

43. G. Thomas; Transmission Electron Microscopy of Metals, John Wiley New York (1962).

44. S. Amelinckx; The Direct Observation of Dislocations, Solid State Physics, Supplement 6 Academic Press New York (1964).

45. E. W. Müler; Direct Observation of Imperfections in Crystals p. 77 (Inter Science N.Y.) (1962).

46. G. Brandon and W. Wald; Phil. Mag. 6 1035 (1961).

47. H. F. Ryan and J. Suiter; Acta Met. 14 847 (1966).

48. P. R. V. Evans; J. Less-Common Metals 6 253 (1964).

49. W. G. Johnston and J. J. Gilman; J. Appl. Phys. 30 129 (1959).

50. D. F. Stein and J. R. Low; J. Appl. Phys. 31 862 (1960).

51. J. S. Erickson; J. Appl. Phys. 33 2499 (1962).

52. A. R. Chaudhury, J. R. Patel and L. J. Rubin; J. Appl. Phys. 33 2736 (1962).

53. D. Dew-Hughes; I.B.M. Journ. 5 279 (1961).

54. M. N. Kabler; Phys. Rev. 131 54 (1963).

55. E. Yu. Gutmanas, E. M. Nadgornyi and A. V. Stepanov; Soviet Phys. Solid State 5 743 (1963).

56. E. M. Nadgornyi and E. Yu. Gutmanas; Physical Basis of Yield and Fracture, Inst. Phys. and Phys. Soc. Oxford Conf. Proc. p. 266 (1966).

57. H. W. Schadler; Acta Met. 12 861 (1964).

58. H. D. Guberman; Radiation Metallurgy Section, Solid State Division Prog. Rep. ORNL-4020 p. 41, July 1966.

59. G. S. Ansele, M. J. Roblin and R. S. Goodrich; J. Metal. 13 662 (1961).

60. T. Suzuki and H. Kojima; Acta Met. 14 913 (1966).

61. J. J. Gilman; Australian J. Phys. 13 327 (1960).

62. J. J. Gilman; J. Appl. Phys. 36 3195 (1965).

63. V. Celli, M. Kabler, T. Ninomiya and R. Thompson; Phys. Rev. 131 58 (1963).

64. A. Lawley and H. L. Gaigher; Phil. Mag. 10 15 (1964).

65. J. R. Low and A. M. Tukaylo; Acta Met. 10 215 (1962).

66. W. G. Johnston and J. J. Gilman; J. Appl. Phys. 31 632 (1960).

67. J. S. Koehler; Phys. Rev. 86 52 (1952).

68. E. Orowan; Dislocations in Metals A.I.M.M.E. (N.Y.) p. 103 (1954).

69. G. T. Hahn; Acta Met. 10 727 (1962).

70. R. W. Guard; Acta Met. 9 163 (1961).

71. A. H. Cottrell; Dislocations and Plastic Flow in Crystals Oxford University Press (1953).

72. W. G. Johnston and D. F. Stein; Acta Met. 11 317 (1963).

73. J. T. Michalak; Acta Met. 13 213 (1965).

74. J. W. Christian; Acta Met. 12 99 (1964).

75. S. Floreen and T. E. Scott ibid 12 750 (1964).

76. J. C. M. Li and J. T. Michalak ibid 12 1458 (1964).

77. D. Hull and F. W. Noble; Dislocations in Solids (Faraday Soc. Lond.) p. 251 (1964).

78. F. W. Noble and D. Hull; Acta Met. 12 1089 (1964).

79. F. Guiu and P. L. Pratt; Phys. Stat. Sol. 6 111 (1964).

80. J. C. M. Li; Canadian Jour. Phys. 45 493 (1967).

81. A. H. Cottrell; Bristol Conf. Rep. on the Strength of Solids (Phys. Soc. Lond.) p. 30 (1948).

82. A. H. Cottrell and B. A. Bilby; Proc. Phys. Soc. A62 49 (1949).

83. J. R. Low Jnr. and M. Gensamer; Trans. A.I.M.M.E. 158 207 (1944).

84. H. Conrad and G. Schoeck; Acta Met. 8 791 (1960).

85. R. P. Carreker and R. W. Guard; Trans. A.I.M.M.E. 206 178 (1956).

86. M. M. Hutchison; Phil. Mag. 8 121 (1963).

87. J. J. Gilman and W. G. Johnston; Dislocations and Mechanical Properties of Crystals (John Wiley N.Y.) p. 116 (1957).

88. W. G. Johnston; J. Appl. Phys. 33 2716 (1962).

89. A. H. Cottrell; The Relation Between the Structure and Mechanical Properties of Metals (H.M.S.O. Lond.) p. 456 (1963).

90. R. E. Peierls; Proc. Phys. Soc. 52 34 (1940).

91. F. R. N. Nabarro; ibid 59 256 (1947).

92. A. Seeger; Phil. Mag. 1 651 (1956).

93. A. Seeger, H. Donth and F. Pfaff; Disc. Faraday Soc. 23 10 (1957).

94. J. Lothe and J. P. Hirth; Phys. Rev. 115 543 (1959).

95. J. E. Dorn and S. Rajnak; Trans. Met. Soc. A.I.M.E. 230 1052 (1964).

96. G. Saada; Acta Met. 8 200 (1960).

97. G. Saada; Acta Met. 9 166 (1961).

98. G. Saada; Electron Microscopy and Strength of Crystals (Inter Science N.Y.) p. 651 (1963).

99. R. Bensen, G. Thomas and J. Washburn; Direct Observation of Imperfections in Crystals (Inter Science N.Y.) p. 375 (1962).

100. A. S. Keh and Weissmann; Electron Microscopy and Strength of Crystals (Inter Science N.Y.) p. 231 (1963).

101. W. Carrington, K. F. Hale and D. McLean; Proc. Roy. Soc. A257 203 (1960).

102. G. Schoeck; Acta Met. 9 382 (1961).

103. J. Friedel; Dislocations (Pergamon) 1964.

104. A. Seeger; Phil. Mag. 46 1194 (1955).

105. P. B. Hirsch; 5th International Congress in Crystallography Cambridge (1960).

106. T. E. Mitchell, R. A. Foxal and P. B. Hirsch; Phil. Mag. 8 1895 (1963).

107. R. A. Foxall, M. S. Duesbery and P. B. Hirsch; Canadian Jour. Phys. 45 607 (1967).

108. A. W. Sleeswyk; Phil. Mag. 8 1467 (1963).

109. J. R. Low and R. W. Guard; Acta Met. 7 171 (1959).

110. R. L. Fleischer; Acta Met. 10 835 (1962).

111. G. Schoeck; Phys. Rev. 102 1458 (1956).

112. G. Schoeck and A. Seeger; Acta Met. 7 469 (1959).

113. R. J. Arsenault; Phil. Mag. 13 31 (1966).

114. B. L. Mordike and P. Haasen; Phil. Mag. 7 459 (1962).

115. J. C. Fisher; Trans. A.S.M. 47 451 (1955).

116. J. Heslop and N. J. Petch; Phil. Mag. 1 866 (1956).

117. H. Conrad; J. Iron and Steel Inst. 198 364 (1961).

118. H. Conrad and W. Hays; Trans. A.S.M. 56 249 (1963).

119. H. Conrad; The Relation Between the Structure and Mechanical Properties of Metals (H.M.S.O. Lond.) p. 476 (1963).

120. Z. S. Basinski and J. W. Christian; Aust. J. Phys. 13 299 (1960).

121. J. W. Christian and B. C. Masters; Proc. Roy. Soc. A281 223 (1964).

122. A. Lawley, J. Van den Sype and R. Madin; J. Inst. Met. 91 23 (1962).

123. R. C. Koo; Acta Met. 11 1083 (1963).

124. D. F. Stein, J. R. Low and A. U. Seybolt; Acta Met. 11 1253 (1963).

125. D. F. Stein; Acta Met. 14 99 (1966).

126. B. L. Mordike; Zeit. f. Metall. 53 586 (1962).

127. R. M. Rose, D. P. Ferris and J. Wulff; Trans. Met. Soc. A.I.M.E. 224 981 (1962).

128. D. P. Gregory; Acta Met. 11 455 (1963).

129. D. P. Gregory, A. N. Stroh and G. H. Rowe; Trans. Met. Soc. A.I.M.E. 227 678 (1963).

130. N. Brown and R. A. Ekrall; Acta Met. 10 1101 (1962).

131. R. Kossowsky and N. Brown; Acta Met. 14 131 (1966).

132. H. Conrad; J. Metals 582 (1964).

133. F. Guiu; Phys. Stat. Sol. 19 339 (1967).

134. N. K. Chen, R. Madin and R. B. Pond; J. Metals 462 June 1951.

135. P. H. Keck and M. J. E. Colay; Phys. Rev. 89 1297 (1953).

136. E. Buchler; Trans. Met. Soc. A.I.M.E. 212 694 (1958).

137. A. Lawley; Electronics 32 39 (1959).

138. I. Drangel and G. Murray; Material Research Corp. Rep. to A.I.M.E. Meeting Feb. 1964.

139. H. W. Schadler and J. R. Low; General Electric Res. Lab. Rep. No. 62-GC-206 (1962).

140. M. Davis, A. Calverly, R. F. Lever; J. Appl. Phys. 27 195 (1956).

141. H. C. Kim and P. L. Pratt; Materials Research Bulletin 2 323 (1967).

142. W. Haywang; Z. Naturforsch 11 232 (1956).

143. P. H. Keck, M. Green and M. L. Polk; J. Appl. Phys. 24 1479 (1953).

144. H. W. Schadler; The Art and Science of Growing Crystals John Wiley (N.Y.) p. 343 (1963).

145. W. G. Pfann; Met. Rev. 2 29 (1958).

146. W. G. Pfann; Zone Melting John Wiley (N.Y.) (1958).

147. W. A. Tiller; The Art and Science of Growing Crystals John Wiley (N.Y.) 276 (1963).

148. J. E. Kunzler and J. H. Wernick; Trans. Met. Soc. A.I.M.E. 212 856 (1958).

149. E. Buehler and J. E. Kunzler; Trans. Met. Soc. A.I.M.E. 221 957 (1961).

150. O. Winkler; Met. Rev. 5 1 (1960).

151. S. D. Hurwitt and M. A. Adams; Metals Progress Feb. 1963.

152. H. R. Smith; Vacuum Metallurgy Reinhold Pub. Co. (N.Y.) p. 221 (1958).

153. R. Emeis; Z. Naturforsch 9A 67 (1954).

154. A. Calverly, M. Davis and R. Lever; J. Sci. Instr. 34 142 (1957).

155. F. E. Birbeck and A. Calverly; J. Sci. Instr. 36 460 (1959).

156. M. Cole, C. Fisher and I. A. Bucklow; Brit. J. Appl. Phys. 12 577 (1961).

157. F. Guiu; Ph.D. Thesis London University (1965).

158. J. D. Livingstone; Acta Met. 10 229 (1962).

159. D. A. Young; Nature 182 375 (1958).

160. J. J. Gilman and W. G. Johnston; J. Appl. Phys. 29 877 (1958).

161. J. J. Gilman; J. Appl. Phys. 31 936 (1960).

162. W. G. Johnston and J. J. Gilman; J. Appl. Phys. 31 632 (1960).

163. W. G. Johnston; Progress in Ceramic Science Pergamon Press p. 1 (1962).

164. J. J. Gilman and W. G. Johnston; J. Appl. Phys. 27 1018 (1956).

165. H. W. Schadler; Direct Observation of Imperfections in Crystals (Inter Science p. 593 (1962).

166. W. C. Dash; Dislocations and Mechanical Properties of Crystals (John Wiley N.Y.) p. 57 (1957).

167. H. Pickering; Acta Met. 13 437 (1965).

168. J. F. Nye; Acta Met. 1 153 (1953).

169. F. L. Vogel; Trans. A.I.M.E. 206 946 (1956).

170. F. L. Vogel, W. G. Pfann, H. E. Corey and E. E. Thomas; Phys. Rev. 90 489 (1953).

171. W. T. Read and W. Shockley; Phys. Rev. 78 275 (1950).

172. S. Amelinckx; Acta Met. 2 848 (1954).

173. W. G. Pfann and C. C. Lovell; Acta Met. 3 512 (1955).

174. C. G. Dunn and W. R. Hibbard; Acta Met. 3 512 (1955).

175. G. W. King and J. W. Spretnak; Trans. Amer. Inst. Mech. Engrs. 216 745 (1964).

176. H. L. Prekel and A. Lawley; Phil. Mag. 14 545 (1966).

177. K. T. Aust and R. Maddin; Acta Met. 4 632 (1956).

178. F. Duan, M. Nay-Ben, L. Chi and L. Tian-nan; Scientia Sinica 12 979 (1963).

179. F. Duan, M. Nay-Ben and L. Chi; Scientia Sinica 12 909 (1963).

180. D. P. Ferris, R. M. Rose and J. W. Wulff; Trans. Met. Soc. A.I.M.E. 224 975 (1962).

181. G. Taylor and J. W. Christian; Phil. Mag. 15 873 (1967).

182. M. Cole, I. A. Bucklow and C. W. B. Grigson; Brit. J. Appl. Phys. 12 296 (1961).

183. M. H. Farmer and G. H. Glaysher; J. Sci. Instr. 30 9 (1953).

184. D. H. Avery, M. L. Ebner and W. A. Blackofen; Trans. Met. Soc. A.I.M.E. 212 256 (1958).

185. D. F. Stein; Canadian J. Phys. 45 1063 (1967).

186. F. Guiu and P. L. Pratt; Phys. Stat. Sol. 15 539 (1966).

187. E. Schmid and W. Bois; Plasticity of Crystals, Hughes and Co. Ltd. London (1950).

188. A. S. Keh; Phil. Mag. 12 9 (1965).

189. T. E. Mitchell and W. A. Spitzig; Acta Met. 13 1169 (1965).

190. A. Gilbert, B. A. Wilcox and G. T. Hahn; Phil. Mag. 12 649 (1965).

191. A. N. Andrade and Y. S. Chow; Proc. Roy. Soc. 175A 962 (1940).

192. H. W. Schadler and J. R. Low; General Electric Res. Lab. Rep. No. 62-GC-206 (1962).

193. B. Sestak and S. Libovicky; The Relation Between the Structure and the Mechanical Properties of Metals (London H.M.S.O.) p. 158 (1963).

194. F. W. Noble and D. Hull; Phil. Mag. 12 777 (1965).

195. C. N. Reid, A. Gilbert and A. R. Rosenfield; Phil. Mag. 12 409 (1965).

196. H. Conrad and S. Frederick; Acta Met. 10 1013 (1962).

197. H. L. Prekel and H. Conrad; Acta Met. 15 955 (1967).

ACKNOWLEDGEMENTS

I am very grateful to Professor P. L. Pratt for his continued interest and guidance throughout this work and to Professor J. G. Ball for providing research facilities.

Thanks are also due to my colleagues in the department, especially Mr. V. Ramaswamy and Mr. D. Kirk for their encouragement and help and to Dr. F. Guiu for many valuable discussions. The assistance of the technical staff in the department is gratefully acknowledged.

Finally I would wish to thank the Council of Scientific and Industrial Research, Government of India and the Central Electricity Generating Board for their generous financial help.